Max-Planck-Institut
für Kolloid- und Grenzflächenforschung

Nanostructured Carbohydrate-Derived Carbonaceous Materials

Dissertation

zur Erlangung des akademischen Grades
"doctor rerum naturalium"
(Dr. rer. nat.)
in der Wissenschaftsdisziplin "Physikalische Chemie"

eingereicht an der
Mathematisch-Naturwissenschaftlichen Fakultät
der Universität Potsdam

von
Shiori KUBO

Potsdam, den 16, 02, 2011

Published online at the
Institutional Repository of the University of Potsdam:
URL http://opus.kobv.de/ubp/volltexte/2011/5315/
URN urn:nbn:de:kobv:517-opus-53157
http://nbn-resolving.de/urn:nbn:de:kobv:517-opus-53157

Nanostructured Carbohydrate-Derived Carbonaceous Materials

Shiori KUBO

Contents

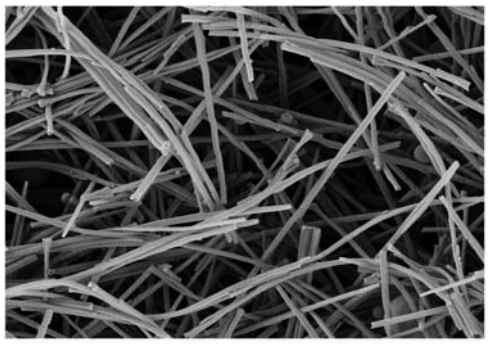

「人間は考える葦である。」

Man is but a reed, the weakest of nature, but he is a thinking reed.

L'homme n'est qu'un roseau, le plus faible de la nature; mais c'est un roseau pensant.

- Blaise Pascal -

1. Introduction

From ancient times, society has made use of porous carbon materials; charcoal was used for decolourisation of alcohol, water and sugar in ancient Egypt.[1] In Asian history, it has also been used as an adsorbent in order to protect religious shrines from moisture attack.[1] Today, porous carbon materials are widely used in industry as adsorbents (e.g. activated carbon) for drinking water, wastewater and gas purification or as catalysts or catalyst supports.[2,3,4,5] The developed surface area and pore properties of such materials play an important role enhancing the adsorption capacity or catalytic activity.

Carbon materials are essential in the applications associated with our daily life and are becoming of increasing interest to the developing application fields of energy storage[6] (e.g. electrodes for Li ion batteries or supercapacitors), fuel cells[7] (e.g. novel catalysts for the oxygen reduction reaction) or chromatography technologies[8,9,10] due to the increasing need of sustainable energy supply and highly developed biological / medical technologies (Figure 1.1). When compared to conventional electrolytic capacitors or to batteries, carbon-based supercapacitors offer good specific energy (1-10 Wh kg^{-1}), as recently demonstrated, for example, by carbon aerogels with high porosity and surface area (> 50 %, 400 - 1000 m^2g^{-1}).[11,12] Due to the extreme versatility of carbon materials available (e.g. crystalline, amorphous, bulk, nanostructured, activated, functionalised), a great deal of literature research has discussed the use of various electrodes configurations

for supercapacitors. This is a good example of how material porosity directly affects the electrochemical performance. In order to improve even further the performance of carbon materials, novel synthetic approaches as well as a developed fundamental understanding of their properties are strongly desirable from materials chemistry point of view.

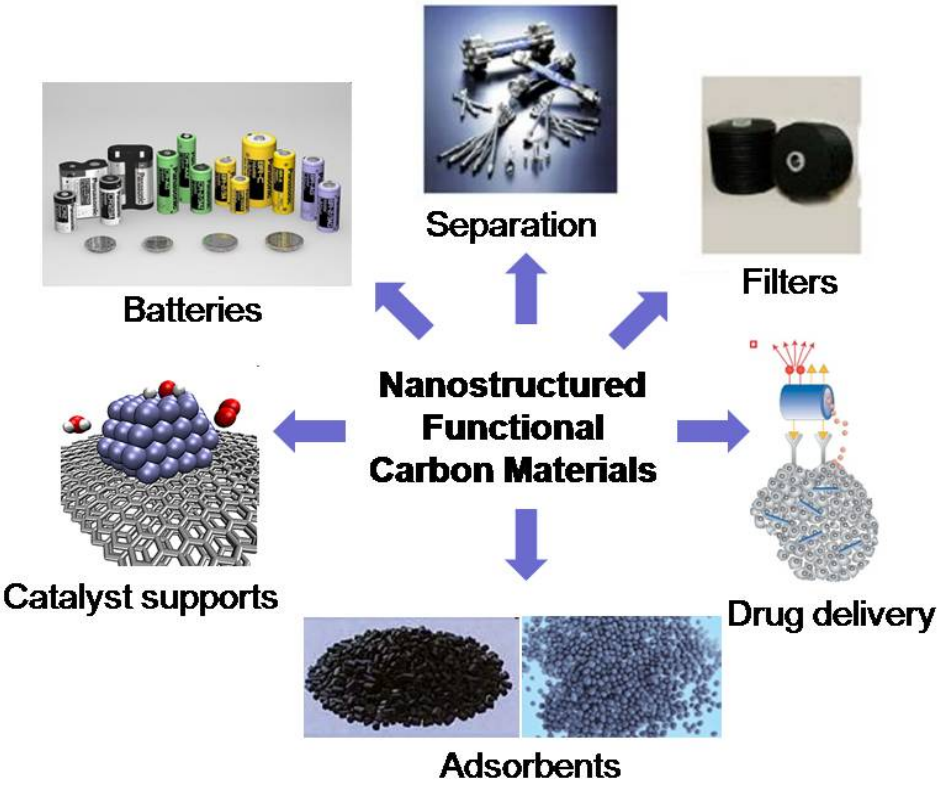

Figure 1.1: Main application fields of porous carbon materials.[13,14,15]

Carbon is one of the most versatile elements, which can be found as different allotropes. The most common crystalline carbon allotropes are diamond and graphite. In diamond the carbon atoms have sp^3 hybridisation and are tetrahedral, while sp^2 hybridisation occurs in graphite resulting in a layered, planer structure of hexagonal lattice. More recently discovered crystalline carbon nanostructures such as fullerenes,[16] single[17] or multiple walled carbon nanotubes[18] or graphene[19] exhibit unprecedented physico-chemical properties. In addition to all these crystalline forms of carbon, amorphous carbon is another allotrope. Amorphous carbons are polycrystalline materials of graphite or diamond possessing no long - range crystalline order. Examples of amorphous carbons are carbon black, activated carbons, glassy carbons, soot, chars etc. (Figure 1.2).

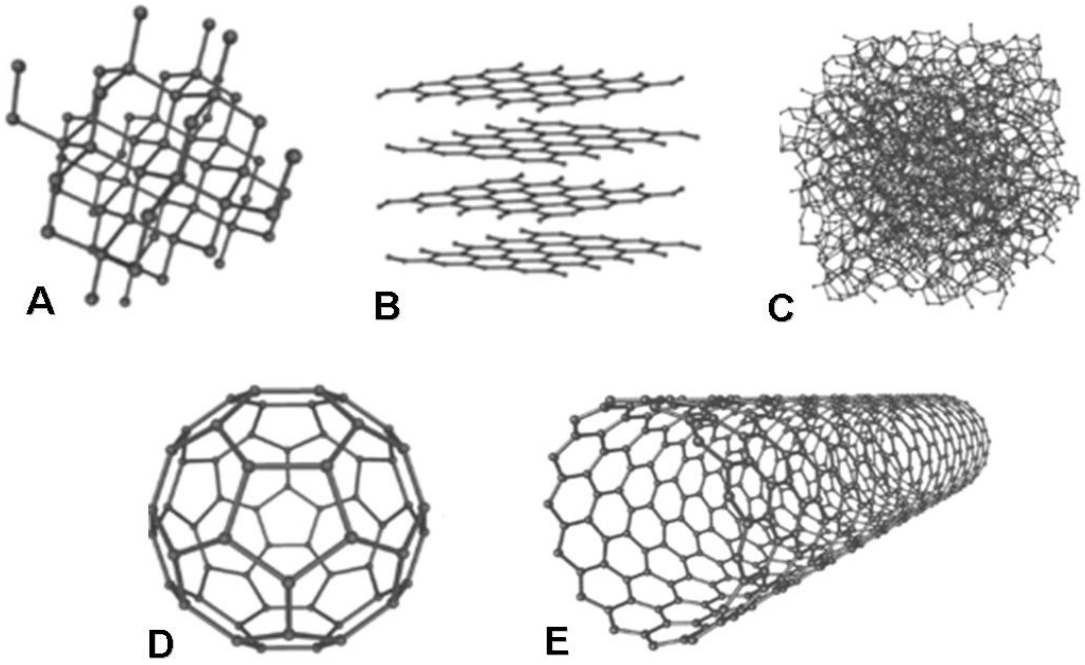

Figure 1.2: The allotropes of carbon: (A) diamond, (B) graphite, (C) amorphous carbon, (D) fullerene, and (E) carbon nanotube.[20]

The majority of carbon materials used in the aforementioned applications is typically synthesised through the heat treatment of carbon-rich organic precursors. Such a process is called "carbonisation". These precursors undergo a thermal decomposition (pyrolysis), which eliminates volatile compounds that include heteroatoms and become carbon-rich. Upon increasing temperature, condensation / charring reactions occur and localised aromatic units grow and become aligned into small microcrystallites (Figure 1.3). Depending on the temperature employed, such microcrystallites can arrange into a hexagonal lattice, parallel to one another, an arrangement commonly known as turbostratic carbon. This approach is normally applied to generate amorphous carbons, whereas more crystalline materials (e.g. nanotubes) are often produced through more complicated / expensive techniques such as laser ablation,[21] electro-arc discharge[22] or chemical vapor deposition[23] usually employing high temperatures (> 1000 ^{o}C) and therefore accessibility and sustainability of the procedure is somewhat limited.

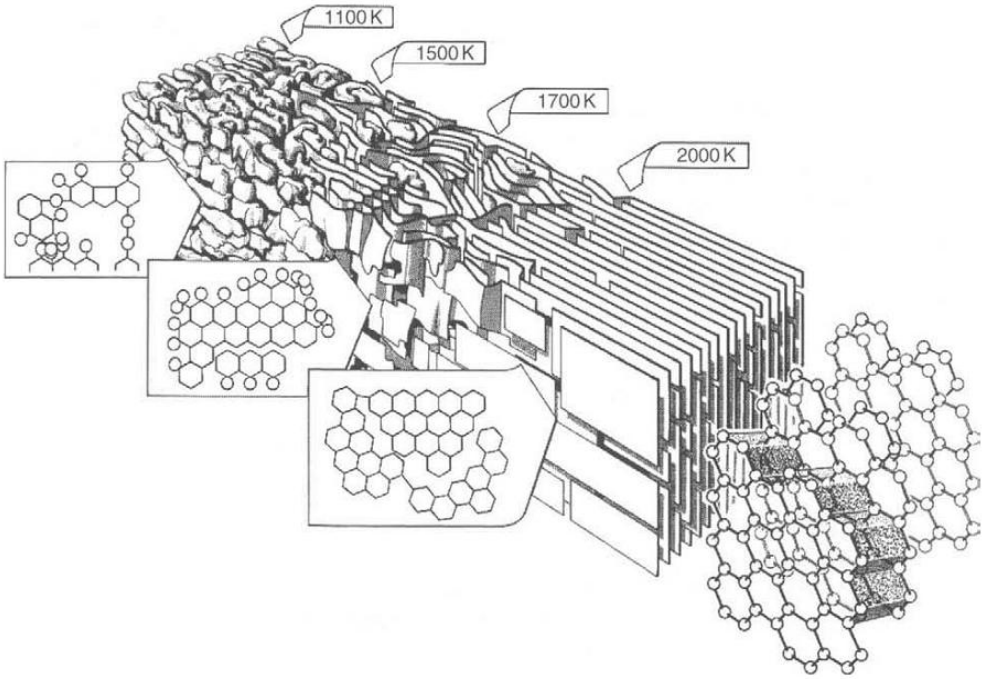

Figure 1.3: Structural changes in the carbon microstructure during carbonisation.[24]

Contrary to all these high temperature procedures, the recently rediscovered hydrothermal carbonisation (HTC) procedure offers new perspectives being performed from renewable resources (e.g. biomass and its derivatives) at low-temperatures (e.g. 130 – 200 °C) in aqueous phase and under self-generated pressure. Although known since 1913, when Bergius demonstrated hydrothermal transformation of cellulose into coal-like materials,[25] this technique has received much interest since 2000 and has been extensively investigated for the production of various hydrothermal carbons with a wide range of applications.[26,27,28] In this synthetic HTC procedure, the carbon precursor firstly dehydrates to 5-hydroxymethyl-furfural, followed by subsequent condensation / polymerisation reactions, to form a carbon-rich material consisting of interconnected aromatised carbon cores composed of polyfuran-type units, with the surfaces essentially terminated by a rim of functional polar groups, rendering their surfaces relatively hydrophilic.[29,30,31] This synthesis route allows the facile and direct preparation of monodisperse carbonaceous spherical particles in the micrometer size range in a one-pot procedure. However, an open question remains concerning the porosity of these carbonaceous materials, as conventional HTC material prepared in this straightforward aqueous based synthesis presents very limited surface area and pore volumes, which in

turn limits their efficient application and performance in the aforementioned application fields. Due to this limitation this thesis focuses on the development of synthetic routes to introduce well-defined porosity into hydrothermal carbonaceous materials. Furthermore, mechanistic investigations regarding the formation of pores in said carbon nanostructures and the preparation and study of carbon materials with tuneable surface chemistry will also be presented.

In relation to the introduction of porosity into carbon materials, Knox *et al.* (1986) was one of the first to synthesise nanoporous carbon materials with a variety of pore structures using the appropriate nanostructured silica materials as sacrificial templates.[8] This procedure reflects the "nanocasting"[32] approach to structure replication and is more specifically called exo-templating or hard-templating. Generally, in exo-templating, a carbon precursor infiltrates a sacrificial hard template structure and carbonised in the pores, followed by template removal to give the inverse nanostructures of the original inorganic templates.[32,33,34] Besides this very well known technique, more recently, Zhao *et al.* and Dai *et al.* have independently demonstrated that under the correct synthesis conditions, the use of a sacrificial inorganic template is not required, demonstrating a direct route to ordered porous carbon materials *via* organic-organic self-assembly of block copolymers and a suitable aromatic carbon precursor (e.g. phloroglucinol or resorcinol-formaldehyde).[35,36,37,38,39,40] This method, widely recognised as one of the classical methods to produce inorganic porous materials by sol-gel chemistry, is called endo-templating or soft-templating.

In this thesis, these templating methods are employed for the introduction of porous properties into the hydrothermal carbonaceous materials at the nanoscale. In this context, the hydrothermal process has clear advantages when compared to the classical carbonisation method (pyrolysis) since it takes place in an aqueous phase and thus can, in principle, be easily combined with the presented templating approaches. Pure carbohydrates are in this case the most convenient precursors since they are easily dissolved in water. Additionally, polar functionalities are present on the materials surface allowing relatively facile further modification to be performed.[30] The post chemical modification of the obtained porous hydrothermal carbonaceous materials with useful chemical moieties (e.g. stimuli-responsive polymers) is also investigated. Furthermore, the presented routes to porous hydrothermal carbons also allows the facile control of surface functionality and in turn carbon condensation / aromaticity (e.g. by post thermal

treatment), which extends the possible application of such materials to the aforementioned fields of heterogeneous catalysis, separation science and, when toxicity issue is cleared, biotechnology.

In the first part of this thesis, the hydrothermal carbonisation of carbohydrates in the presence of inorganic sacrificial templates will be presented. As will be shown this synthetic approach allows the production of mesoporous carbonaceous materials and carbonaceous tubular nanostructures using 2-furaldehyde as a carbon source, the dehydration product of the pentose D-Xylose.[29] Simultaneous control of pore properties and surface properties will also be highlighted. The second section is dedicated to the hydrothermal carbonisation of carbohydrate in the presence of amphiphilic block copolymers (i.e. endo or soft templating techniques). The aim of this study is the production of ordered porous carbonaceous materials possessing useful functional surface chemistry. A cooperative self-assembly of the organic structural directing agent (e.g. block copolymers) and D-Fructose (biomass carbon precursor) under hydrothermal carbonisation process leads to the formation of an ordered hybrid phase composed of the block copolymers and the carbonaceous moiety, which after template removal, gives carbonaceous materials with ordered pore structure.

2. Nanostructured Carbonaceous Materials

2.1 Carbonisation Chemistry

2.1.1 Classical Carbonisation (Pyrolysis)

The majority of commercial carbon material used today is synthetic and can be conveniently described as "*engineered carbons*". These manufactured carbons typically have an amorphous structure often in combination with some degree of graphitic microcrystallinity.[41] Amorphous carbons can be considered as sections of hexagonal carbon layers with very little order parallel to the layers. The process of graphitisation consists essentially of the ordering and stacking of these layers parallel to each other and is generally achieved by high-temperature treatments (> 2500 ^{o}C). Between the extremes of amorphous carbon and crystalline graphite, a wide variety of carbon materials can be prepared and their properties tailored for specific applications (e.g. turbostratic carbon; Figure 1.3).

Carbon materials are derived from organic precursors with high carbon contents (e.g. phenol-formaldehyde) or hydrocarbons (e.g. CO, CH_4, C_2H_2) synthesised most commonly through the thermochemical decomposition in an oxygen-free atmosphere at temperatures typically in excess of 500 ^{o}C. The final properties of these carbons are dependent on a number of critical factors such as the carbon precursor, its dominant aggregation state during carbonisation in the gas, liquid, or solid phase, processing conditions, and the structural and textural features of the product.[42] A variety of carbon

materials synthesised with different carbonisation conditions are summarised in Table 2.1.

Table 2.1: Common precursors and controlling production factors for various classes of carbon materials.[11]

Carbon material (phase during aggregation)	Common precursors	Controlling production factor	Structural/textural feature
Gas phase			
Carbon blacks	Hydrocarbon gas or liquid	Precursor concentration	Colloidal/nanosized
Pyrolytic carbon	Hydrocarbon gas	Deposition on a substrate	Preferred orientation
Vapour-grown carbon fibres	Hydrocarbon gas	Presence of a catalyst	Catalyst particle size/shape
Fullerene	Graphite rod	Condensation of carbon vapour	Nanosize molecule
Nanotubes	Hydrocarbon vapour	Condensation of carbon vapour	Single wall, multi-wall, chiral
Liquid phase			
Cokes	Coals, petroleum pitch	Shear stress	Mesophase formation and growth
Graphite	Petroleum coke	High temperature	Mesophase formation and growth
Carbon fibres (pitch derived)	Coal pitch, petroleum pitch	Spinning	Mesophase formation and growth
Solid phase			
Activated carbons	Biomass, coals, petroleum coke, selected polymers	Carbonization/activation	Nanosize pores
Molecular sieve carbon	Selected biomass, coals, polymers	Selective pore development	Nanosize pore/constrictions
Glass-like carbons	Thermosetting polymers (e.g., polyfurfuryl alcohol)	Slow carbonization	Random crystallites, impervious
Carbon fibres (polymer derived)	Selected polymers (e.g., polyacrylonitrile)	Slow carbonization	Random crystallites, non-porous
Highly oriented graphite	Pyrolytic carbon, poly-imide film	High molecular orientation	Highly oriented crystallites

A description of classical carbonisation can be found in many review papers and textbooks.[5,11,42] In classical carbonisation, the carbon precursor goes through a thermal decomposition (pyrolysis), which eliminates volatile materials that include heteroatoms. With increasing temperature, condensation reactions are initiated and localised graphitic units begin to grow and align into small "graphite-like" microcrystallites (e.g. stacking of aromatic layers or "graphene-like sheets"). The carbon precursor and processing conditions used will determine the size of such graphene sheets, the stacking number of graphene sheets and the relative orientation of the crystallites. The size and orientation of the crystallites are very important as they define the materials' texture and the degree of electrical conductivity.

Some carbon precursors (e.g. petroleum pitch, coal pitch, carbonisable polymers) pass through a fluid stage referred to as mesophase during the initial carbonisation stages. This allows large aromatic molecules to align with each other and form a more extensive pre-graphitic structure. Upon further high temperature treatment (> 2500 ^{o}C), these carbons are converted into highly ordered graphite and referred to as graphitising carbons. Other carbon precursors retain a solid phase during carbonisation, and the limited mobility of the crystallites leads to the formation of a rigid amorphous structures that consist of randomly-oriented graphene layers.[2] These materials cannot be readily converted to graphite by further high temperature treatment and are as such referred to as

non-graphitising carbons. Non-graphitising carbons are typically produced from precursors such as biomass, non-fusing coals and many thermosetting polymers (e.g. polyvinylidene chloride). The loss of volatiles and the retention of a rigid and complex molecular structure during the carbonisation of many non-graphitising carbons can lead to a highly porous structure without the need for further activation.

2.1.2 Hydrothermal Carbonisation

2.1.2.1 Overview of Hydrothermal Carbonisation

Hydrothermal carbonisation is an aqueous phase based route to carbonaceous materials using water-soluble carbon precursors typically carbohydrates or their derivatives but also raw agricultural biomass.[26,29] The synthesis is carried out in an autoclave at moderate temperatures (< 200 ^{o}C) and under self-generated pressures (< 10 bar) to typically yield a solid carbonaceous precipitate. It is considered that under such conditions water splitting plays an important role in catalysing the reaction.[43] The reaction mechanism consists of an initial dehydration of the carbohydrate and subsequent polymerisation / aldol-condensation of the dehydration product(s) (e.g. 5-hydroxymethyl-furfural) towards a carbon-rich phase. Detailed mechanism will be explained in the next subchapter. The process is significantly different from classical carbonisation methods giving the resulting materials a unique chemical character. The advantages of hydrothermal carbonisation can be summarised as:-

1) Low carbonisation temperatures
2) Aqueous phase synthesis
3) Inexpensive renewable precursors (e.g. carbohydrates, their dehydration derivatives or raw biomass) used as carbon sources.
4) Simple one pot ability to incorporate other important chemical structures such as nanoparticles or functional monomers.
5) Easy access to material with useful, easily transformable functional surfaces (e.g. hydroxy, carbonyl, carboxyl, lactone, and olefinic groups), allowing simple post-chemical modification (e.g. functional polymers).

The history of the hydrothermal carbonisation process dates back to the beginning of 1910s. In 1913, Bergius and his co-workers reported the hydrothermal transformation of cellulose into coal-like materials. In 1928, in his paper titled "Beiträge zur Theorie der Kohleentstehung" Bergius presented the hydrothermal carbonisation of carbohydrates demonstrating the geological process (e.g. transformation of carbohydrate to coal) as a chemical process on the laboratory scale performed during a time-scale of two to three days. The reaction was conducted using cellulose, wood, grass, sugar and peat as carbon precursor(s) in H_2O at 250 - 300 ^oC through multi-step dehydration and the degree of carbonisation was determined by elemental analysis.[25] More systematic investigations were performed by Berl and Schmidt in 1932, by varying the biomass source and performing the HTC at temperatures between 150 and 350 ^oC.[44] Later, Schuhmacher *et al.* analysed the influence of *p*H on the outcome of the hydrothermal carbonisation reaction and found serious differences in the decomposition schemes, as identified by the difference in C/H/O composition.[45]

Due to the increasing demand for high-performance carbonaceous materials in materials chemistry and nanotechnology applications, this facile aqueous procedure has been attracting attention once more in the new century. In 2001, Huang *et al.* utilised this hydrothermal carbonisation method to successfully produce monodisperse carbon spheres with the size of 1 - 5 μm from a sugar solution at lower synthesis temperature (e.g. 190 ^oC).[38] This aqueous based formation of carbonaceous spherules is considered more similar to the conventional emulsion polymerisation mechanism of colloidal particles. Here, partially dewatered carbon precursors (e.g. sugar) form an aqueous emulsion, where further dehydration of the sugar precursor leads to the appearance of nuclei-oligomers within the emulsion in the form of tiny particles. These nuclei gradually grow up into nano-scaled spherules and precipitate as carbon particles. Following this work, a variety of hydrothermal carbons have been produced, leading to the formation of nanoparticles encapsulated by colloidal carbon microspheres,[28] metal/carbon nanoarchitectures (e.g. Ag@carbon nanocables,[46] Ag@carbon-rich composite microcables[47]), and many others.[26] The syntheses of different types of carbonaceous and carbon/metal composites such as a Si@SiOx/C nanocomposite,[6] Pd supported hydrothermal carbon,[4] and carboxylate-rich[48] and imidazole-functionalised carbon spheres[49] for the applications as an anode material for lithium-ion batteries, catalyst in hydrogenation of hydroxyl aromatic derivatives, or adsorbents for metal ion species have also been recently reported.

In terms of pore properties and nanostructure of hydrothermal carbons, Huang *et al.* reported that the monodisperse carbonaceous spherules possessed a surface area of 400 $m^2 g^{-1}$ derived from a 0.4 nm - sized micropore inside the particles after the materials was further carbonised at higher temperatures (e.g. 1000 ^oC). However, methods to obtain more developed pore properties such as high(er) surface area or increased pore size / volume or to allow control in pore properties for the production of application-rich carbonaceous materials are yet to be fully established.

2.1.2.2 Mechanism of Hydrothermal Carbonisation

Open questions, however, remain regarding the influence of the carbohydrate precursor and a more detailed synthetic mechanisms behind the formation of hydrothermal carbon materials. Therefore, to gain information about the fundamentals of the hydrothermal carbonisation model systems have been studied using model carbohydrates precursors (e.g. D-Xylose and D-Glucose) and their decomposition products (e.g. furfural and 5-hydroxymethyl-furfural (HMF).[29,31] It was demonstrated that under hydrothermal conditions all hexose sugars, regardless of their complexity, degrade to a HMF intermediate, which finally condenses to a carbon-like material having similar morphologies and the same chemical and structural composition, independent of the starting precursor. By contrast, D-Xylose (i.e. a pentose) dehydrates to furfural, which in turn reacts to provide carbon structures very similar to those obtained from using a pure furfural precursor, which are importantly different from materials derived from the hexoses (e.g. a higher carbon content / aromatic structuring). Detailed ^{13}C solid-state NMR investigations have shown that starting from more complex "real-life" biomass, instead of pure sugars, does not change the overall outcome of the hydrothermal carbonisation reaction, and remarkable similarities between products of homologous carbohydrate series are observed with respect to morphology and local structural connectivity.[31] The hydrothermal carbonisation reaction essentially proceeds via three important steps (Figure 2.1):-

1) Dehydration of the carbohydrate to HMF or furfural

2) Polymerisation towards polyfurans

3) Carbonisation via further intermolecular dehydration.

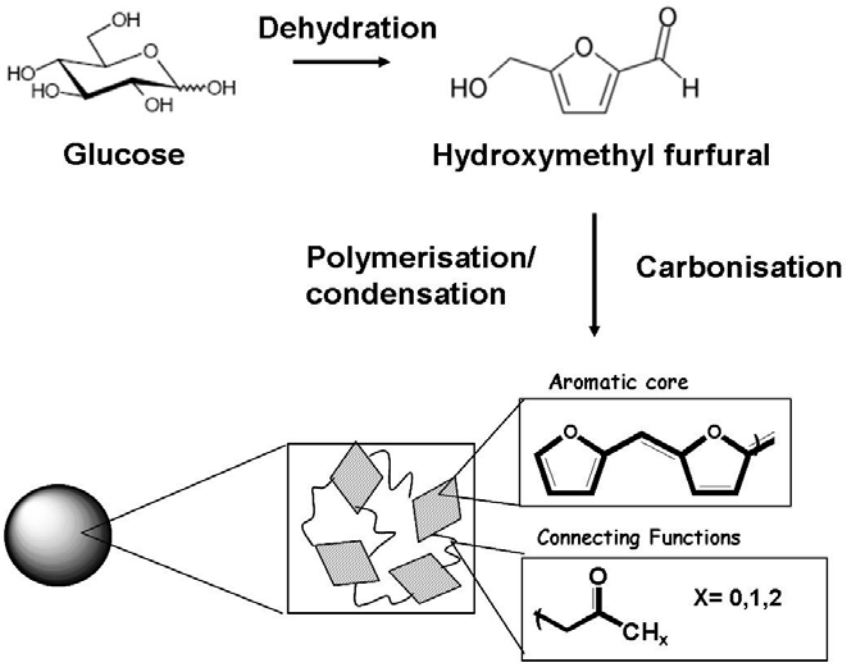

Figure 2.1: Proposed mechanism of reaction pathway of hydrothermal carbonisation from D-Glucose.[31]

Dehydration of D-Glucose to form HMF is more specifically described as the conversion of D-Glucose to 1,2-enediol through tautomerisation followed by further dehydration steps (Figure 2.2). The generated HMF then forms extended polyfuran-type aromatic core through polymerisation and condensation. Additionally, aliphatic sections which are derived from other types of dehydrated D-Glucose through aldol condensation, operate as the main bridge between the aromatic core and chemical functions at the materials surface (Figure 2.3).

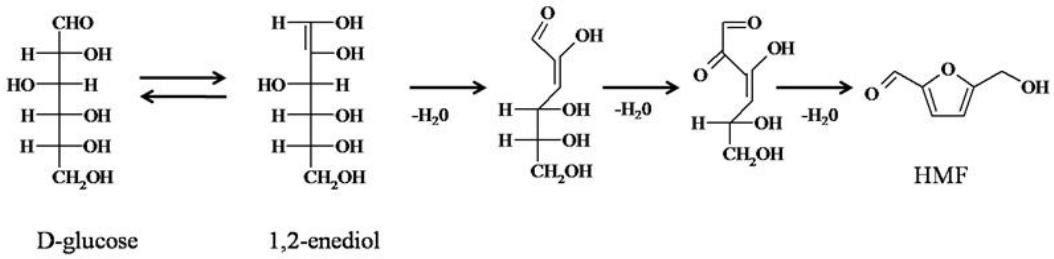

Figure 2.2: A generalised mechanism of dehydration of D-Glucose into HMF.[50]

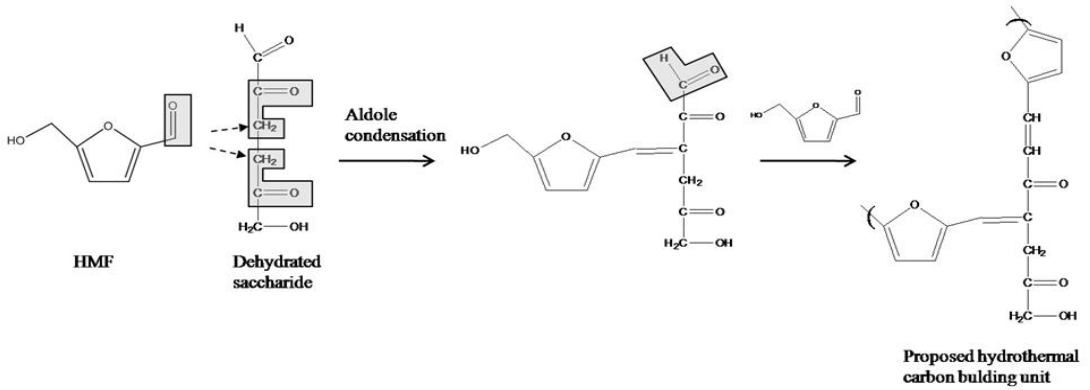

Figure 2.3: A proposed formation mechanism of polyfuran structure.[51]

Hydrothermal carbons obtained from soluble, non-structural carbohydrates are micrometer-sized, spherically shaped particle dispersions, containing a sp^2-hybridized backbone (responsible for the brown to black colour) decorated with numerous polar oxygenated functional groups partially retained from the parent carbohydrate. The presence of these surface groups offers the possibility of facile post-functionalisation and makes the material more hydrophilic and easily dispersible in water. The size of the final particles depends mainly on the carbonisation time and precursor concentration as well as on additives and stabilisers that may be added to the initial reaction mixture. Thus, the obtained hydrothermal carbons represent a very unique character compared to carbon materials synthesised through classical carbonisation methods.

2.2. Nanostructured Carbonaceous Materials

Among a variety of porous solids (e.g. porous polymer, porous inorganic solids), porous carbon materials generally confer greater stability, *p*H resistivity, and higher mechanical strength. Additionally, upon graphitisation, carbon materials further confer electron conductivity which plays an important role in electrochemistry. There are a large number of different types of porous carbons and representative examples are discussed briefly below.

2.2.1 Activated Carbon

The process employed to increase surface area and porosity in the materials obtained from a carbonised organic precursor is referred to as "activation" and the resulting broad group of materials are referred to as "activated carbons". Carbon chars, a carbonised organic precursor, usually have a relatively low porosity and their structure consists of elementary crystallite with a large number of interstices between them. The interstices tend to be filled with "disorganised" carbon residues (tars) that block the pore entrances. Activation opens these pores and can also create additional porosity. Varying the carbon precursor and activation conditions (e.g. temperature, time and gaseous environment) allows some control over the resulting porosity, pore size distribution, and the nature of internal surfaces.

The activation process can be divided into two general categories: thermal activation and chemical activation. Thermal activation entails the modification of a carbon char by controlled gasification, and is usually carried out at temperatures between 700 and 1000 ^{o}C in the presence of a suitable oxidising gas (e.g. steam, carbon dioxide, air or mixtures of thereof). During gasification, the oxidising atmosphere increases the pore volume and surface area of the material through a controlled carbon "*burn-off*" and the elimination of volatile pyrolysis products. Chemical activation is usually carried out at slightly lower temperatures (~ 400 - 700 ^{o}C) and involves the dehydrating action of certain agents such as phosphoric acid, zinc chloride and potassium hydroxide. Exceptionally high surface area materials (> 2500 m^2 g^{-1}) have been prepared using potassium hydroxide activation techniques.[52]

2.2.2. Carbon Aerogels from the Carbonisation of Organic Aerogels

Carbon aerogels are highly porous materials prepared mainly by the pyrolysis of organic aerogels. They are usually synthesised by the poly-condensation of resorcinol (R) and formaldehyde (F), via a sol-gel process and subsequent pyrolysis.[53,54] A thorough review is found in the literature.[55] The reaction can be divided into the following three steps: gelation of a sol mixture, drying of wet gel, and carbonisation of dried gel. In the first step, molar ratio of R and F has a profound effect on the properties of the gel. The solvent can be either water or organic solvents and catalysts (e.g. sodium carbonate or acidic catalysts) can be added. The main reaction of R and F includes addition reaction of F to 2-, 4-, and / or 6- position on the aromatic ring of R. This gives place to hydroxymethyl

derivatives. Subsequently, these derivatives undergo a condensation reaction to form methylene and methylene ether bridged compounds. This reaction is catalysed in acid media. The condensation products form clusters that give rise to colloidal particles and, finally, to the wet gel or hydrogel. Here, the most important factors that control the properties of the organic gel are the concentrations of catalyst and reactants and the initial *p*H. The wet gel must be in the second step dried with supercritical fluids to preserve its structure, where liquid CO_2 is widely used. Then, in the third step, carbonisation of the dried aerogel is carried out by heating the sample in flowing N_2 or Ar at a temperature between 500 – 2500 ^{o}C. During carbonisation, the aerogel loses oxygen and hydrogen functionalities and there is an enrichment in carbon giving a high carbon content material structure. Such carbon aerogels derived from this pyrolysis approach possess high porosity, high surface area (400 - 1000 m^2 g^{-1}) and uniform pore sizes (largely between 2 and 50 nm). They can be produced as monoliths, composites, thin films, powders or micro-spheres. Possessing high surface area and electroconductivity, carbon aerogels are one of the most promising materials as electrodes in supercapacitor or fuel cells.

2.2.3. Carbon Aerogels from Biomass Derivatives

Clark *et al.* demonstrated the production of carbon aerogels from polysaccharide[56] (e.g. high-amylose corn starch,[57,58] alginic acid[59] and pectin[60]) providing the opportunity to produce a wide range of mesoporous carbonaceous materials, with textural properties reflective of the porous polysaccharide precursor (e.g. mesoporous starch) and surface / bulk chemistry intermediary between the polysaccharide and classical activated carbons. The procedure is not only technically gentle and is based on the gelation of biomass-derived polysaccharides. First, a simple process of gelation in water opens up and disorders the dense biopolymer network, after which it partially recrystallises during a process of retrogradation to yield a porous gel. Exchanging water with a lower-surface-tension solvent such as ethanol prevents collapse of the network structure during the drying process. After drying the expanded porous polysaccharide is obtained. To convert to a carbonaceous equivalent, using the example of mesoporous starch, the neutral porous polysaccharide is doped with a catalytic amount of organic acid (e.g. *p*-toluenesulfonic acid) and is heated under vacuum to enable fast carbonisation and fixing of the mesoporous structure. Importantly, heating at different temperatures (e.g.

from 150 to 700 ^{o}C) gives a variety of mesoporous materials from amorphous carbons to graphite-like activated carbons. In parallel, surface functionalities can be also controlled showing oxygenated surface functionalities such as carbonyl groups and vinyl ethers groups at lower carbonisation temperature and more aliphatic and alkene / aromatic functions at higher carbonisation temperature. When using acidic polysaccharides (e.g. pectin or alginic acid), the use of a carbonisation catalyst is not required, whilst the use of different polysaccharides allows in part tailoring of micro / mesoporosity properties. Thus, this Starbon® method allows the flexible control not only in surface functionalities and carbon network structures, but also in pore properties simultaneously.

2.3 Nanocasting Methods

Whilst the presented porous carbon materials represent high surface area and high porosity, synthesis still relies on artful manipulation of synthesis parameters and not so much on design principles by which a more detailed adjustment of the properties of the materials was possible in terms of control in surface area, porosity, pore size and so on. More precise manipulation has been demonstrated via “nanocasting” approaches for the synthesis of porous inorganic materials, organic materials and carbon materials.[32] When templates are used in the synthesis of porous solids, two different modes in which the template can act can be distinguished, namely soft-templating and hard-templating which will now be briefly discussed (Scheme 2.1).

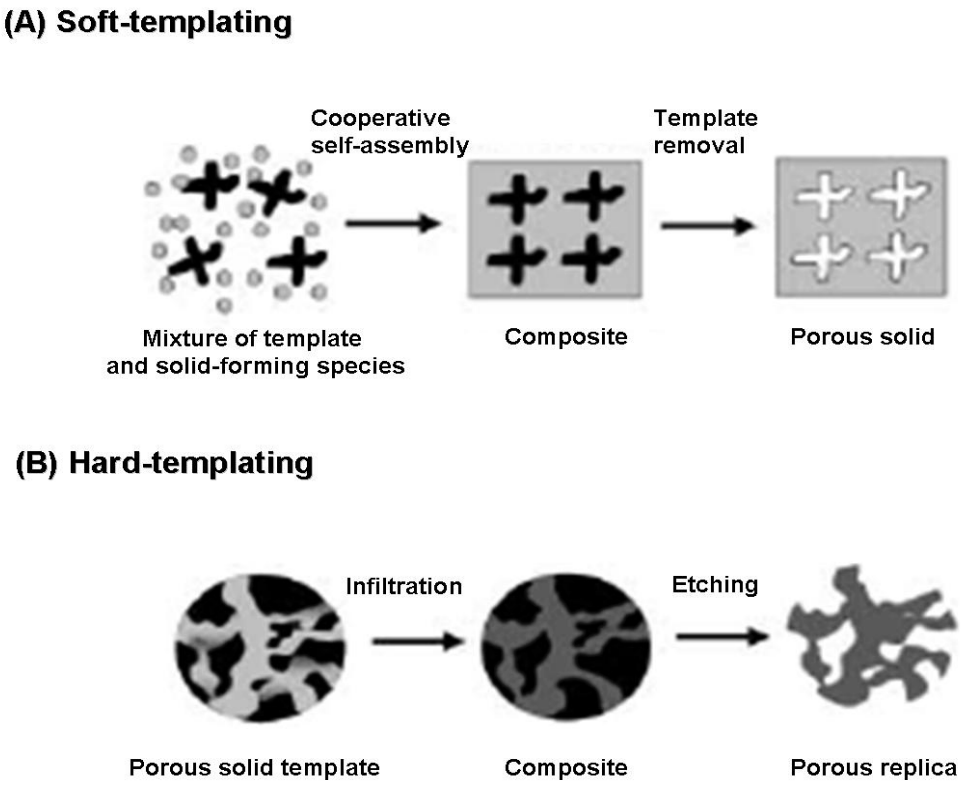

Scheme 2.1: (a) Soft-(endo-) templating and (b) hard-(exo-) templating methods.[32]

2.3.1 Soft-Templating (Endo-Templating)

Soft-templating creates voids in a solid by inclusion of molecular or supramolecular template species (e.g. surfactants or block copolymers) which occupies a specific void space around which the growing solid phase is built (Scheme 2.1.a). If afterwards the template is removed, the space is made accessible and a pore system develops. The sizes of the voids can range from the molecular scale, where molecules are used as templates, to the macroscopic scale. The mechanisms by which the pore systems develop are diverse. However, it is clear that there needs to be a favourable interaction between the templating species and solid to be templated (e.g. hydrogen bonds or ionic interactions).

The two major discoveries in developing porous solids via the soft-templating approach are zeolites and mesoporous silica materials. In zeolite syntheses, structure - directing agents (e.g. organic cation or hydrated metal ion) are templated with an alumina source and a silica source to form crystalline microporous aluminosilicates.[32,61] This is a molecular templating, where one molecule / ion occupies one space and then after template removal generates a pore with diameter at the molecular scale (e.g. 0.1 – 2 nm).

The formation mechanism is somewhat controversial and there are several roles of template species suggested:-

1. The framework forms around the template molecule which determines the shape and size of the later voids in structure;
2. Template species can just be a space filler which occupies the voids between the framework constituents and thus contributes to the energetic stabilisation of a more open structure compared to the denser structure;
3. It may control the equilibrium in the synthesis mixture, such as *p*H value or complexation structure;

   or
4. It can pre-organise solution species to favour nucleation of a specific structure.

Synthesis of mesoporous materials such as mesoporous silica involves templating species such as surfactant micelles or block copolymer micelles, whereby the polymers act as true templates, as the lyotropic ordered phase of those structures essentially directs the pore structure of the final mesoporous material. Also a cooperative self-assembly of a structure directing agent and a precursor species can form an ordered phase in a diluted solution to yield precipitates. The template can be removed by thermolysis or solvent extraction. Scientists of Mobil Oil Company disclosed the synthesis of the M41S materials in 1992, and the classical example of MCM-41, a hexagonal arrangement of hexagonal pore channels which have a diameter of about 4 nm, much bigger than that of zeolite materials.[62,63] In the case of M41S series, lyotropic liquid-crystal arrangement of surfactant is surrounded by the silicate ions, which then condense to form the siliceous framework. Using this pathway, it is possible to synthesise ordered porous materials with pore sizes in the range of 2 - 10 nm. Here, ionic interaction between an ionic surfactant and a silica precursor species (e.g. silicon alkoxide) is believed to play a role in the formation of the regularly ordered phase and this process is believed to be a cooperative process of these two species. Later, Stucky *et al.* successfully synthesised ordered mesoporous silica materials using non-ionic surfactants (e.g. Pluronics®, Triton®, Tween® etc.) providing materials with thicker pore walls and so a better thermal stability and also a wider range of controllable pore sizes.[64] In this case, a silica precursor species and a template species interact with each other through hydrogen

bonding to form an ordered phase.[65,66] These approaches have now been extended to the preparation of a range of porous metal oxides including the synthesis of porous titanium dioxide through a cooperative self-assembly pathway.[67]

As far as carbon materials are concerned, soft-templating method for the purpose of synthesising ordered porous carbon materials is still a relatively new area. Recently, Zhao's group and Dai's group independently demonstrated the soft-templating method using a cooperative self-assembly of a block copolymer and a resorcinol and a phloroglucinol carbon precursor, respectively. This will be described further in the chapter 5.

2.3.2. Hard Templating (Exo-Templating)

Opposite to soft templating, in hard templating a pore structure of a preformed rigid porous solid (i.e. the hard template) is replicated by an added / infiltrated liquid or gaseous precursor species (Scheme. 2.1.b). Typically, the precursor can be incorporated into the pores by sorption, phase transition, ion exchange, complex or covalent grafting. Upon heat treatment, the precursors are thermally decomposed and a composite of a template and a forming solid species is formed. The hard-template can be then removed mainly by acid etching to give a negative replica of a template structure. This method, in particular, allows the synthesis of different types of structures depending on those of preformed porous solids such as (ordered) mesoporous silica and zeolite and is very versatile (please see review by Yang and Zhao for further details).[68] As far as the hard-templating synthesis of mesoporous carbons is concerned, in 1999 Ryoo *et al.* first reported the synthesis of a highly ordered porous carbon material by replicating the structure of mesoporous silica (e.g. MCM-48, SBA-15) to yield a highly ordered porous carbon replica.[33] To be specific, in this example sucrose was used as an efficient carbon precursor and could be completely incorporated into the channels of mesoporous silica templates by a controllable two-step impregnation process. After carbonisation of the precursors at 900 ^{o}C and dissolution of the template using HF (aq) solution, the obtained materials maintained the macroscopic morphology and ordered mesostructure of the template. Among different types of mesoporous carbon replicas, CMK-3[69] was the first report of a true replica mesostructure, which was templated by SBA-15 and presented pore volume and surface area values of 1.3 $cm^3\ g^{-1}$ and 1520 $m^2\ g^{-1}$, respectively. Since

this first report, a wide variety of porous carbon materials have been synthesised employing a wide range of hard templating media (Table 2.2).

Table 2.2: Summary of reported mesoporous carbon materials.[68]

Silicate template	Ordered mesoporous carbon	Precursor	Space group
MCM-41	Hexagonal carbon nanowire arrays	Sucrose	*P6mm*
	Self-supported nanowire arrays	Furfuryl	Partially ordered
MCM-48	CMK-1	Sucrose	$I4_132$ or lower
	CMK-4	Acetylene	$Ia\bar{3}d$
SBA-15	CMK-3	Sucrose	*P6mm*
	CMK-5	Furfuryl	*P6mm*
	G-CMK-3	Acenaphthen	*P6mm*
	Graphitized CMK-3	Mesophase pitches	*P6mm*
SBA-16	Spherical mesoporous carbon	Sucrose	$Im\bar{3}m$
SBA-3	Small pore ordered mesoporous carbon	Sucrose	*P6mm*
SBA-1	CMK-2	Sucrose	Unknown
FDU-5	Monolithic mesoporous carbon	Sucrose	$Ia\bar{3}d$
	Tubular mesoporous carbon	Furfuryl	$Ia\bar{3}d$
FDU-12	Spherical mesoporous carbon	Sucrose	Unknown
KIT-6	CMK-4	Sucrose	*Ia3d*
	Graphitized CMK-4	Mesophase pitches	$Ia\bar{3}d$

The hard templating method in principle allows precise control of pore volume and pore size, but compared to the soft-templating method, this replication approach is somewhat technically complicated requiring the synthesis of the inorganic hard-template initially and also a highly acidic solution such as HF (aq) for the removal of inorganic templates, making the overall process relatively resource consumptive. Furthermore, the carbon materials produced in this manner are typically chemically inert – a requirement to withstand the strong acid treatment in the template removal step – and as such post-synthesis chemical modification is a challenge.

3. Characterisation Techniques

3.1 Electron Microscopy

3.1.1 Transmission Electron Microscopy (TEM)[70]

The TEM instrument was first developed by Ruska, von Borries and Knoll in 1935. It won Ruska a Nobel Prize in 1986. In general, electron microscopy represents the technique based on stigmatic imaging by electronic lenses and TEM is the oldest technique among them. In a typical TEM machine set-up, electrons are generated by an electron gun with tungsten or LaB_6 filament and then accelerated through a positive stabilised voltage V_0 (10 - 120 keV) under vacuum (Figure 3.1). A conventional thermoionic electron gun associated with a double condenser system operated in the focusing mode on the specimen generates a probe of the order of 1 μm in diameter and 1 μA in intensity. Additional condenser lenses (e.g. condenser objective) lead to a minimum beam diameter of some 1 nm with the intensity of some 1nA, notably combined with a LaB_6 source or a field emission source.

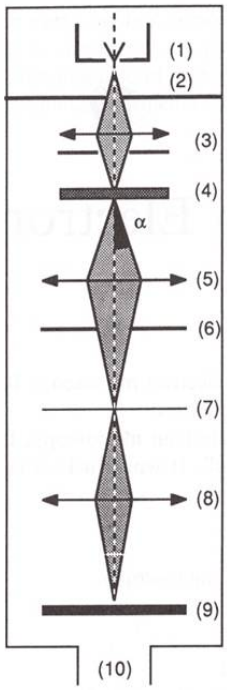

Figure 3.1: Basic components of a TEM instrument. (1) Electron source at a voltage V_0; (2) grounded anode; (3) condenser system; (4) thin specimen; (5) objective lens; (6) objective back focal plane; (7) objective image plane; (8) projection lenses; (9) photographic film; (10) vacuum pumps.

Lenses used in the electron microscope are mainly magnetic lenses with a stabilised input. Electron lenses have characteristics which are quite similar to those of conventional lenses with parameters such as the focal length and the aberrations. Focal length is given by:

$$\mathbf{1/f = (k/E_0) \int_{gap} Hz^2\, dz} \qquad \mathbf{(3.1)}$$

Where k = a constant, E_0 = the voltage of electron source, and Hz is the axial component of the magnetic field in the pole piece gap. Convergence (1/f) increases continuously with increasing lens current, resulting in a zoom effect.

Resolution of a TEM is defined as:

$$\mathbf{d = 0.61 \cdot \lambda / (n \cdot \sin\alpha)} \qquad \mathbf{(3.2)}$$

Improving the resolution means reducing the resolution distance d, which may be achieved in the following three ways:-

(a) reducing wavelength λ (e.g. UV microscopes)
(b) increasing aperture α
(c) increasing refractive index n.

A TEM can be operated in the two different operating modes; an imaging mode and a diffraction mode. The imaging mode exploits the lowest illumination coherence, where the electron beam is focused onto the specimen, thus resulting in the maximum beam aperture. This focusing mode reduces diffraction effects and is suitable for imaging with high-point resolution. The diffraction mode is operated with the highest illumination coherence which is achieved by over-focusing the beam, resulting in the reduced beam aperture. This mode increases the diffraction effect and is suitable for periodic imaging like electron diffraction.

In order to be observable, an image must display a contrast. In a TEM, the specimen acts on the transmitted beam through absorption and scattering. The scattering effect is prominent for image contrast and transmitted electron waves differ mainly in direction from one point to another of the specimen. It also depends on the electron density of the sample and for example area containing heavy metal appears dark due to scattering of electrons in the sample.

3.1.2 High Resolution Transmission Electron Microscopy (HR-TEM)[70]

HR-TEM enables us to reach to structure resolution of a unit cell scale, organic and biological molecules and single atoms. When the resolution distance becomes smaller than crystal parameters (or atomic distances in an amorphous solid), an additional structure-related contrast appears, which leads to the high-resolution electron microscopy.

In contrast to the normal TEM described above, the introduced primary electron beam is either diffracted or transmitted through the specimen and for this, the specimen should be placed so that the atom row orients itself almost parallel to the primary beam, where Bragg's condition applies. Diffracted wave and transmitted wave interfere with each other, where diffracted wave contains the information of atom orientation. The

diffracted and transmitted waves are brought together again to the objective lens. As the diffracted wave is the Fourier transform of the periodic potential for the electrons in two dimensions, the back transform of the interfering waves leads to an enlarged picture of the periodic potential. This image formation is called phase-contrast imaging where contrast is created by the interference of the waves. The obtained picture is magnified by the following electron-optical system and finally seen on the screen at magnification of typically 10^6.

3.1.3 Scanning Electron Microscopy (SEM)[70]

The basic technique of SEM was first assessed by Knoll in 1935. In SEM, scattered electrons are scanned by a deflection system, usually consisting of magnetic coils operated by a large-range scan generator. An SEM machine normally includes the following main components: electron source, scanning device, specimen on its stage, imaging system, and data processing (Figure 3.2). An electron beam is generated by negative high voltage and is introduced to the condenser lens system (usually consisting of two lenses). The probe size of the electron beam is decreased through these lenses and emitted to the sample. In the case of using a tungsten filament as an electron source, the intensity of probe is 10^{-12} to 10^{-11} (A) with 2 - 3 nm of probe size.

There are two operating modes in SEM, called secondary electron mode and back scattered electron mode, which differ in the types of electron that are captured at the collector field. Secondary electrons are generated through the energy loss of primary electrons and because of the low energy, these are easily attracted by the collector field. Moreover, the cross-section of the secondary electrons represents high signal-to-noise ratio being favourable for imaging. Back scattered electrons are generated by elastic scattering of primary electrons and represents high energy. Because of the straight path of the scattered electrons, its cross-section is smaller than that of secondary electrons. In the back scattered electron mode, secondary electrons are all captured at collector field and do not reach the scintillator. Thanks to their high energy, only back scattered electrons can be detected.

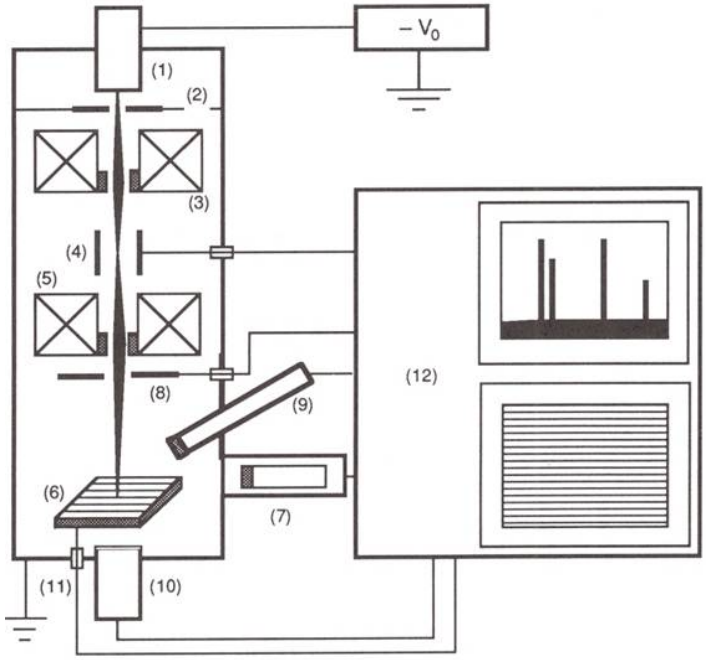

Figure 3.2: Basic components of an SEM instrument. (1) Electron source at negative high voltage ($-V_0$); (2) grounded anode; (3) condenser lenses; (4) beam deflection and scanning system; (5) objective lens; (6) specimen on a goniometric stages; (7) electron detector; (8) back scattered electron detector; (9) X-ray spectrometer (for energy dispersive X-ray spectroscopy); (10) transmitted electron detector; (11) absorbed current measurement; (12) data processing unit.

The scattered electrons then create an image via topographic contrast and composition contrast. The former is mainly due to inclination of the sample surface or shadowing effect. The latter varies as a function of composition of specimen like metal species, organic species. In the case of secondary electron mode, detected secondary electrons are only from thin surface layer (- a few nm) because of low energy. Therefore, contrast displayed in secondary electron mode is not related to the bulk composition of the sample, whilst that of back scattered electron mode represents bulk composition due to the high energy electron beam. Modern SEM machines are now capable of resolution in order of 3 – 10 nm with available magnification of 10 – 100000.

3.2 Small Angle X-ray Scattering (SAXS)[71]

Small Angle X-ray Scattering (SAXS) analysis is a technique for studying average structural features of in the colloidal range (1 - 100 nm, 2 theta = 0 – 2 ^{o}). The information obtained from the SAXS measurement contains shape, size and surface area of the particle as well as repeating unit of ordered materials with macromolecular range. For the determination of structures of nanoparticles, colloidal dispersions, macromolecules and ordered mesoporous materials, SAXS has been one of the strongest tools and has been widely accepted.

In a typical SAXS measurement set-up, X-rays can be generated from CuKα, Molybdenum, or Tungsten sources (Figure 3.3). A generated X-ray is collimated either by a series of slits or of pinholes and radiated to the sample. The scattered light (e.g. Compton scattering and Rayleigh scattering) is then detected by a CCD camera, wire detector (gas filled chamber) or image plates. The condition for the generation of scattering pattern follows Bragg's law. Thus, when the spacing of the regular structure is *d*,

$$\mathbf{2 \cdot \mathit{d} \cdot \sin(\theta) = n \cdot \lambda} \qquad \mathbf{(3.3)}$$

However, the unit d is not convenient for the interpretation of the obtained scattering pattern since it cannot be read directly from the scattering pattern such as a 2D scattering pattern obtained from a CCD camera. Instead, it is very common to use the unit $\vec{q}$, which is called "scattering vector". The scattering vector is used for converting the optical path difference d or ($\vec{r}$) to the difference in phases of incident and scattered waves (see Figure 3.4). $\vec{q}$ is defined as:

$$\vec{q} = \vec{k} - \vec{k}_0 \qquad \mathbf{(3.4)}$$

Here, optical path difference can be described as:

$$\mathbf{x = -\ \vec{r}\ (\vec{k} - \vec{k}_0)} \qquad \mathbf{(3.5)}$$

Optical path difference x is equivalent to difference of phases Δ φ, therefore:

$$\Delta\varphi = -\frac{2\pi}{\lambda}(\vec{r})(\vec{k} - \vec{k}_0) = -\vec{q} \cdot \vec{r} = -\frac{2\pi}{\lambda} \cdot \vec{r} \cdot 2\sin(\theta) \qquad (3.6)$$

Therefore, the scattering vector $\vec{q}$ is described as:

$$\vec{q} = \frac{4\pi}{\lambda}\vec{r}\sin\theta \qquad (3.7)$$

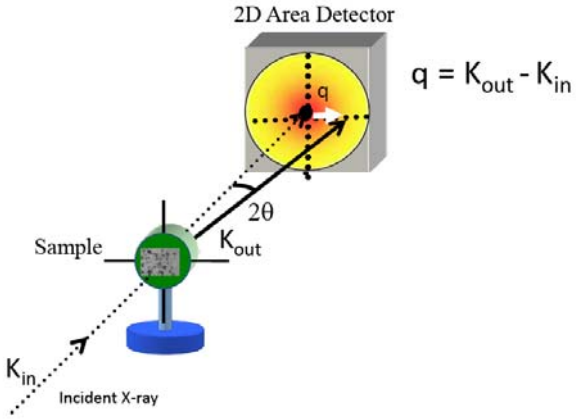

Figure 3.3: A general setup of a SAXS instrument.

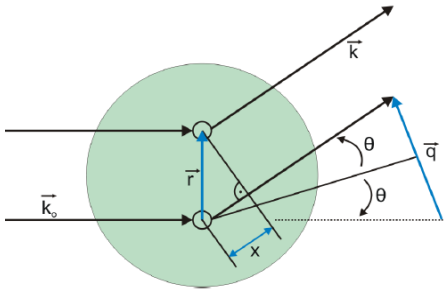

Figure 3.4: A scheme showing the generation of scattering vector $\vec{q}$.

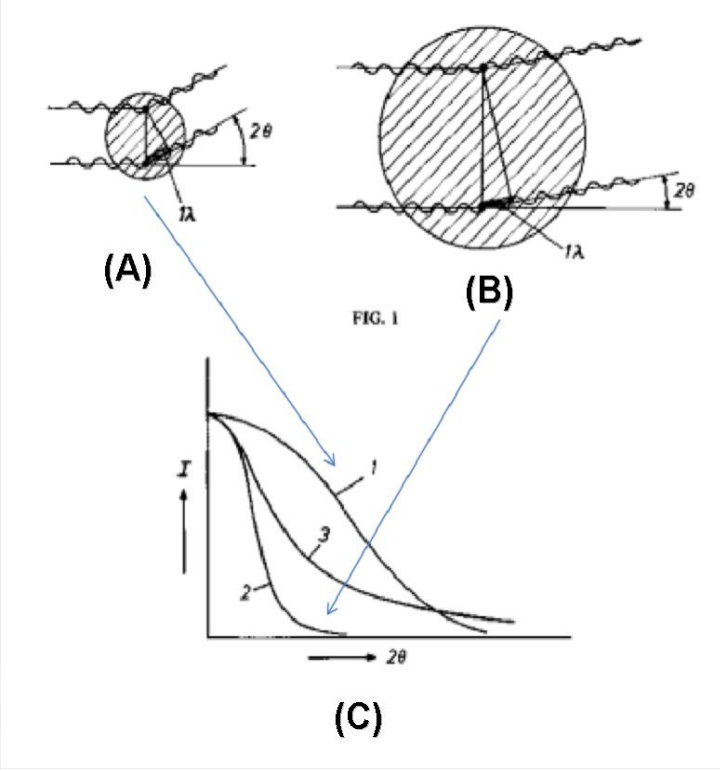

Figure 3.5: Model images of an incident beam and scattered wave; (a) from a small particle and (b) from a large particle. (c) Comparison of the SAXS patterns between (a) and (b).

In particular, scattered waves from regularly oriented macromolecular or colloidal systems interfere at small 2 theta angle (Figure 3.5.b) compared to smaller regular units (e.g. atomic order; (Figure 3.5.a)). It leads to the appearance of a scattering pattern at the smaller 2 theta angle (Figure 3.5.c). In addition, due to the relatively large regular unit, a SAXS instrument requires the precise collimation of the incident beam and the relatively long sample - detector distance for the precise detection of scattering pattern. Generally in SAXS measurements, the obtained scattering patterns are analysed in terms of the form factor ($P(\vec{q})$) and the structure factor ($S(\vec{q})$), where the total scattering intensity can be described as:

$$\mathbf{I}(\vec{q}) = \mathbf{K} \cdot \mathbf{P}(\vec{q}) \cdot \mathbf{S}(\vec{q}) \text{ (K=constant)} \qquad (3.8)$$

The structure factor appearing in the smaller q region represents an interference pattern of the scattering from the particles which are dependent on the particle size. In the case of homogeneous nanoparticles, the particle radius can be determined by the slope of Guinier's plot. In the intermediate q region, we observe the contribution of the form

factor, which is a specific oscillation pattern for each particle shape (e.g. spherical, rod-like), therefore giving information about the particle shape. In addition, in the region of a higher q value, it is possible to observe the contrast at the interface between the two media (e.g. particle and solvent). This region is called Porod's region and used to calculate the surface area of the particles (see reference 72 for further details).[72]

In diluted systems, scattering intensity can be also described as:

$$\mathbf{I}(\vec{q}) = \mathbf{i_0} \cdot \boldsymbol{\rho} \cdot \mathbf{V}^2 \cdot \mathbf{P}(\vec{q}) \qquad \textbf{(3.9)}$$

Where:

$\mathbf{i_0}$ = a scattering cross section of a single electron

$\boldsymbol{\rho}$ = electron density of a particle

$\mathbf{V}$ = particle volume

$\mathbf{P}(\vec{q})$ = form factor of a particle.

Thus, electron density of a sample and sample volume play important roles in obtaining scattering intensity in practical measurement. Besides, in order to be observable, a scattering pattern must display contrast on pictures obtained from the CCD camera. Scattering of dilute object assuming sharp interface is described as:

$$\Delta\mathbf{I}(\vec{q}) = \mathbf{i_0} \cdot (\Delta\boldsymbol{\rho})^2 \cdot \mathbf{V}^2 \cdot \mathbf{P}(\vec{q}) \qquad \textbf{(3.10)}$$

Where $\Delta\rho = \rho_{sample} - \rho_{matrix}$.

Therefore, an increased difference in electron density between sample and matrix leads to a more precise observation of the obtained scattering pattern.

As far as the SAXS analysis of ordered porous materials is concerned, Bragg peaks are derived from the repeating unit of the formed ordered structure (e.g. hexagonal, cubic, lamellar). For a better understanding, a porous solid with the hexagonal pore system is described (Figure 3.6). Bragg peaks appear at the positions according to the rules of hexagonal network described mathematically as:

$$\mathbf{d_{hk} = (h^2 + k^2 + hk)\ (1/2)} \qquad \mathbf{(3.11)}$$

Which gives the sequential ratio of peak positions of 1 (d_{10}) ; √3 (d_{11}) ; 2 (d_{20}) ; √7 (d_{21}),….

In this particular case, the diameter shown as d in Figure 3.6 is detected as a d_{10} face. Then the lattice parameter a is deduced from d_{10} by the relation, $a = 2 \cdot d_{10} / \sqrt{3}$. When, for example, the pore diameter is known from the nitrogen sorption isotherms, the pore wall thickness of the solid can be calculated by simply subtracting the former from the latter.

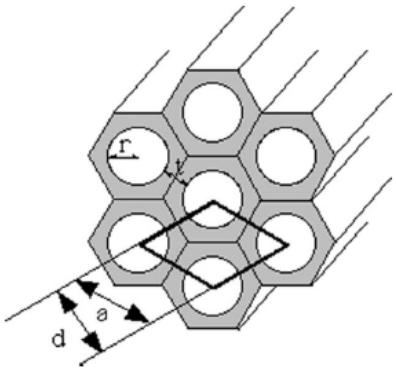

Figure 3.6: A model hexagonal pore system for the calculation of d and a.[73]

3.3 Gas sorption[74,75]

Gas sorption measurement is one of the most powerful tools to characterise the physicochemical properties of porous solids including the textural properties of porosity and surface area. Adsorption occurs whenever a solid surface is exposed to a gas or liquid through chemical and / or physical interaction(s) between an adsorbent and an adsorbate. Typically, nitrogen, argon, krypton or carbon dioxide are used as model adsorbates. In a basic set-up of the gas sorption experiment, typically, pressure and temperature of each dose of gas are measured and the gas is allowed to enter the adsorption bulb (Figure 3.7). After adsorption equilibrium has been established, the amount adsorbed is calculated from the change in pressure and results derived from the relation between relative pressure (p/p_0) and volume of adsorbed gas. Usually, nitrogen is used as an adsorptive and measurement temperature is kept at 77 K (i.e the boiling point of nitrogen) so that p_0 is kept the same as atmospheric pressure.

From analysis, sorption isotherms are obtained and allow the determination of surface area, pore volume, and pore size of the adsorbent (Figure 3.8).

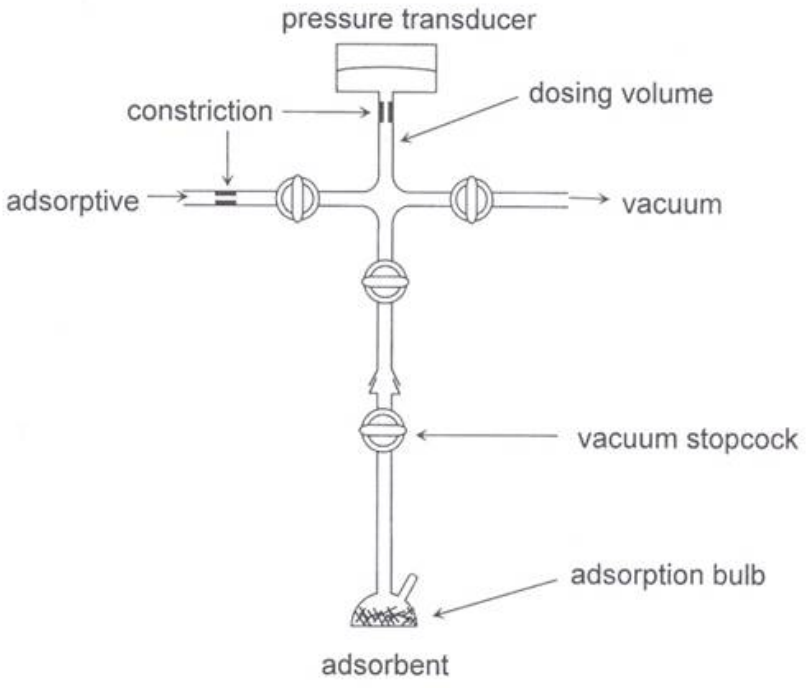

Figure 3.7: A basic setup of the gas sorption measurement.

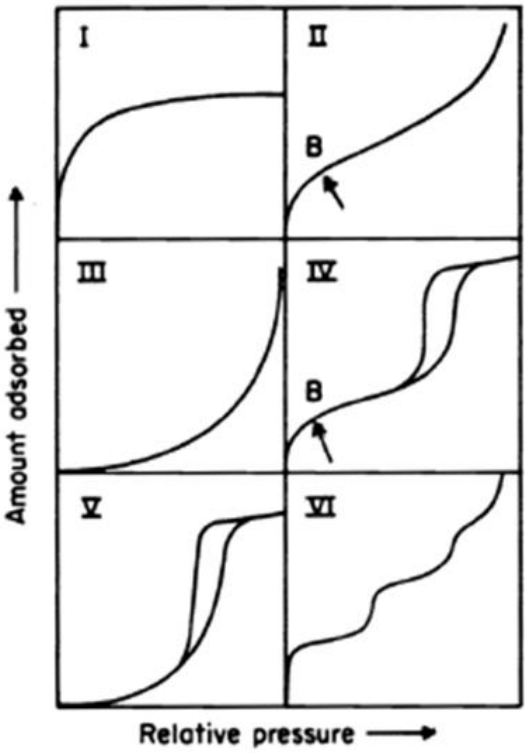

Figure 3.8: Different types of sorption isotherms.[76]

There are many calculation models depending on the pore size region or adsorbate – adsorbent interaction. Type I isotherms (Langmuir isotherms) are concave to the p/p_o axis and the amount of adsorbate approaches a limiting value as p/p_o approaches 1 and are classically exhibited by microporous solids having relatively small external surfaces (e.g. activated carbons or molecular sieve zeolites). The limiting uptake of adsorbate is governed by the accessible micropore volume rather than by the internal surface area. The reversible type II isotherm is the normal form of isotherm obtained with a non-porous or macroporous adsorbent and represents unrestricted monolayer-multilayer adsorption. The reversible III isotherm is convex to the p/p_0 axis over its entire range and is not common, but can be seen in a number of systems (e.g. nitrogen on polyethylene). The main characteristic feature of a type IV isotherm is the hysteresis loop, which is associated with capillary condensation taking place in mesopores and the limiting uptake over a range of high p/p_0. This shape of isotherm is given typically by mesoporous adsorbents. A type V isotherm is uncommon, but can be obtained with certain porous adsorbents, whilst a type VI isotherm represents a stepwise multilayer adsorption on a uniform non-porous surface, where the step-height represents the monolayer capacity for each adsorbed layer and have

been obtained with argon or krypton on graphitised carbon blacks at liquid nitrogen temperature.

3.3.1 Determination of surface area

3.3.1.1 Brunauer-Emmett-Teller (BET) method[77]

The BET method is the most widely used procedure for the determination of the surface area of solid materials. Two stages are involved in the evaluation of the surface area by the BET method from physisorption isotherm data. First, it is necessary to construct the BET plot and from it to derive the value of the monolayer capacity, n_m. The second step is the calculation of the specific surface area ($a_{(BET)}$) from n_m and this requires a knowledge of the average area occupied by each molecule (σ) in the complete monolayer (e.g. the molecular cross-sectional area). The BET equation can be expressed in the following linear form:

$$\frac{p/p_0}{n\,(1 - p/p_0)} = \frac{1}{n_m \cdot C} + \frac{C - 1}{n_m \cdot C} \cdot (p/p_0) \qquad \textbf{(3.12)}$$

Where n corresponds to the total amount adsorbed and C to the BET constant. This equation is derived from the assumption that the adsorbed molecules in one layer can act as adsorption site for molecules in the next layer. In practice, the BET surface area is calculated from the BET plot of p/p_0 as an x axis and $(p/p_0)/(n \cdot (1-p/p_0))$ as a y axis. The values of the slope and the intercept give n_m. Finally, from the following equation, the BET surface area is obtained.

$$\mathbf{a_{(BET)} = n_m \cdot L \cdot \sigma} \qquad \textbf{(3.13)}$$

Where L is Avogadro constant.

3.3.1.2 *t*-plot method[78]

The *t*-plot method is an alternative method to the BET method, presented by Lippens and de Boer (1965). Here, the experimental isotherm is transformed into a *t*-plot in the

following manner: the amount adsorbed, n, is replotted against *t*, defined as the standard multilayer thickness on the reference non-porous material at the corresponding p/p_0. Any difference in shape between the experimental isotherm and the standard *t*-curve is thus revealed as a non-linear region of the *t*-plot. By this method a specific surface area, denoted as a(*t*), can be calculated from the slope, $s_t = n/t$ of a linear section. The equation of *t*-plot method is written as:

$$\mathbf{a(t) = (M / \rho) \cdot (n / t)} \qquad \mathbf{(3.14)}$$

Where M is molar mass and ρ is mass density.
Taking ρ = 0.809 g cm^{-3} for nitrogen at 77K,

$$\mathbf{a(t) / m^2\ g^{-1} = 0.0346 \cdot (s_t / \mu mol\ nm^{-1})} \qquad \mathbf{(3.15)}$$

In the *t*-plot method, the appropriate standard isotherm must be determined on a non-porous solid having the same surface structure as that of the test adsorbent. The most serious limitation of the *t*-plot method is that it is necessarily dependent on the BET evaluation of the monolayer capacity of the reference material since *t* is derived from n/n_m.

3.3.1.3. α_s method[74]

By a simple modification of the *t*-method it is possible to avoid the prior evaluation of n_m and thereby extend the analysis to virtually any type of physisorption system (Sing, 1968, 1970). To convert the standard adsorption data into an alternative dimensionless form, n_m, is replaced by n_s, the amount adsorbed at a pre-selected arbitrary relative pressure. In practice, it is convenient to take relative pressure of 0.4. The corresponding reduced adsorption is the $n/n_{0.4}$ and is called α_s. The reduced isotherm for the non-porous reference adsorbent is therefore arrived at empirically without any need to determine the BET monolayer capacity. The plot with α_s as an x axis and with n (amount adsorbed) as a y axis is called α_s plot. The α_s method for surface area determination is typically calibrated against certain non-porous reference materials (e.g. aerosil). For example, for nitrogen

adsorption on a non-porous hydroxylated silica at 77K, with a_{ref} = 154 m^2 g^{-1} and $(n_{ref})_{0.4}$ = 2387 µmol g^{-1}, the following equation is obtained:

$$\mathbf{a_{(S\text{-}N2)} / m^2\ g^{-1} = 0.0645 \cdot (s_s / \mu mol\ g^{-1})} \qquad \mathbf{(3.16)}$$

Where s_s can be obtained from the slope of the plot $s_s = n/\alpha_s$,

3.3.2 Assessment of Mesopore Size Distribution

Mesopores are defined as pores with a diameter between 2 and 50 nm.[76] For the determination of pore size and pore size distribution in this pore size region, capillary condensation inside the pores is analysed, which is a typical physicochemical phenomenon in this region. The Kelvin equation describes the relationship between relative pressure (p/p_0) and the radius of a liquid meniscus (r) as:

$$\mathbf{\ln (p/p_0) = -} \frac{2\sigma V_L}{RT}\frac{1}{r_k}\cos\theta \qquad \mathbf{(3.17)}$$

Where, V_L is molar volume of the condensates, σ is surface tension of liquid condensates, and θ is a contact angle (0 in the case of nitrogen).

Before capillary condensation occurs, however, adsorption layer is already formed on the surface of the adsorbent. Therefore, the true mesopore diameter r_p is described as:

$$\mathbf{r_p = r_k + \mathit{t}} \qquad \mathbf{(3.18)}$$

Where t is thickness of the adsorption layer and can be calculated through the equation:

$$\mathbf{\mathit{t} = (v/v_m)\ \sigma} \qquad \mathbf{(3.19)}$$

Where v/v_m is the average number of adsorption layers.

This equation, however, is not suitable when the pore size is wider than 5 nm as pointed out by Barret, Joyner and Halenda (BJH).[79] In this pore size region, the volume of liquid desorbed includes not only the condensate from the next larger size pores but also the volume from a second thinning of the physically adsorbed layer left behind in the pores of the largest size. They provided an alternative calculation method, where pore size distribution is determined by nitrogen desorption branch instead of a combination of adsorption layer (physisorption region) and capillary condensation (BJH method) assuming cylindrical pores. Thus, pore volume at the desorption point n can be described as;

$$V_{pn} = \left(\frac{r_{pn}}{r_{Kn} + \Delta t_n / 2} \right)^2 \left(\Delta V_n - \Delta t_n \sum_{j=1}^{n-1} Ac_j \right) \qquad \textbf{(3.20)}$$

Where r_{pn} is the pore size including physically adsorbed layers, r_{Kn} is the inner capillary radius, t_n is a thickness of physically adsorbed layers, V_n is the desorbed gas volume, and Ac_j is the area exposed by the previously emptied pores. The BJH method offers a means of computing $\sum Ac_j$ from A_p ($A_p = 2V_p/r_p$ for cylindrical pores) for a relative pressure decrement and thus allows the calculation of pore size distribution.

3.3.3 Assessment of Micropore Size Distribution

Micropores are defined as pores with a diameter less than 2 nm.[76] The adsorption process in a micropore is considered different from that in mesopore or macropore regions, where capillary condensation or multilayer adsorption occurs. This is due to the increase in adsorption energy which is derived from the overlapping of the potential fields of adsorptive molecules, whose diameter is close to the pore diameter. There are several methods to determine micropore distribution such as the *t*-plot, α_s, Dubinin-Radushkevich[80], Dubinin-Stoeckli[81] Horvath-Kawazoe[82] or Saito and Foley[83] methods. Recently, computational science has enabled more precise assessment of micropore size distribution (e.g. density functional theory, Monte-Carlo simulation) by describing sorption and phase behaviour of fluids in narrow pores in more detail.

3.3.4 Density Functional Theory (DFT) for Determination of Pore Chracteristics[75]

Classical macroscopic theories like the Dubinin-Radushkevich approach, the BJH method, and semiempirical approach such those of Horvath-Kawazoe and Saito and Foley are said not to give a realistic description of the filling of micropores and even narrow mesopores. This leads to an underestimation of the pore sizes. In order to achieve a more realistic description, microscopic theories are necessary, which describe the sorption and the phase behaviour of fluids in narrow pores on a molecular level. DFT or methods of molecular simulation (e.g. Monte Carlo simulation) provide a much more accurate approach for pore size analysis, bridging the gap between the molecular level and macroscopic approaches. The Non-Local Density Functional Theory (NLDFT) correctly describes the local fluid structure near curved solid walls; adsorption isotherms in model pores are determined based on the intermolecular potentials of the fluid-fluid and solid-fluid interactions. The relation between isotherms determined by these microscopic approaches and the experimental isotherm on a porous solid can be interpreted in terms of a Generalised Adsorption Isotherm (GAI) equation:

$$N(p/p_0) = \int_{W\,\min}^{W\,\max} N(p/p_0, W) f(W) dW \qquad \textbf{(3.21)}$$

Where:

$N(p/p_0)$: experimental adsorption isotherm data

W: pore width

$N(p/p_0, W)$: isotherm on a single pore of width W

f(W): pore size distribution function.

The GAI equation reflects the assumption that the total isotherm consists of a number of individual "single pore" isotherms multiplied by their relative distribution, f(W), over a range of pore sizes. The set of $N(p/p_0, W)$ isotherms for a given system can be obtained, as indicated above, either by DFT or Monte Carlo computer simulation. The pore size distribution is then derived by solving the GAI equation numerically via a specific mathematical algorithm.

3.3.5. Quenched Solid Density Functional Theory (QSDFT) method[84,85]

While NLDFT has proven to be a reliable method for the characterisation of ordered siliceous materials and zeolites or carbon materials with homogeneous surfaces (e.g. carbon material with a graphitic surface), pore size analysis of carbons with heterogeneous surfaces and disordered pore structure remains difficult. The QSDFT method invented by Neimark *et al.* enables the calculation of pore size distributions from 0.5 nm up to *ca*. 40 nm for geometrically and chemically disordered micro-mesoporous carbons.

The main idea here is to use a multi-component DFT, in which the solid is treated as one of the components with a fixed spatially distributed density. The solid is modelled using the distribution of solid atoms rather than the source of the external potential field. This allows for the effects of heterogeneity due to the surface roughness to be accounted for explicitly, improving the NLDFT models for carbons that assumed flat, structureless, graphitic pore walls. The parameters of the fluid-fluid interactions have been determined so as to reproduce bulk thermodynamics equilibria of nitrogen at 77K. The model of the solid, the extent of pore wall roughness / corrugation and fluid-solid interaction parameters have been determined from the fit of the reference experimental adsorption isotherms on graphitised and non-graphitised carbon blacks.

3.4 Fourier Transform Infrared Spectroscopy (FTIR)[86]

Infrared spectroscopy is a well-established technique and commercial instruments have been available since the 1940s. Direct information about the presence of functional groups is immediately available from an infrared spectrum. The spectrum is a plot of the percentage of the infrared beam that passes through (or absorbed through) the sample versus wavelength (or wavenumber) (Figure 3.9). The positions and relative strength of the absorption peaks gives clues to the structure of the molecule by comparing the spectrum of an unknown material with a reference spectrum.

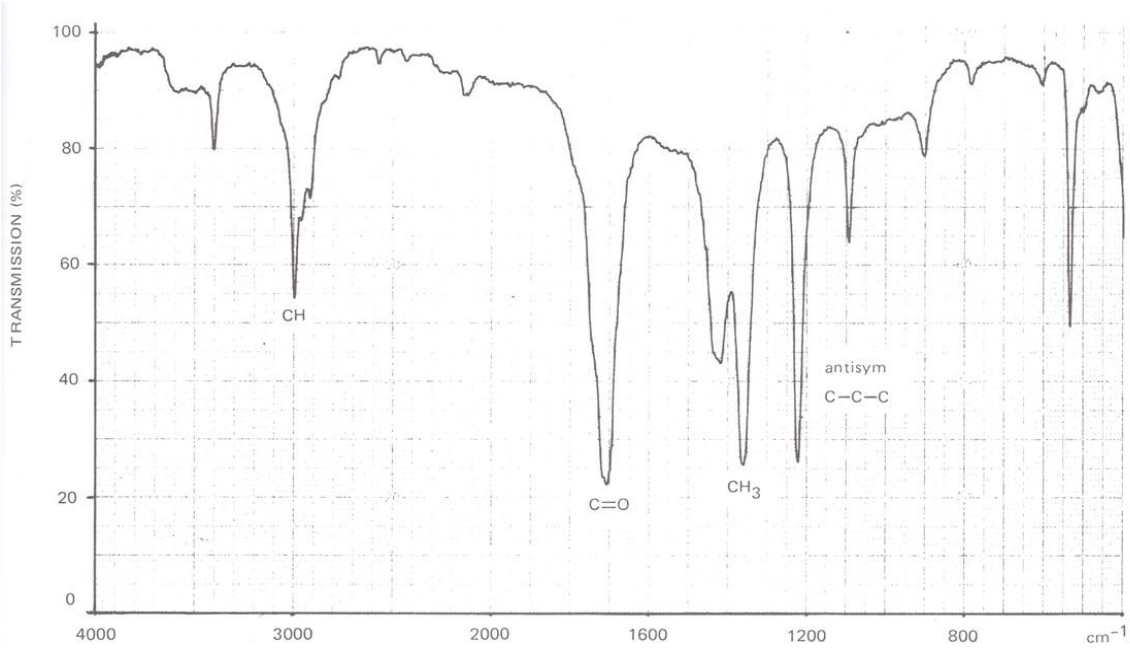

Figure 3.9: An example spectrum of FTIR.

Infrared spectroscopy gives information on molecular structure through the frequencies of the normal modes of vibration of the molecule. A normal mode of vibration is one in which each atom executes a simple harmonic oscillation about its equilibrium position. There are many vibrational modes in one molecule and each vibrational mode is associated with the change in the permanent dipole in the molecule and is therefore IR active (Figure 3.10). A model of the motion of the molecules can be made using balls to represent the atoms and springs to represent the bonds. The motion of the atoms represents the vibration motions through stretching and bending. According to

classical mechanics, the frequency of vibration ν (s^{-1}) of the two connected atoms of mass m (kg) connected by a spring with force constant k (N m^{-1}) is given by:

$$\nu = \frac{1}{\pi} \cdot \sqrt{\frac{k}{2m}} \qquad \textbf{(3.22)}$$

The results of this calculation form the basis for the interpretation of vibrational spectra.

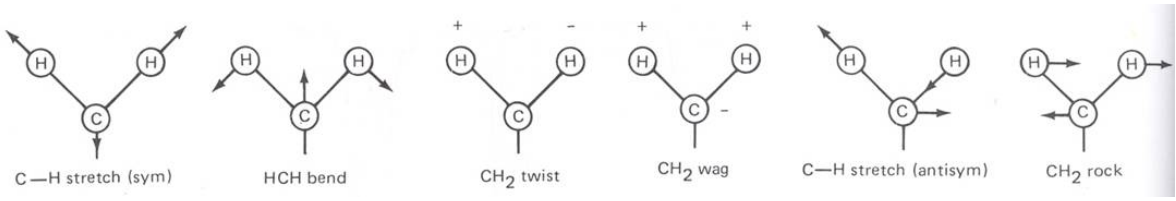

Figure 3.10: A model of vibrational modes of a molecule.

In infrared absorption, energy is transferred from the incident radiation to the molecule and a quantum mechanical transition occurs between two vibrational energy levels. The difference in energy between the two vibrational energy levels is directly related to the frequency (s^{-1}) of the electromagnetic radiation by equation:

$$\mathbf{E_2 - E_1 = h\nu} \qquad \textbf{(3.23)}$$

Where h is Planck's constant ($6.63 \cdot 10^{-34}$ J s) and hν is known as a photon.

A frequency is unique to each molecule or each chemical bond and, thus, by observing the frequency absorbed, we are able to identify molecules and chemical bonds. Particularly, when an FTIR spectrum is recorded, ν (s^{-1}) is a very large number and is inconvenient. Therefore, a more convenient unit $\bar{\nu}$ is obtained by;

$$\bar{\nu} = \mathbf{\nu / c} \qquad \textbf{(3.24)}$$

Where c is the velocity of the light and $\bar{\nu}$ is called wavenumber.

The intensity of an infrared absorption peak is measured using such units as transmittance (%) or absorbance (A) shown below;

$$\textbf{Transmittance (\%): } T = 100 \cdot (I / I_0) \qquad (3.25)$$

$$\textbf{Absorbance (A): } A = \log_{10} (I / I_0) \qquad (3.26)$$

Most FTIR spectrometers are based on the Michelson interferometer, composed of two plane mirrors, M1 and M2 mounted at 90 ^{o} to each other and a semireflecting beam splitter (Figure 3.11). One of the mirrors (M1) is fixed; the other (M2) can be moved very precisely through a distance (δ) of a few millimetres. The beam splitter transmits 50 % of the incident radiation to one mirror and reflects 50 % to the other. After reflection at M1, 50 % of the radiation travels back through the beam splitter and recombines with 50 % of the radiation returned from the mirror M2 and reflected by the beam splitter. The optical path difference between the beams is known as the retardation x (x = 2 δ). Unless x = 0, the recombined beams will interfere. With this arrangement 50 % of the radiation returns to the source. The other 50 % passes through the sample to a detector.

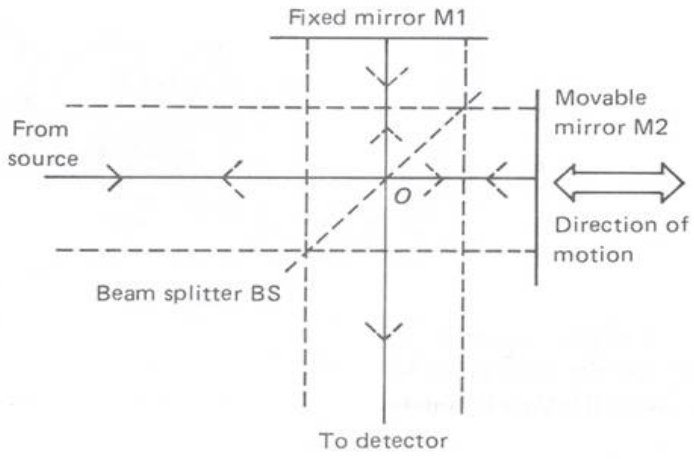

Figure 3.11: A scheme of Michelson interferometer.

In the case of monochromatic beam with the wavelength of λ, the intensity at the detector will be maximum when x = 0, nλ (n = 0, 1, 2, …) and no intensity will be observed when x = λ/2. If the mirror moves constantly, the intensity moves according to a cosine function:

$$\mathbf{I(x) = 0.5 \cdot I \cdot \bar{\nu} \cdot (\cos 2\pi \bar{\nu} x)} \qquad \mathbf{(3.27)}$$

In practice, a continuous source (infinite number of wavelength) of infrared radiation is used. In this case, all wavelengths will be in phase, only when x = 0. At any other position of the mirror, very complex interference pattern will result. A sample placed between the interferometer and the detector reduces the intensity of radiation at any frequency at which the sample absorbs. Thus the infrared absorption spectrum is contained in the resulting interferogram with the horizontal axis of x and the vertical axis of I(x). This interferogram, however, is not convenient to obtain quantitative information about the absorption at each wavelength. Therefore, Fourier transformation must be performed on the interferogram. The obtained spectrum is the FTIR spectrum with the horizontal axis of $\bar{\nu}$ and the vertical axis of I($\bar{\nu}$).

4. Hydrothermal Carbonisation of Carbohydrates in the presence of Inorganic Sacrificial Templates

4.1. Introduction

In this chapter, the use of hard templating will be demonstrated in combination with the hydrothermal carbonisation procedure for the synthesis of nanostructured carbon materials. A variety of inorganic templates, such as mesoporous silica beads, meso - macroporous bimodal silica monolith and macroporous alumina membranes are utilised. The use of the hydrothermal carbonisation process is very advantageous in this context as it allows relatively facile impregnation / infiltration of water-soluble carbon precursors (e.g. carbohydrates) due to its aqueous reaction process. Furthermore, the surface chemistry of the resulting replicas possess functionality suitable for relatively facile post-chemical modification, whilst importantly, materials surface character can also be effectively tuned by selection of post-hydrothermal carbonisation temperature allowing further subtle control of surface / bulk chemistry from more polar hydrophilic (e.g. OH, COOH, and C=O functionalities) to increasingly non-polar / hydrophobic structural motifs (e.g. extension of the aromatic / pseudo-graphitic nature), thus allowing simultaneous control of materials nanostructures and surface properties.

With regard to chromatographic applications, mesoporous silica beads are considered to be the classical standard separation media while silica monoliths are considered to be the new generation of stationary phases.[87,88,89,90] Chromatographic silica beads are monodisperse spherical micrometer-sized (e.g. 5 - 10 μm) particles presenting a pore size typically in the range of 5-30 nm, whilst silica monoliths represent a single

continuous piece of hierarchically structured macro- and mesopores. As a consequence of such continuous pore structuring, monoliths are considered superior to conventional bead-based separation media, specifically in terms of mass transfer and diffusion kinetics. Both types of silica material have been successfully replicated via hard templating / nanocasting approaches into the corresponding carbon replica materials with bimodal or multipore size distributions.[91, 92, 93] However, one drawback of these established approaches is the use of high pyrolysis temperatures (e.g. > 1000 ^{o}C) used to carbonise the impregnated precursors and render material stable enough to withstand the chemical abrasiveness of the template removal step. Therefore the surfaces of such replicas are essentially chemically inert, making another post-chemical modification a significant synthetic challenge.[8, 94] Furthermore, such methods are also limited in terms of "sustainability" due to the resource consumptive high temperature synthesises and petroleum-derived precursors employed. Thus, while such hard templating strategies can be considered powerful tools in terms of nanostructure replication, novel approaches allowing synthesis of functional carbon nanostructures under mild condition are of significant interest and desirability.

Through the similar templating techniques, tubular carbonaceous nanostructures have been obtained using uniform and straight macropore channels offered by anodic alumina membrane (AAO).[95,96,97,98,99,100] Although their chemistry are typically very different to that of carbon nanotubes,[17, 101, 102, 103] they are finding use in similar application fields (e.g. sensing,[104,105] photonic crystals,[106] catalyst supports,[107,108] and energy storage[109,110]) due in part to similarities in morphology; i.e. tubular structures but with larger diameter in the upper nm-range (e.g. ~ 100 nm). The templating of AAO to produce tubular carbon materials was first reported by Martin *et al.* who demonstrated the production of metal and polymer microtubles.[111,112] Later on, Steinhart and Wendorff introduced a liquid phase approach to synthesise carbon, polymer and metallic hollow nanotubes.[113,114] This method involves the initial physical wetting of the AAO with the corresponding precursor to form a thin liquid film covering the substrate. After condensation of precursor towards the desired material, the template is removed by acid etching leading to carbon, polymer or metallic nanotubes, where tube diameter can be controlled by template pore size, while tube wall thickness corresponds to the amount of wetted monomer introduced. This method has since been extended to the production of 1-D tubular carbon structures from a variety of carbon precursors either by gas[95,97] or

liquid[99] infiltration techniques, with subsequent application of the reported materials in a variety of topical fields including catalysis and electrochemistry.[97,98,107,115] Here again, high-temperature carbonisation is employed rendering materials relatively chemically inert. Therefore, a combined hydrothermal carbonisation – templating approach would be of great value if it could allow a direct synthesis of functional carbonaceous tubular nanostructures.

In sub-chapter 4.2, nanocasting replication of silica templates (e.g. beads and monoliths) will be presented, whilst in chapter 4.3, the use of a macroporous alumina membrane template for the production of tubular carbon nanostructures, demonstrating throughout the applicability of the combined hydrothermal carbonisation / hard templating route to the production of tuneable carbon nanostructures. Additionally, by taking advantage of modifiable oxygen containing surface groups afforded by the hydrothermal carbonisation approach, the introduction of useful polymeric moieties by grafting of a thermoresponsive polymer (e.g. poly(N-isopropylacrylamide (PNiPAAM)) will be also demonstrated.

4.2. Silica as a Sacrificial Template

4.2.1. Hard-Templating of Mesoporous Silica Beads for the Production of Hydrothermal Carbon Spheres

4.2.1.1 Chemicals

Silica beads Si 300 (φ 30 nm) were kindly provided by Merck®. 2-furaldehyde and NH_4HF_2 was purchased from Sigma-Aldrich (Steinheim, Germany) and used as received.

4.2.1.2 Synthesis method for hard-templating of mesoporous silica beads

A 50 wt% 2-fualdehyde – H_2O mixture (2-furaldehyde 2.0 g : water 2.0 g) was infiltrated into mesoporous silica beads Si-300 and heat treated in a stainless steel autoclave (Paar, Acid Digestion Vessel 4744) at 180 ^oC for 48 h. The recovered product was washed extensively with water and dried in a vacuum oven overnight at 70 ^oC. The dried silica - hydrothermal carbon composite was then either directly washed with 4M NH_4HF_2 (aq) or further carbonised under an inert atmosphere (i.e. N_2) for 3 h at the desired temperature (i.e. 350 ^oC, 550 ^oC, and 750 ^oC). Calcined materials were also washed with a 4M NH_4HF_2 (aq) at room temperature to remove the silica template. The resulting carbon replicas were carefully washed with H_2O and dried overnight under vacuum at 70 ^oC.

4.2.1.3 Results and Discussion

Previously, our group has reported that for a successful replication, it is important to match the template surface polarity with that of the carbon precursor.[116] Hydrophobisation of the silica template can be performed via methylation or thermal treatment (Scheme 4.1). A variety of morphologies are obtained using silica templates with different polarities and 2-furaldehyde as a carbon source (Figure 4.1). The use of silica templates with a very hydrophobic surface character leads to the generation of macroporous carbon casts (Figure 4.1.a) whereas hollow carbon spheres are produced when using a moderately hydrophobic surface (Figure 4.1.b).

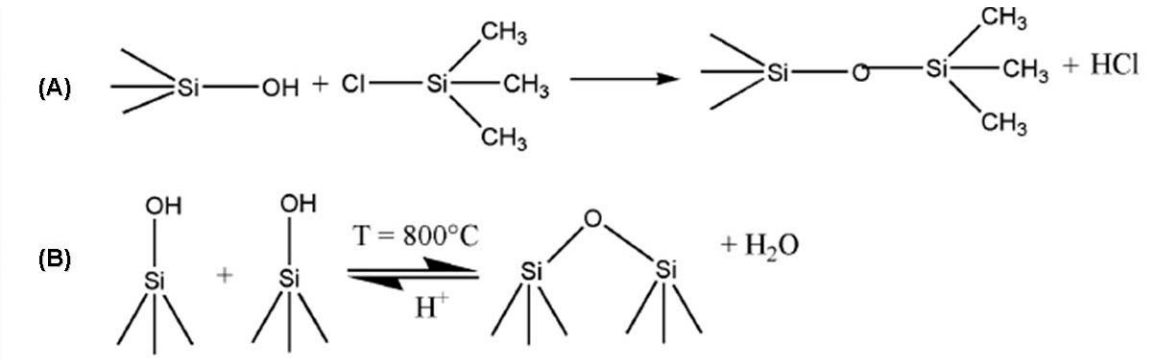

Scheme 4.1: (A) hydrophobisation of the rehydroxylated silica with trimethylchlorosilane and (B) dehydroxylation of silica surface by condensation at 800 ^{o}C. Adapted from the reference.[116]

Here, surface hydrophobicity of the silica template was considered too high for the carbon precursor to achieve complete penetration under hydrothermal conditions. Dehydroxylated silica templates filled with 60 wt% 2-furaldehyde resulted in mesoporous carbonaceous microspheres (Scheme 4.1.b; Figure 4.1.d) thus demonstrating successful templating, whereas application of a 30 wt% carbon precursor gave only small carbon spherules (6 – 10 nm diameter), owing to the lack of interconnectivity between growing particles in the coating. Furthermore, when rehydroxylated silica was used, demixing occurred due to the enhanced hydrophilic character of the template surface essentially inhibiting impregnation of the 2-furaldehyde (data not shown). Complete impregnation was achieved by controlling the degree of hydrophobicity of the template and by controlling the concentration of the carbon precursor in an aqueous solution. In addition to the matching of the surface polarities, it was also illustrated that the carbon nanocoating procedure operates in a "patchwise" manner, via the generation of stable colloidal intermediates. For nonporous templates, hollow carbonaceous spheres with a robust carbon coating are observed (Figure 4.1.c).

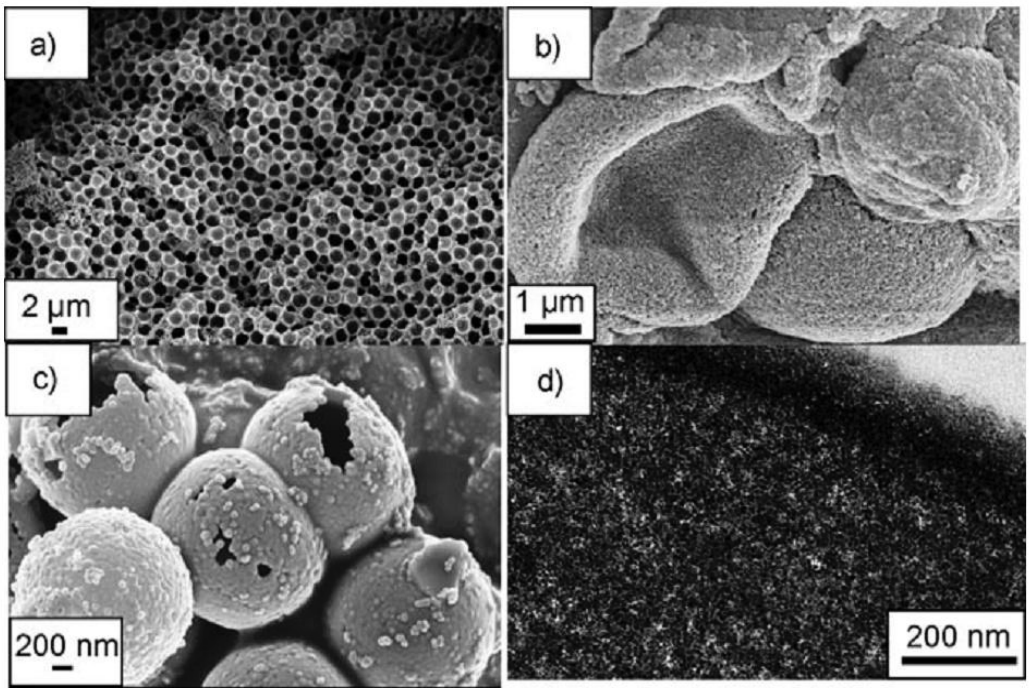

Figure 4.1: Morphologies obtained via hydrothermal carbonisation of glucose in the presence of silica templates with different polarities. a) Macroporous carbon cast obtained in the presence of nonporous silica with a very hydrophobic surface, b) mesoporous-shell hollow spheres obtained from mesoporous silica templates with moderate hydrophobicity, c) hollow spheres obtained using nonporous silica spheres with moderate hydrophobicity, and d) mesoporous hydrothermal carbon replica obtained using a calcined mesoporous silica template. Adapted from the reference.[116]

Likewise, in the case of employing a dehydroxylated Si-300 silica bead template (Figure 4.2, BET surface area (S_{BET}) = 58.3 m^2g^{-1}, total pore volume (V_{total}) = 0.25 cm^3g^{-1}, micropore volume (V_{micro}) = 0 cm^3g^{-1}), spherically shaped carbonaceous particles were successfully synthesised. Comparison with an SEM image of Si-300 silica template reveals that the particle size (~ 5 µm) and the morphology uniformity were both maintained (Figure 4.3.a and b). Post-carbonisation treatment had no significant impact on the material morphology (Figure 4.3.c and d). From elemental analysis, carbon content of the synthesised materials was observed to increase from 64 wt% to 81 wt% for the post-carbonised materials (750 ^oC), thus showing increased carbon-rich character.

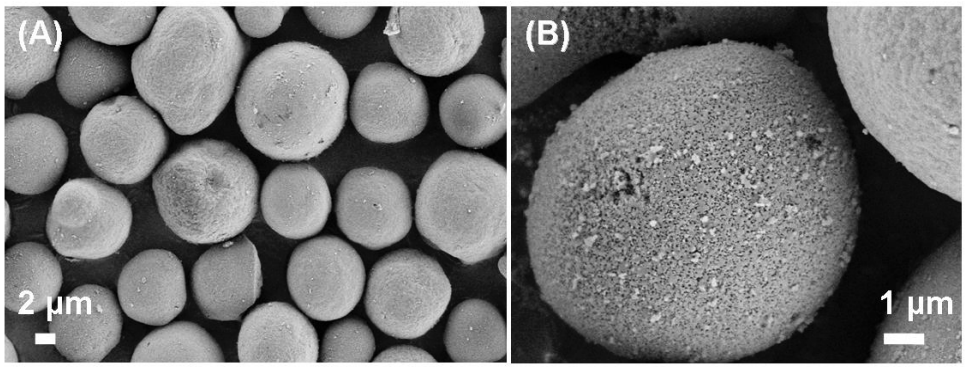

Figure 4.2: (a) and (b) SEM micrograph of Si-300 silica beads.

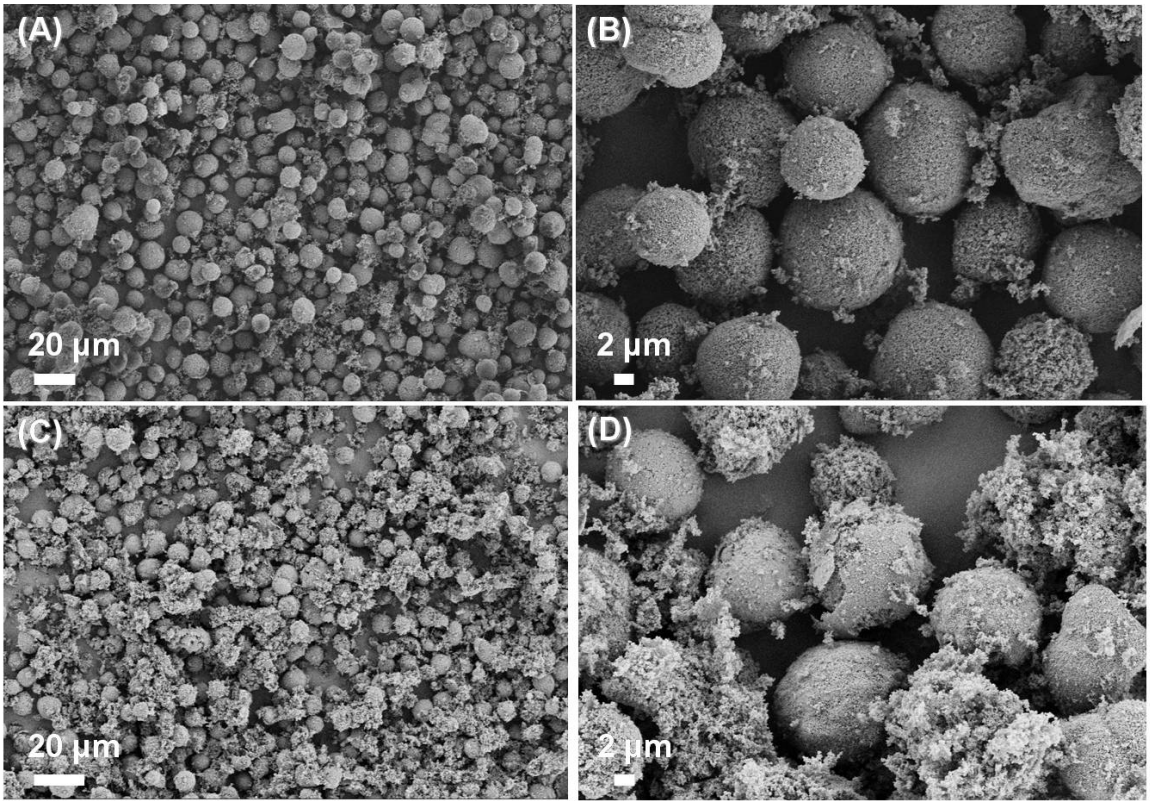

Figure 4.3: SEM micrographs of (a) and (b) a synthesised carbon replica (HTC@180°C) and (c) and (d) a carbon replica after post-calcination at 750 ^{o}C.

TGA curves (performed under an oxygen atmosphere) showed different mass loss features between the as-synthesised replicas and the replica carbonised at 750 ^{o}C (Figure 4.4). The *d*TG curve of the as-synthesised replica shows a very small peak at the temperature < 100 ^{o}C which is due to the removal of physisorbed water (Figure 4.4.a). Two main peaks at ~ 310 ^{o}C and ~ 480 ^{o}C correspond to desorption of structural chemisorbed H_2O and CO_2, and the latter to oxidative corrosion of the carbonaceous framework.

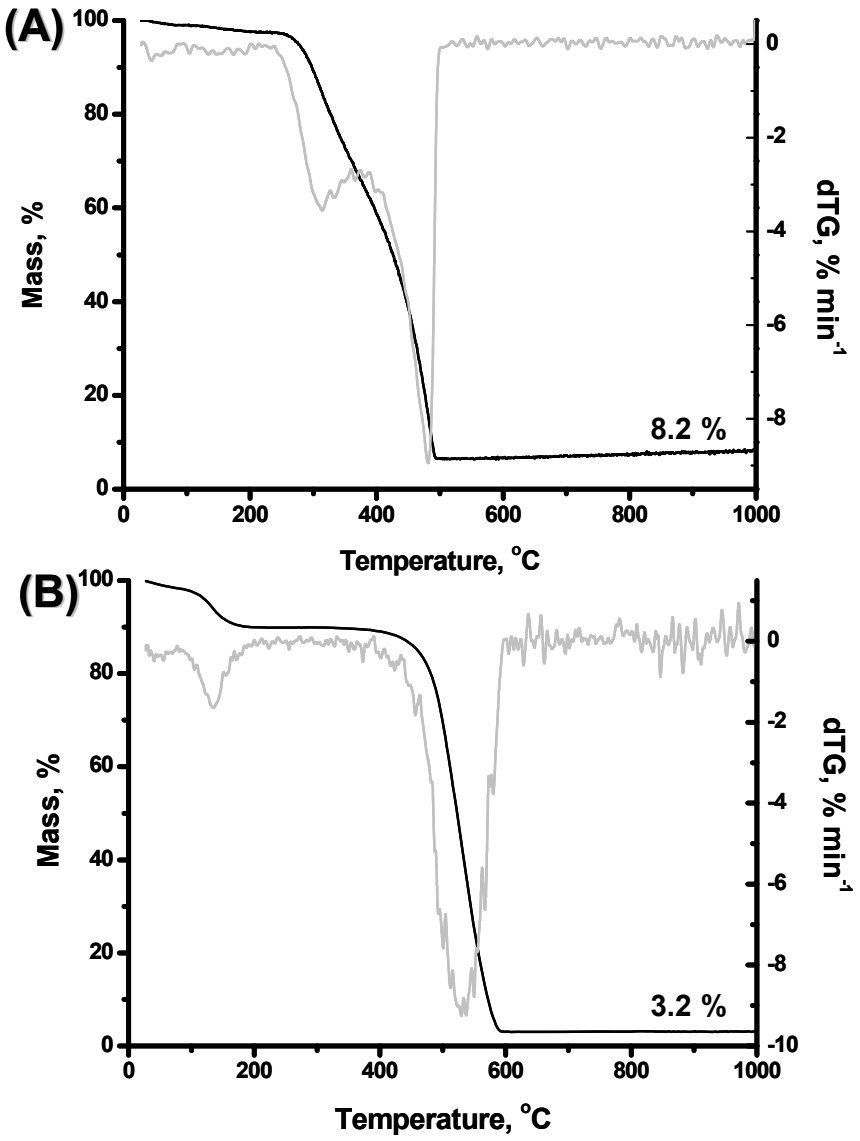

Figure 4.4: TGA (black line) and *d*TG (grey line) curves for (a) as-synthesised replica and (b) replica post-carbonised at 750 °C (performed under an oxygen atmosphere).

The *d*TG profile of the post-carbonised replica demonstrates much higher oxidation stability as demonstrated by a shift in the peak corresponding to the oxidative event to ~ 530 °C. This is indicative of the increasing content of aromatic species in the carbon structure by employing the post-carbonisation step and correlates well with the result obtained from the elemental analysis. The obtained TGA curves also confirm the near complete removal of the inorganic template (Residual mass loss ~ 8 % for the as-synthesised replica and ~ 3 % for the replica carbonised at 750 °C).

The main advantage of the combined hydrothermal carbonisation / hard templating method is the accessibility of materials possessing surface functionalities. By

further post-carbonisation treatment of the obtained composite at different temperatures (i.e. 350, 550, 750 ^{o}C) followed by the template removal, carbon spheres with different pore properties and surface functionalities were obtained.

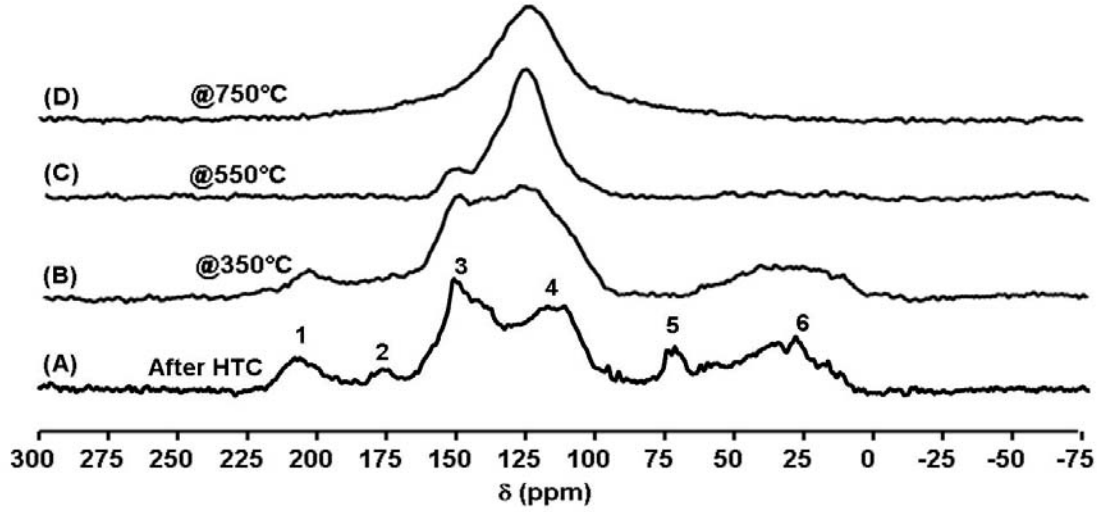

Figure 4.5: ^{13}C CP MAS solid state NMR spectrum of (a) the synthesised carbon replica (b) the replica carbonised at 350 ^{o}C, (c) at 550 ^{o}C and (d) at 750 ^{o}C.

Table 4.1: Peak assignment of the ^{13}C CP MAS spectra.

Peak number	Peak position, ppm	Assignment
1	200 - 220	C=O
2	175	C(O)OH
3	140 - 160	O-C=C
4	100 - 150	C=C
5	75	C-O-C
6	0 - 75	C-C

^{13}C CP MAS solid-state NMR spectrum of the produced carbon material shows three main functional group types: aliphatic groups (δ = 0 - 75 ppm), which connect the polar functional groups; aromatic groups (δ = 100 - 160 ppm) containing C=C and O-C=C double bonds from the poly-furan hydrothermal carbon structure; and functional groups such as C-O-C (at δ = 75 ppm), C=O (δ = 200 ppm) and COOH (δ = 175 ppm), respectively (Figure 4.5, peak assignment is summarised in Table 4.1.).[31] After further carbonisation under N_2 at 350 ^{o}C, the C=O functional group was still observed showing still the existence of oxygenated surface functionality, whilst C(O)OH and C-O-C

funtionalities disappeared. Further carbonisation under N_2 at 550 ^oC and above led to increasingly extended aromatic system comprising C=C sp^2-conjugated double bonds indicated by the developing intense peak centred at δ = 129 ppm. It is clear from the spectra that all the functional groups present on the carbon surface have disappeared after the post carbonisation at 750 ^oC generating a more hydrophobic and homogeneous surface character. This result is complementary to the previous EA and TGA results, which showed increased carbon character and oxidation stability as a result of increased aromatic / pseudo-graphitic character.

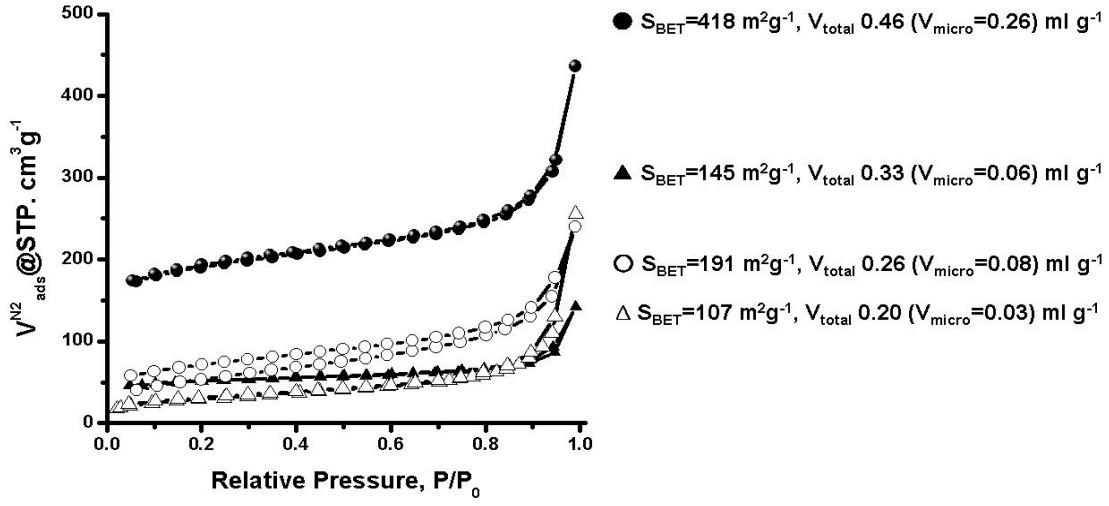

Figure 4.6: N_2 sorption isotherms of (a) Si-300 silica bead template and (b) (open triangle) an as-synthesised carbon replica (closed triangle), and replica carbonised at 350 ^oC, (open circle) at 550 ^oC and (closed circle) at 750 ^oC.

In unison with the change in the surface properties, difference in pore properties was also observed between the four different types of materials. Both surface area and pore volume increased with the increase in post carbonisation temperature, from 107 to 418 m^2g^{-1} and from 0.20 to 0.46 $cm^3\ g^{-1}$ (Figure 4.6). Significantly, the as-synthesised materials micropore volume increases dramatically with increasingly higher carbonisation temperature (e.g. 750 ^oC) contributing to the observed increase in material total pore volume, which is believed to the consequence of carbon network decomposition and the evolution of strongly adsorbed non-incorporated hydrothermal carbonisation products (e.g. oligo-furans or levulinic acid) during the heat treatment.[117]

In this way, the morphological structure of mesoporous silica beads was successfully templated to yield the spherical carbonaceous replica. As examined by EA, TGA and NMR analyses, control of surface properties and the aromatic / condensed nature of the carbonaceous replica could be achieved (from hydrophilic, functional groups rich property to more hydrophobic, aromatic, carbon-rich property), whilst spherical morphology was maintained throughout the whole series of materials post-carbonisation at different temperatures.

4.2.2 Hydrothermal Carbon Monoliths

4.2.2.1 Chemicals

Bimodal silica monoliths were obtained from Merck®. 2-furaldehyde and NH_4HF_2 were purchased from Sigma-Aldrich (Steinheim, Germany) and used without further purification.

4.2.2.2 Synthesis of replica of silica monoliths

In a typical synthesis, 0.1 g of silica monolith was infiltrated with a solution mixture of 4.0 g of 2-furaldehyle and 10.0 g of water and hydrothermally treated at 180 ^{o}C in an autoclave for 48 h. The drying and template removal procedure was the same as described in the chapter 4.2.1.2.

4.2.2.3 Results and Discussion

The silica monolith used as a sacrificial template in this study shows a single continuous piece; possessing 1 - 2 μm sized continuous macropores (Figure 4.7.a, 4.8.a and b). N_2 sorption indicates a type IV isotherm with a specific surface area of 350 m^2g^{-1}, total pore volume of 0.96 cm^3g^{-1} and pore diameter of 16 nm (Figure 4.9). Thus, material possesses mesopores in the macroporous silica wall representing a meso- and macro- bimodal pore structuring.

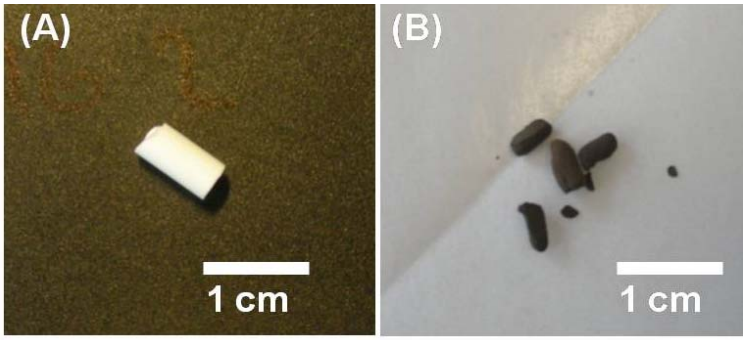

Figure 4.7: Optical micrographs of (a) template silica monolith and (b) synthesised carbon materials after template removal.

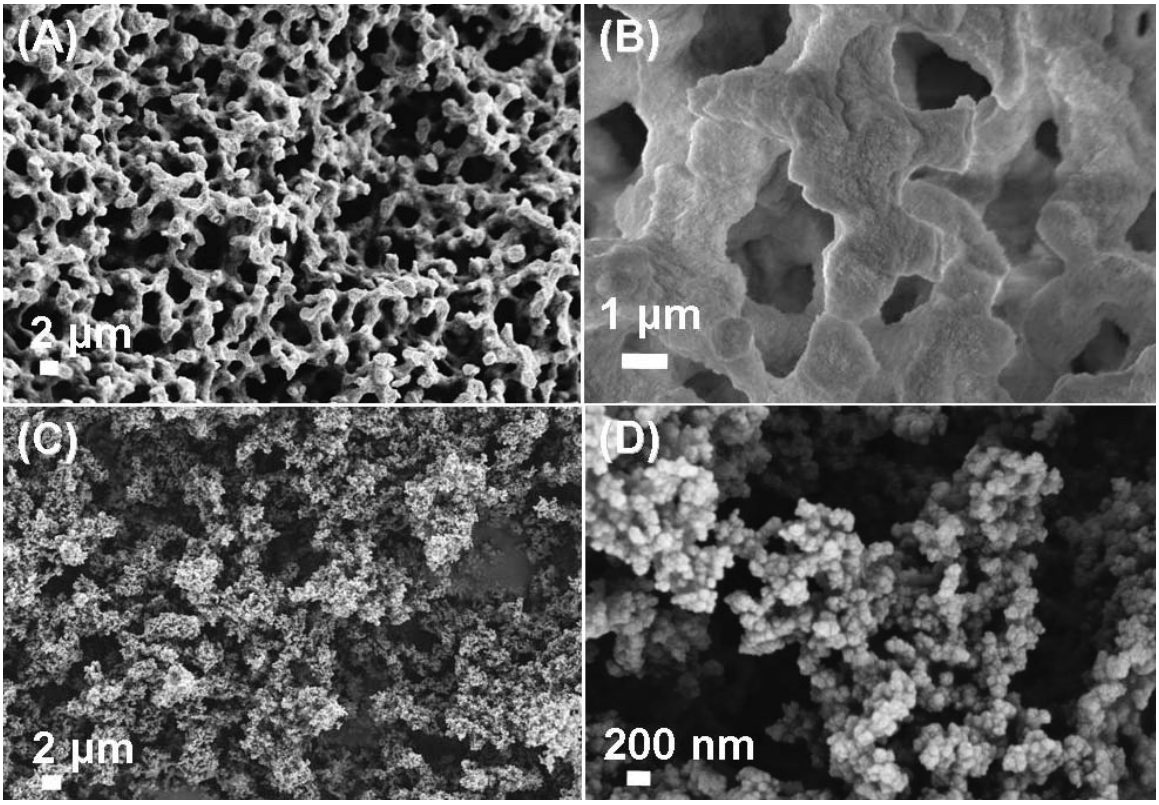

Figure 4.8: SEM micrographs of (a) and (b) a template silica monolith and (c) and (d) synthesised carbon material after template removal.

Unfortunately, the monolithic morphology could not be completely maintained after nanocasting (Figure 4.7.b). The SEM micrograph shows *ca.* 2 µm - sized aggregates (Figure 4.8.c), each of which is composed of uniform small spherical particles with a size of 0.1 µm (Figure 4.8.d) and, interestingly, approximately the same in size (~ 2 µm) as the macropore of the template and thus is considered a reverse structure of the macropores. However, a mechanically strong, continuous aggregated phase could not be produced via this approach leading to a lack of stable monolithic morphology.

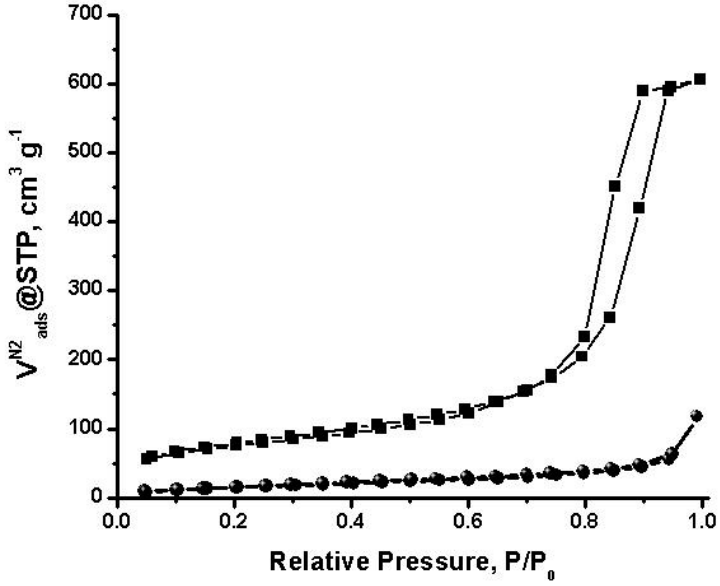

Figure 4.9: N_2 sorption isotherms of (closed square) an original silica monolith template and (closed circle) a templated carbonaceous material.

The specific surface area of the replica decreased considerably from the 350 $m^2 g^{-1}$ characterised in the original silica monolith to the lower value of 70 $m^2 g^{-1}$ in the final carbonaceous material, in unison with a marked reduction in material mesopore content; from 0.96 cm^3g^{-1} to 0.30 cm^3g^{-1}(Figure 4.9). Mesoporosity in the case of the replica is presumably the results of interstitial voids between aggregated particles and not the comparatively well ordered mesoporosity observed in the template. We believe this problem occurs either because the 2-furaldehyde carbon precursor was not properly infiltrated into mesopores of the template or the generated hydrothermal carbon network was not rigid enough to maintain such a complex hierarchical arrangement of the meso-macropores under the synthesis conditions employed. Regarding mesopore impregnation, the precursors generally tend to be absorbed at the external surface of the templates and the mesopore channels are fairly difficult to fill completely due to capillary effects.[68] This can be also considered to have hindered the maintenance of monolithic morphology due to the lack of the bridges between macroporous domains. Therefore, improved infiltration and achieving increasingly rigid carbon networks (e.g. highly cross linked or highly condensed carbon networks) is desirable for the successful templating. For this, vacuum infiltration techniques[118] or an additional cross linking / carbonisation step (e.g. cross linking of the formed poly-furan network) would possibly be helpful in successfully replicating the template structure and morphology.

4.3 Macroporous Alumina Membranes as a Sacrificial Template

4.3.1 Chemicals

Alumina membranes with an average pore diameter of 200 nm (Anodisc 13) were purchased from Whatman International (Maidstone, England). 2-furaldehyde (furfural) was purchased from Sigma-Aldrich (Steinheim, Germany). (3-Aminopropyl) triethoxysilane (APS) was obtained from Fluka. N-isopropylacrylamide (NiPAAm) and 2,2-azobisisobutyronitrile (AIBN) were purchased from Acros and were recrystallized from n-hexane and methanol respectively. The RAFT agent (4-cyanopentanoic acid trithiododecane) was synthesized according to the literature.[119] N-hydroxysuccinimide, N,N-dicyclohexylcarbodiimide (DCC) and ethyl acetate were also obtained from Fluka.

4.3.2 Synthesis

4.3.2.1. Synthesis of Carbonaceous Tubular Nanostructures (denoted as tubular carbons)

In a typical synthesis 0.1 g of alumina membrane (Whatman, Anodisc 13) was soaked in a mixture of 1.2 g of 2-furaldehyde and 4.0 of water and subsequently placed into a stainless steal autoclave (Parr, Acid Digestion Vessel 4744) which was then sealed and placed in a 180 ^{o}C oven for 48 h. The recovered product was washed extensively with water and dried in a vacuum oven overnight at 70 ^{o}C. The dried alumina membrane - hydrothermal carbon composite was then further carbonised under an inert atmosphere (i.e N_2) for 4 h at the desired temperatures (i.e. 350 ^{o}C, 550 ^{o}C, and 750 ^{o}C respectively). To remove the AAO template, a concentrated phosphoric acid washing step was employed, conducted under stirring at 65 ^{o}C. The resulting carbon replicas were then sonicated, carefully washed with water and dried in a vacuum oven overnight at 70 ^{o}C.

For comparison purposes, impregnation of an AAO membrane was also performed without any previous hydrothermal treatment. Here, alumina membrane was soaked into the mixture of 1.2 g of 2-furaldehyde and 4.0 of ethanol and mechanically shaken at room temperature for 48 h, followed by post-carbonization treatment as indicated above. Template removal was conducted in the same way as described above. In this case, however, no solid precipitate was recovered after washing, proving that the hydrothermal treatment has a crucial role in a successful replication.

4.3.2.2 Preparation of Thermoresponsive Tubular Carbons.

(a) Preparation of PNiPAAm in solution by RAFT.

4.0 g (35.0 mmol) of N-isopropylacrylamide (NiPAAm) were dissolved in 6.0 mL of dry DMF. 40.0 mg (0.1 mmol) of 4-cyanopentanoic acid trithiododecane RAFT agent and 2.6 mg (0.024 mmol) of azobisisobutyronitrile (AIBN) initiator were added to this solution. After three freeze-dry cycles, the reaction mixture was heated at 70 ^{o}C for 24 h. PNiPAAM polymer was obtained by precipitation into diethyl ether followed by drying overnight under vacuum at 50 ^{o}C.

(b) Activation of carboxylated PNiPAAm.

4.0 g (0.14 mmol) of carboxylated PNiPAAm was activated with 115 mg (1 mmol) of N-hydroxy succinimide and 206.0 mg (1 mmol) of N,N'-Dicyclohexylcarbodiimide (DCC) in 10 mL ethyl acetate and was stirred at 0 ^{o}C for 2 h followed by stirring overnight at room temperature. The activated polymer solution was filtered and the polymer was isolated by precipitation in diethyl ether followed by a drying step overnight under vacuum at 50 ^{o}C.

(c) Grafting of PNiPAAm onto tubular carbons.

70.0 mg of as synthesized tubular carbons were dispersed in a solution of 0.1 mL (3-aminopropyl) triethoxysilane (APS) dissolved in 10.0 mL dry toluene and refluxed under stirring for 12 h. The amino modified tubular carbons were washed with toluene and methanol, filtered and dried overnight under vacuum at 50 °C. Afterwards, the amino modified tubular carbons were dispersed in 10.0 mL dry 1,4-dioxane containing 150.0 mg of carboxylated PNiPAAm and stirred overnight at room temperature. The resulting PNiPAAm modified carbon composites were washed with dioxane and methanol, followed by filtration and drying overnight under vacuum at 50 ^{o}C.

4.3.3 Results and Discussions

4.3.3.1 Morphology and Chemical Composition

Template AAO possesses uniform macropore channels with a diameter of averagely 200 nm (Figure 4.10). The as-synthesised tubular carbons were denoted as HCT, HCT-350, HCT-550, and HCT-750, where HCT refers to "Hydrothermal Carbonaceous Tubular nanostructures", while the number corresponds to the post-carbonisation temperature. SEM micrographs of these samples show in all cases monodisperse tubular carbons with a length of several micrometers (Figure 4.11.a and b). TEM micrographs reveal that the tubular carbons possess an open ended structure with smooth surfaces (Figure 4.11.c and d).

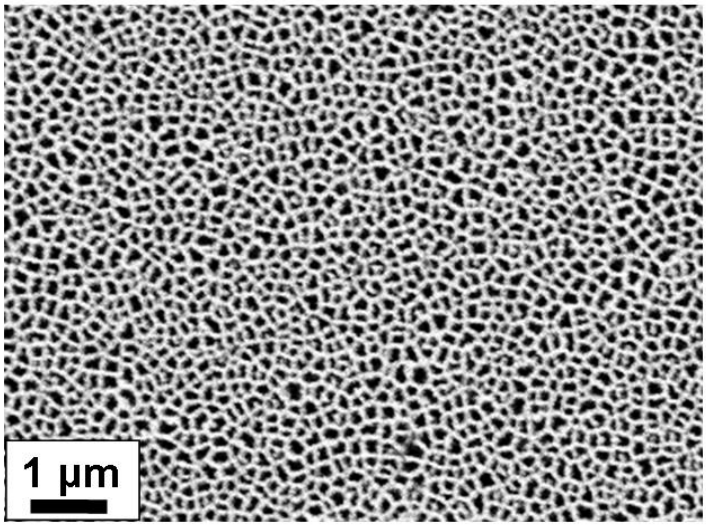

Figure 4.10: SEM micrograph of the AAO template.

Tube diameters are approximately equal to size of AAO macropore domains (*ca*. 200 nm), constituted of a hollow internal diameter of *ca.* 125 (± 25) nm and *ca.* 40 nm thick carbonaceous tube walls. All materials, regardless of post-carbonisation temperature, presented an identical morphology, whilst pore wall thickness was observed to marginally decrease as treatment temperature passed 550 ^{o}C. However, looking carefully at the high resolution TEM micrographs before (Figure 4.11.e) and after further carbonisation (Figure 4.11.f) we can observe that the level of local order is improved with temperature.

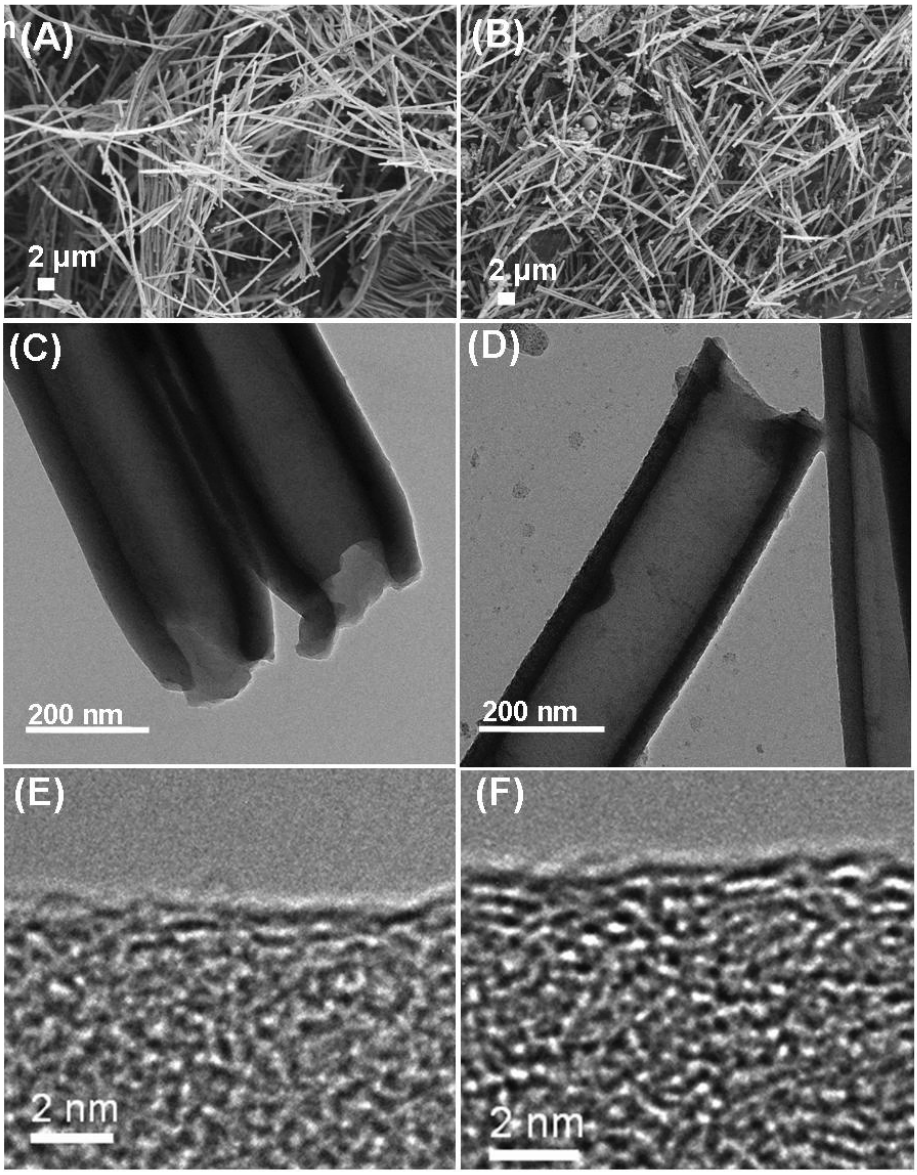

Figure 4.11: SEM micrographs of synthesised tubular carbons (a) HCT and (b) HCT–750; TEM micrographs of (c) HCT and (d) HCT-750; HR-TEM micrographs of (e) HCT and (f) HCT-750.

The successful removal of the alumina template was confirmed using oxidative TGA analysis, indicating a negligible mass residue (e.g. 8.6 wt% for HCT-750; (Figure 4.12)). *d*TG curve analysis indicated two main mass loss regions in the case of the HCT material, with an initial mass loss event centred around ~ 300 °C corresponding to the desorption of structural chemisorbed H_2O and CO_2, while the second peak centred at ~ 440 ^oC is due to oxidative corrosion of the carbonaceous framework.

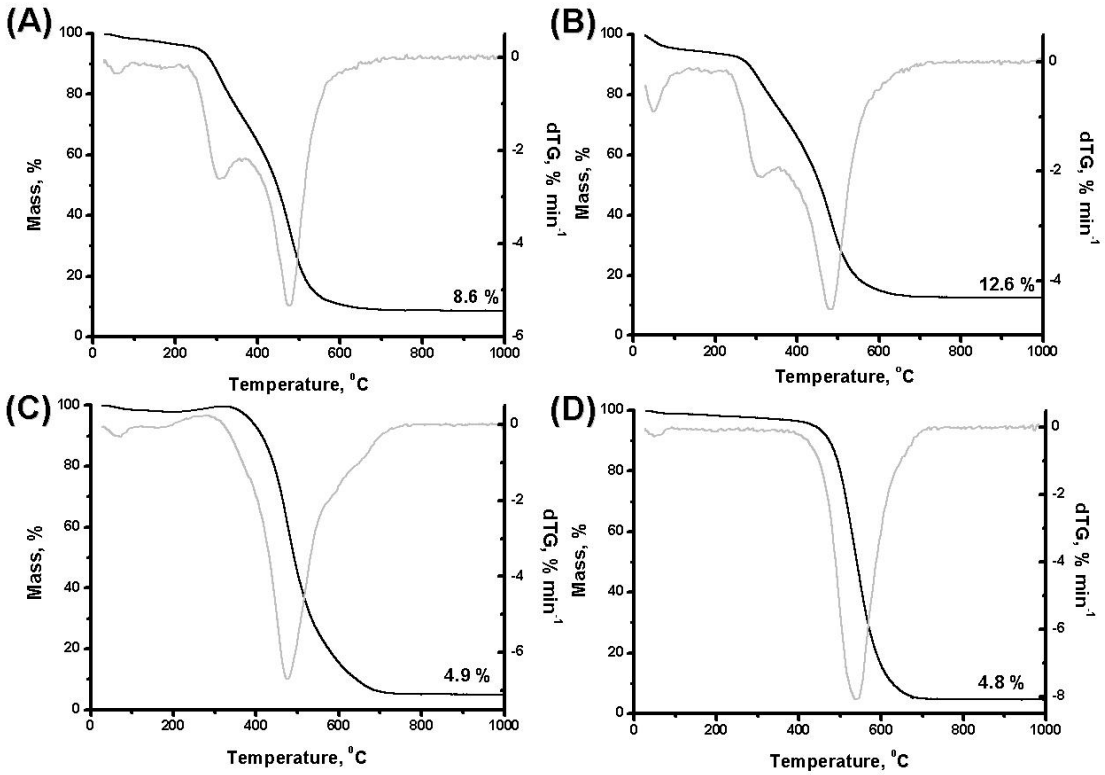

Figure 4.12: TGA (black line) and *d*TG (grey line) curves of (a) HCT (b) HCT-350(c) HCT-550 and (d) HCT-750.

The *d*TG profile of HTC-750 demonstrates much higher oxidation stability as demonstrated by a shift in the peak corresponding to the oxidative event to ~ 550 °C. HCT materials prepared at intermediate carbonization temperatures (i.e. 350 ^{o}C and 550 ^{o}C) are increasingly more oxidation stable indicative of the increasing content of aromatic species in the carbon structure. Elemental analysis nicely complements TG analysis, demonstrating the carbon content increase as a function of post-carbonisation temperature from 62 wt% for HCT to 81 wt% for HCT-750, while correspondingly the hydrogen and oxygen contents are observed to decrease (Table 4.2).

4.3.3.2 Control in Surface Properties

One of the most important advantages of the presented synthetic strategy is the possibility to tune tube surface functionality via selection of the post-carbonisation temperature. To observe changes in the surface chemistry as a function of this preparation parameter, the four synthesised tubular carbon samples were analysed by FTIR (Table 4.2; Figure 4.13).

Table 4.2: Structural and surface properties of the synthesised tubular carbons.

Sample	C / % [1]	O / % [1]	N / % [1]	Surface functional groups [2]	N_2		CO_2	
					S, $m^2 g^{-1}$ [3]	V_{total} (V_{micro}), $cm^3 g^{-1}$ [4]	S, $m^2 g^{-1}$ [3]	V_{total} $cm^3 g^{-1}$ [4]
HCT	62	34	0	-OH, C=O, C-H, C=C, C=C-O	33	0.05 (0)	-	-
HCT-350	63	33	0	-OH, C=O, C-H, C=C, C=C-O	22	0.03 (0)	-	-
HCT-550	73	26	0	C=C, C-H, C-H(out-of-plane)	116	0.14 (0.06)	550	0.16
HCT-750	82	16	0.2	-	699	0.53 (0.12)	674	0.21
HCT-PNiPAAm	61	33	1.5	-OH, C=O, C-H, C=C, C=C-O, -NH	-	-	-	-

1) C, O, N content from elemental analysis, 2) Surface functional groups observed by FTIR, 3) Surface area and 4) total pore volume with micropore volume in parentheses calculated by NLDFT method.

Spectra for HCT and HCT-350 present a broad absorption band between 3700 - 3100 cm^{-1}, corresponding to (H-bonding) –OH stretching modes. Additionally bands in the range of 1800 - 1520 cm^{-1} are assigned to C=O stretching modes from C(O)OH / lactone-type groups revealing that the surfaces of these low carbonisation temperature replicas are decorated with oxygenated functional groups.[120] Spectra for HCT and HCT-350 also indicate the presence of methyl-type groups (e.g. ν(C-H) stretching mode; 2925 cm^{-1}) and conjugated C=C / olefinic species (C=C-O) (e.g. stretching modes between 1650-1450 cm^{-1}). As the carbonisation temperature is increased (e.g. @HCT-550), bands associated with C=O features become increasingly weaker, in unison with a decrease in intensity of –OH bands. Heating to 550 ^{o}C and above results in an increasingly stronger aromatic character as C-H (out-of-plane) bending modes are observed at 877 cm^{-1}, 816 cm^{-1}, and 752 cm^{-1}.[121] For material prepared at 750 ^{o}C, acquisition of suitable spectra was not possible due to the increasingly light absorbing character of the carbon material.

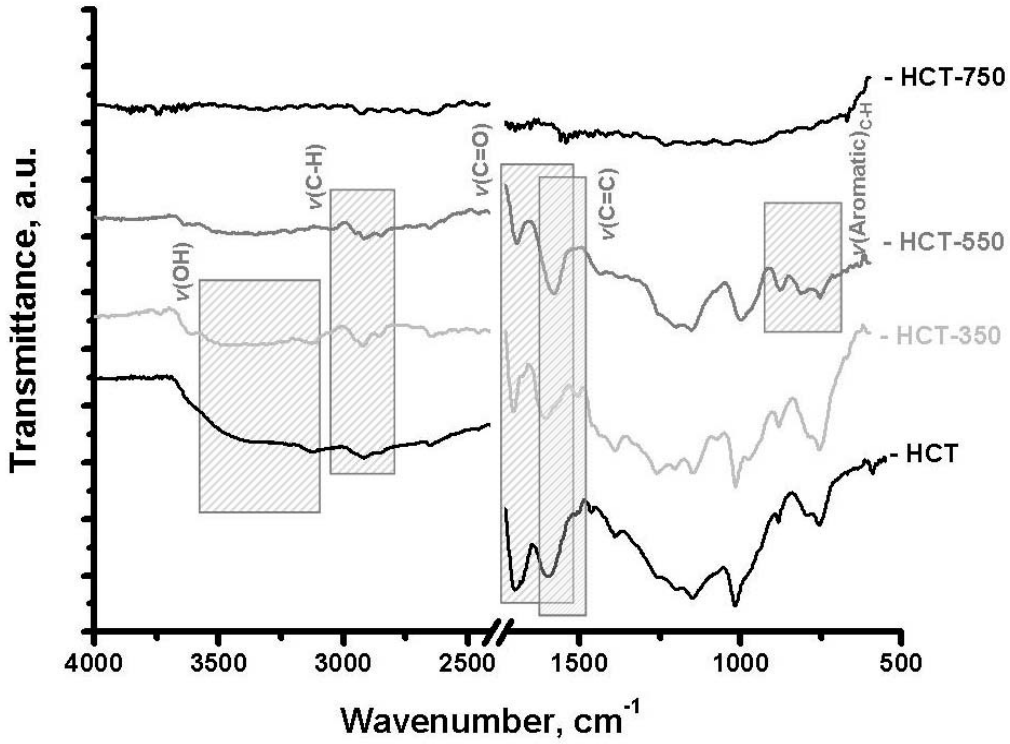

Figure 4.13: FT-IR spectra of synthesised tubular carbons (a) HCT, (b) HCT-350 (c) HCT-550, and (d) HCT-750.

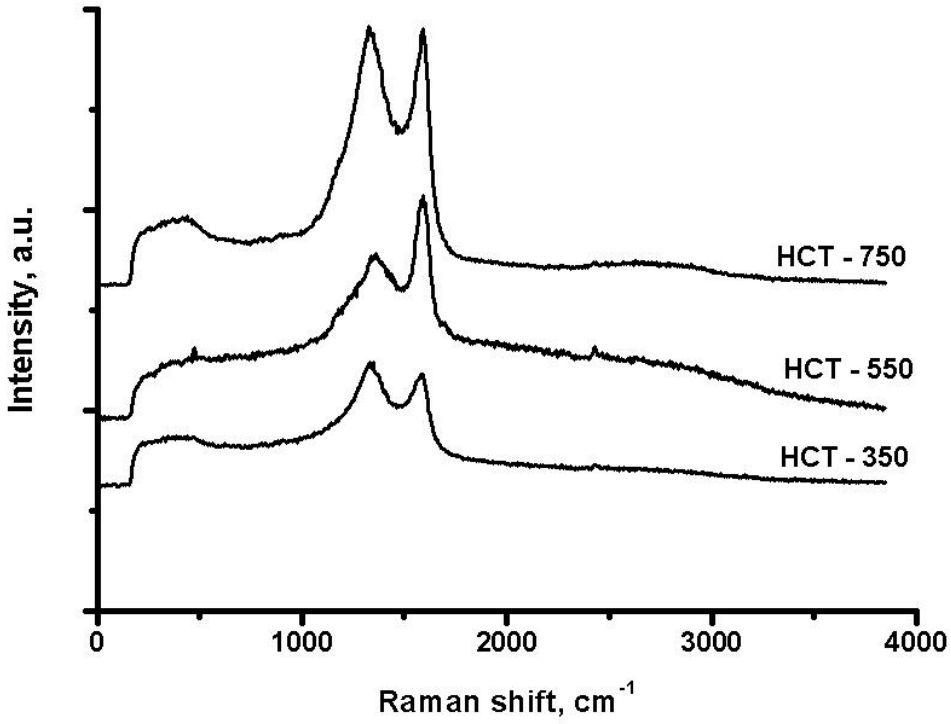

Figure 4.14: Raman spectra of HCT–350, HCT–550, and HCT-750.

Raman spectroscopy confirmed the increase in the aromatic character towards a disordered, graphitic-like structure with the increase in the temperature (Figure 4.14). All samples examined, even at the lowest post-carbonisation temperature of 350 ^{o}C, present typical D (1336 cm^{-1}) and G (1579 cm^{-1}) bands, indicating the presence of disordered carbon and graphitic-like domains.[122] Once the temperature is increased to 550 and 750 °C, respectively the G band becomes more and more pronounced, indicating structure condensation and aromatization as also confirmed by HR-TEM (Figure 4.11.f).

High resolution XPS scans of the C 1(s) photoelectron envelope were deconvoluted to examine the varying surface functionality of the presented tubular carbons as a function of post-carbonisation temperature (Figure 4.15). Deconvolution revealed peaks common to all the presented materials, namely a peak corresponding to $–CH_x$ / C-C (284.5 eV, **C1**) with an associated π->π* shake-up satellite (292 eV, **C5**), two peaks related to oxygenated carbon species; C–O (286.7 eV, **C3**) and C=O (288.7 eV, **C4**), and finally a spectral component (285.7 eV, **C2**) included to compensate for the asymmetry of the C 1(s) peak. For HCT material, the C1 peak represents the largest envelope contribution (peak area 62.1 %) whilst C3 (19.0 %) and C4 (8.3 %) peaks can also be observed confirming the existence of oxygenated surface groups (Figure 4.15.a). Similar C 1(s) spectral features are also observed for HCT-350, indicating still the presence of oxygenated functionalities such as C=O or C-O, although the relative peak areas are slightly reduced (Figure 4.15.b).

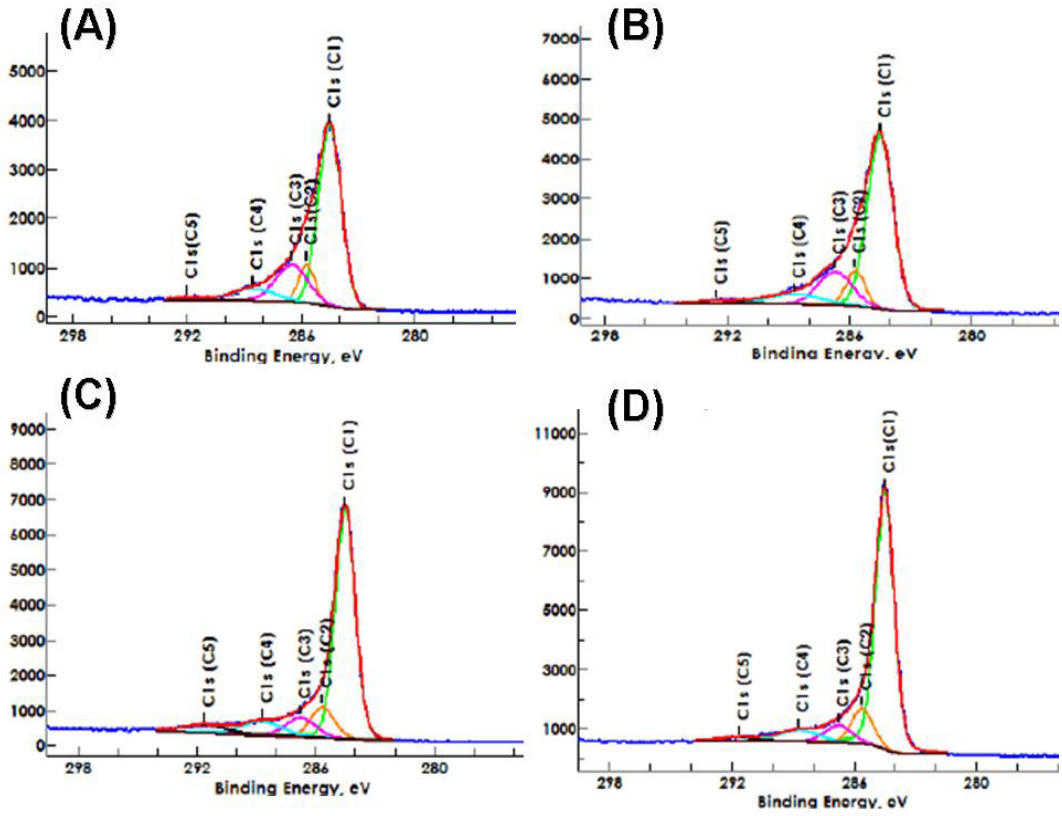

Figure 4.15: High resolution XPS scans of C 1(s) photoelectron envelope for (a) , (b) HCT-350, (c) HCT-550, and (d) HCT-750.

An increase in post-carbonisation temperature results in the C1 peak increasing in intensity in comparison to the other four peaks (Figure 4.15.c), dominating the spectra for HCT-750 material (Figure 4.15.d) indicating the development of an increasingly condensed carbon structure and the development of an extended aromatic sp^2 pseudo-graphitic motif. Corresponding O 1(s) spectra presented deconvoluted spectral peaks attributed to C=O (O1) and C–O (O2) groups (Figure 4.16). Again, by increasing post-carbonisation temperature, significant changes in the percentage area ratio for the O1 and O2 peaks was observed, showing increasing spectral dominance for O2 species as the overall material "O" content decreases (Table 4.3). Elemental composition determined from XPS survey scan are in relatively good agreement with elemental analysis data, the results indicating that with increasing the temperature an increase in the surface carbon content occurs (from 68.9 wt% for HCT to 92.2 wt% for HCT-750) and the amount of oxygen decreases significantly (from 26.5 wt% for HCT to 6.9 wt% for HCT-750) (Table 4.3). Thus, the surface chemistry (and by implication surface polarity) of these carbonaceous tubular nanostructures can indeed be finely tuned by selection of an appropriate post-carbonisation temperature.

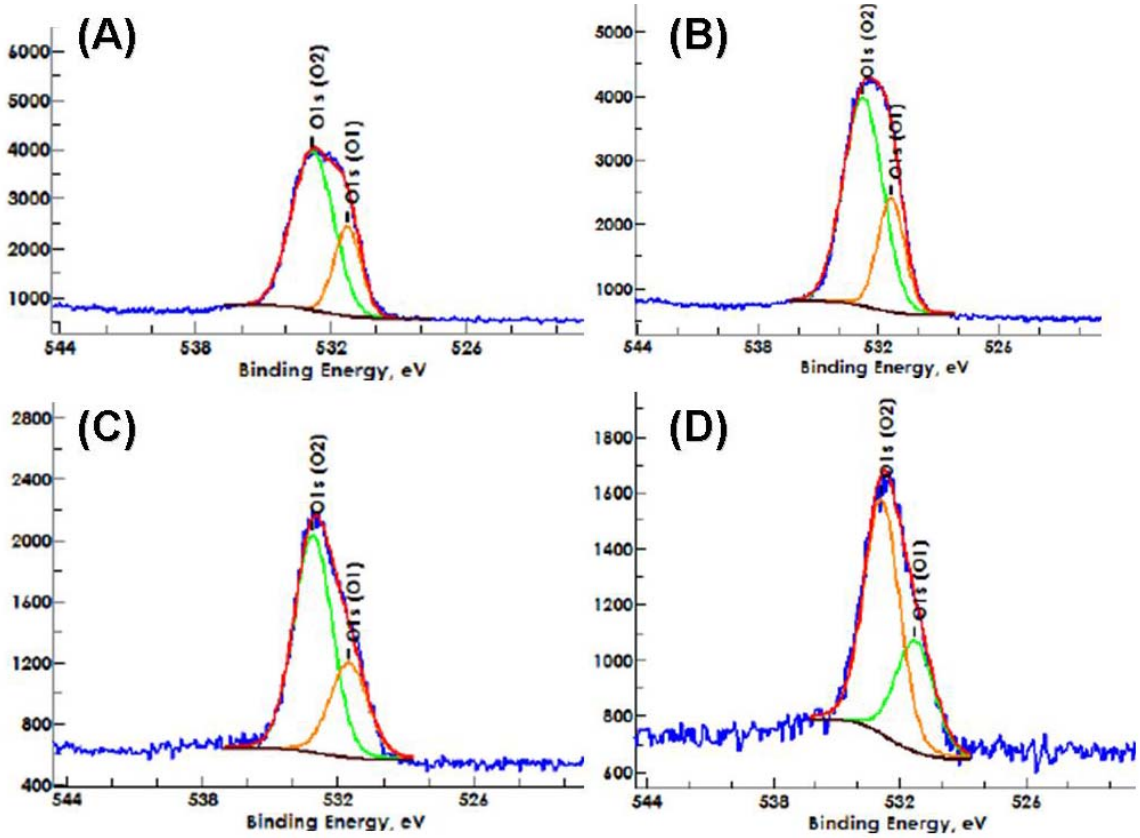

Figure 4.16: High resolution XPS scans of O 1(s) photoelectron envelope for (a) , (b) HCT-350, (c) HCT-550, and (d) HCT-750.

Table 4.3: Peak area contributions after deconvolution of C 1(s) and O 1(s) photoelectron envelopes as a function of post-carbonisation temperature treatment.

Sample	C 1(s) (%area)					O 1(s) (%area)	
	sp^2 [1]	Asymmetry [2]	C-O [3]	C=O [4]	$\pi \rightarrow \pi^*$ [5]	C-O [6]	C=O [7]
HCT	62.1	9.3	19	8.3	1.3	73	27
HCT-350	62.8	9.8	16.6	8.4	8.5	72.5	27.5
HCT-550	68.3	10.7	8.3	8	4.7	69.5	30.5
HCT-750	73	11.3	7	6.7	2.4	66.7	32.3

Area percentages of (1) carbon sp2 peak, (2) asymmetry compensation peak, (3) C-O peak, (4) C=O peak and (5) $\pi \rightarrow \pi^*$ shake-up satellite peak in XPS scans of C1(s). Area percentages of (6) in C-O peak and (7) C-O peak in XPS scans of O1(s).

4.3.3.3. Pore Properties

The porosity of the tubular carbons was determined using N_2 and CO_2 sorption analysis (Figure 4.17; Table 4.2). The HCT and HCT-350 samples showed only negligible pore volume, typical of this open macroporous tubular morphology and of a dense low temperature hydrothermal carbonaceous wall structure. Developed microporosity was found in the materials prepared at elevated temperature (i.e. 550 and 750 ^{o}C). The N_2 isotherm of HCT-550 indicates an increase in specific surface area (i.e. 116 m^2g^{-1}) and a total pore volume of 0.14 cm^3g^{-1} of which 0.06 cm^3g^{-1} is microporosity accessible to the N_2 molecule. HCT-750 presents a specific surface area of 699 m^2g^{-1} with a total pore volume of 0.53 cm^3g^{-1} of which 0.12 cm^3g^{-1} can be contributed to microporous domains. The degree of microporosity is consistent with that found for normal, non-structured hydrothermal carbons post-carbonised at 550 ^{o}C and at 750 ^{o}C. CO_2 sorption analysis provides complementary characterisation of the micropore domains in the presented materials; HCT-550 presents a surface area of 550 m^2g^{-1} and a total pore volume of 0.16 cm^3g^{-1}, while HCT-750 presents a specific surface area of 674 m^2g^{-1} and a total pore volume of 0.21 cm^3g^{-1}. Thus HCT-550 shows less microporosity and surface area in N_2 sorption than in CO_2 sorption, while HCT-750 shows relatively comparable values for both analyses. This means that a majority of micropores already exists, but is still very small (not accessible for N_2) in HCT 550, which then only ripens while further heating to 750 °C.

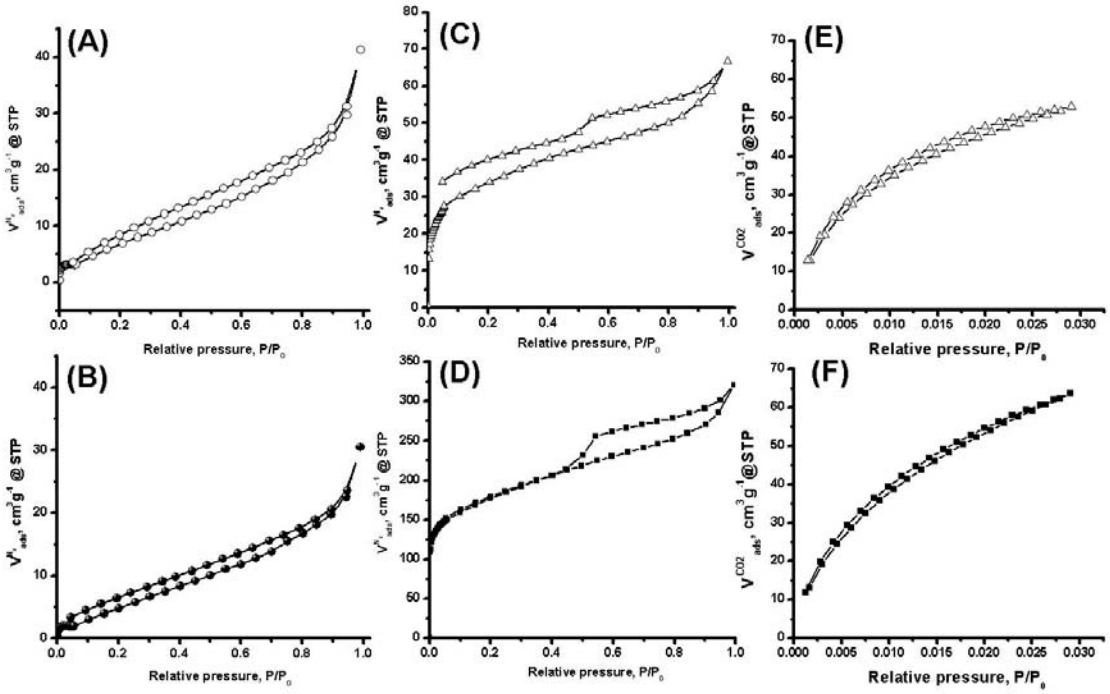

Figure 4.17: N_2 sorption isotherms for (a) HCT (b) HCT-350, (c) HCT-550 and (d) HCT-750 and CO_2 sorption isotherms for (e) HCT-550 and (f) HCT-750.

4.3.3.4. Surface Modification of Tubular Carbons with Thermoresponsive Polymers

The thermoresponsive polymer, PNiPAAm, is widely studied and already used as materials in a number of biomedical applications.[123] One reason for its biomedical popularity is its lower critical solution temperature (LCST) of 32 ^{o}C in water, which is relatively close to human body temperature. It undergoes sharp reversible hydrophilic - hydrophobic changes in water; by increasing the polymer solution temperature to above 32 ^{o}C, the polymer precipitates out of solution. Likewise, PNiPAAm - grafted tubular carbons can be expected to exhibit a very similar hydrophilic - hydrophobic changing behaviour, thus being an interesting and promising candidate for example as a carrier in controlled catch and release of drug molecules, extending thus the range of potential important applications of these materials towards biotechnological and medical fields.

Among stimuli responsive polymers, PNiPAAm is known to have the sharpest hydrophobic / hydrophilic transition at a low critical solution temperature (LCST) of 31 - 32 ^{o}C in aqueous solution.[124,125] This polymer also has been already successfully attached to silica[126] and carbon[127,128] nanostructured materials. In contrast to a silica matrix, a carbon matrix confers greater stability, pH resistivity and mechanical strength. However, reports thus far described in the literature to produce carbon / thermoresponsive polymer

hybrids encounter the previously mentioned problems regarding the functionalisation of the surface. [127,128,129,130] We have shown in the previous section that HCT possesses a high degree of surface functionality (e.g. –OH, C-O, C=O), conferring significant advantages. For potential future applications (e.g. in drug delivery or encapsulation), we therefore demonstrate the simplicity of procedure by attaching PNiPAAm onto the surface of these tubular carbons (termed HCT-PNiPAAm).

PNiPAAm was synthesized using a controlled polymerisation technique (RAFT) in the presence of a carboxylated trithioester RAFT agent, namely 4-cyanopentanoic acid dithiododecane. The molecular weight of the polymer used in our reactions was determined to be 30,000 (g mol^{-1}) using Gel Permeation Chromatography (GPC).

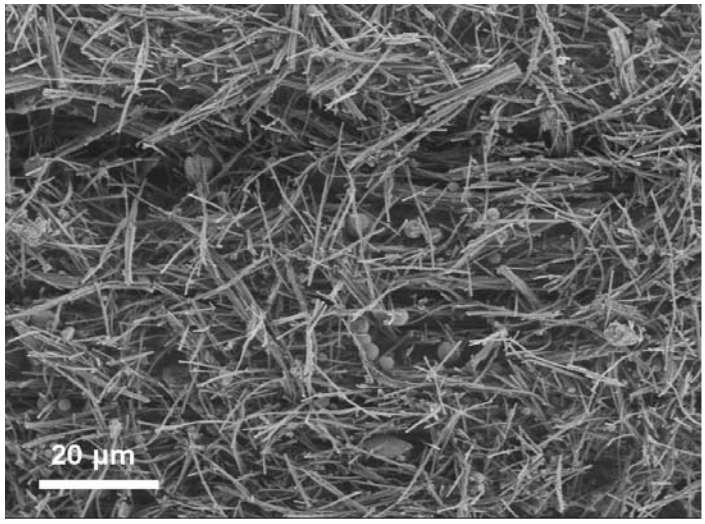

Figure 4.18: SEM micrograph of the HCT-PNiPAAm material.

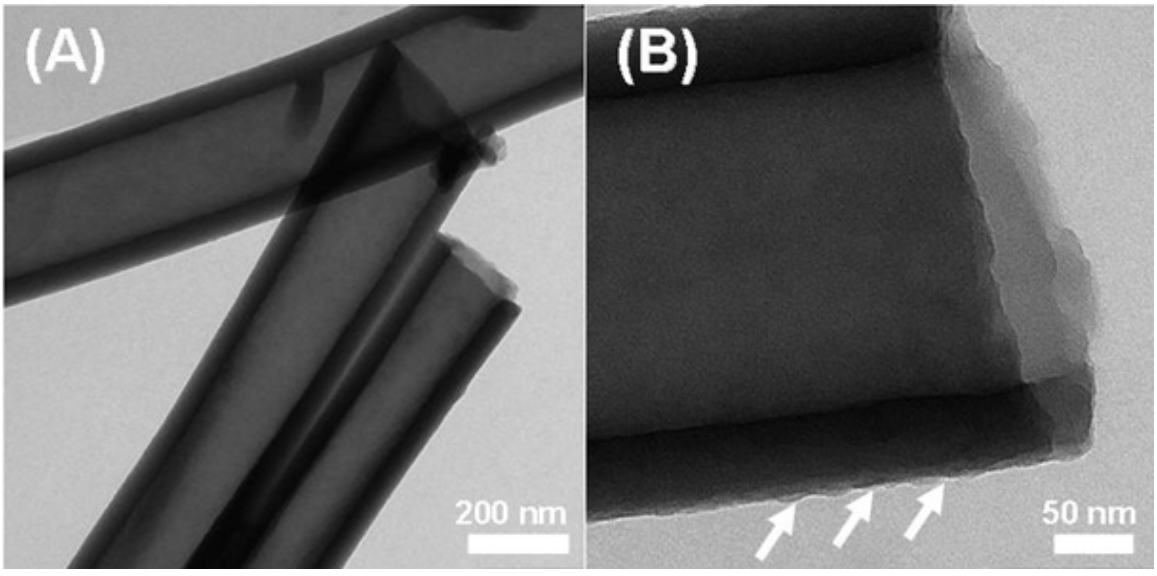

Figure 4.19: (a) and (b) (with high magnification) micrographs of HCT-PNiPAAm material.

Surface hydroxyl groups of the HCT material were first converted into amino groups via the covalent attachment of the modifier (3-aminopropyl) triethoxysilane (APS). Then, the previously synthesized carboxyl modified PNiPAAm was coupled to surface amine groups via standard amide bond formation. No significant changes in material morphology as a result of the chemical modification were observed compared to the parent HCT material, and no agglomeration was induced by polymerisation (Figure 4.18). TEM micrographs indicated maintenance of the tubular nanostructure and dimensions (e.g. diameter ~ 200 nm; Figure 4.19). Higher magnification TEM image indicated the formation of a very thin polymer layer (*ca*. ~ 2-5 nm) of grafted polymer onto the surface of the carbonaceous tubular nanostructure which is no longer smooth and some roughness can be observed (Figure 4.19.b). Successful grafting of the HCT-PNiPAAm was further confirmed by FTIR analysis, where -NH deformation modes (1565-1475 cm^{-1}) and the increase in ν(C-H) stretching mode (2925 cm^{-1}) are detected (Figure 4.20). Elemental analysis indicated an increase in %N compared to the material after APS modification, whilst a further increase in %N after polymer introduction resulting in a surface grafting density of 1.9 mg m^{-2} calculated from the following formula;

$$m_p = \frac{\%N_P \times 10^6}{\%N_{p(theory)}\left[1 - \frac{\%N_P}{\%N_{P(Theory)}} - \frac{\%N_i}{\%N_{i(Theory)}}\right] \cdot S} \qquad \textbf{(4.1)}$$

$\%N_i$ = increase in nitrogen percent of the aminated carbon from elemental analysis

$\%N_{i(theory)}$ = calculated weight percent of nitrogen in initiator

$\%N_p$ = increase in nitrogen percent after polymerization

$\%N_{p(theory)}$ = calculated weight percent of nitrogen in monomer

S = specific surface area of support..

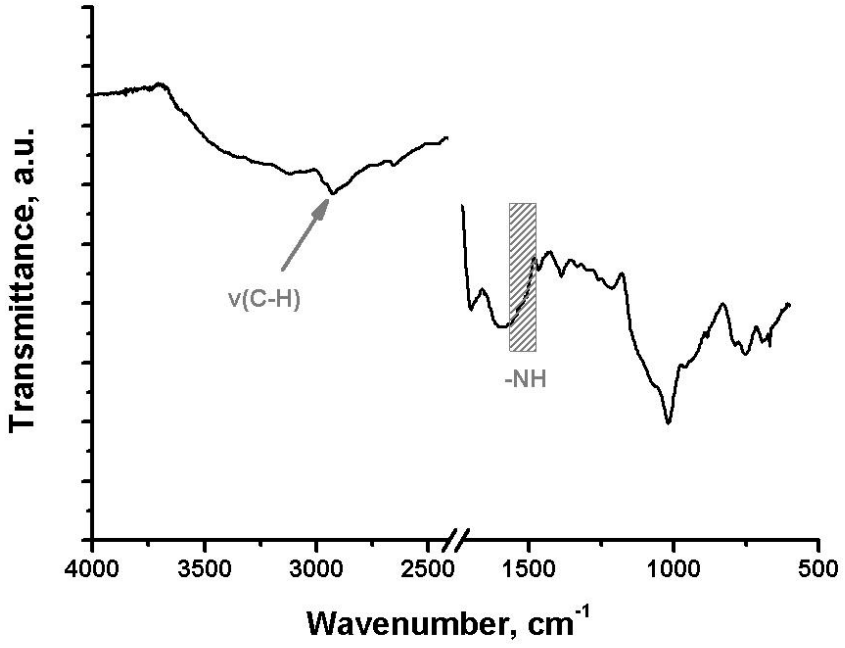

Figure 4.20: FTIR spectrum of HCT-PNiPAAm.

4.3.4.5 Hydrophilic-Hydrophobic Altering Behaviour of HCT-PNiPAAm

To test the thermoresponsive behaviour of HCT-PNiPAAm, a well dispersed aqueous solution of the hybrid material was prepared and light transmission measurements were recorded as a function of temperature cycling in the 15 - 40 ^{o}C range. HCT-PNiPAAm is well dispersed in water below the LCST because of the hydrophilic character of the hybrid. Once the dispersion is heated above 32 °C the hydrogen bonds between the HCT-PNiPAAm and water are disrupted and the tubular carbon material starts to drop out of solution. Indeed, a pure HCT sample in water (0.3 wt%) sediments after two hours at 23 ^{o}C, whereas HCT-PNiPAAm sample in water (0.3 wt%) was still well dispersed (Figure 4.21.a). Above the LCST (@ 40 ^{o}C), the HCT sample shows the same behaviour as at 23 ^{o}C, while the HCT-PNiPAAm hybrid, in contrast, sediments already after 2h (Figure 4.21.b). A fully reversible transmission hysteresis profile with heating and cooling steps is given in Figure 4.22. The observed LCST temperature is slightly higher than that of molecular PNiPAAm in aqueous solution due to the covalent attachment of the polymer to the tubular carbon surface and hence an altered molecular architecture.[88] Also the slight broadening of the thermal transition is typical for a brush-like morphology. We are presently investigating the utility of these hybrid materials as potential hollow switchable nanostructures for the encapsulation of bioactive organic molecules.

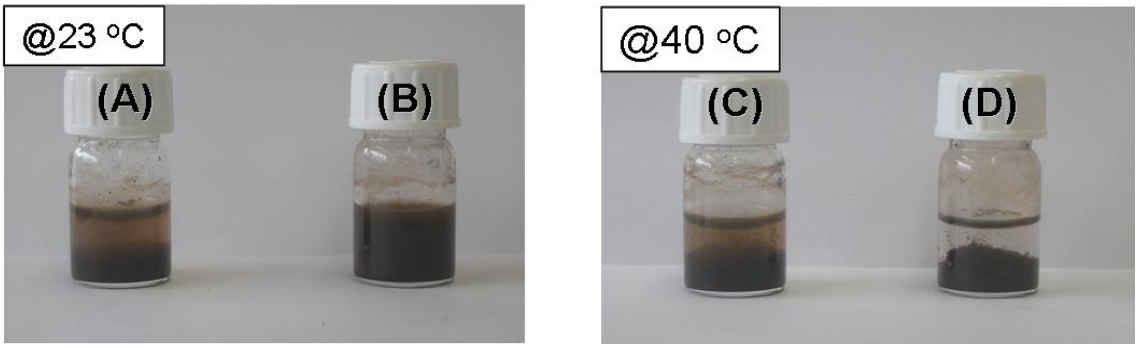

Figure 4.21: (a) HCT and (b) HCT-PNiPAAm (0.3 wt%) in water at 23 °C and (c) HCT and (d) HCT-PNiPAAm (0.3 wt%) in water at 40 °C.

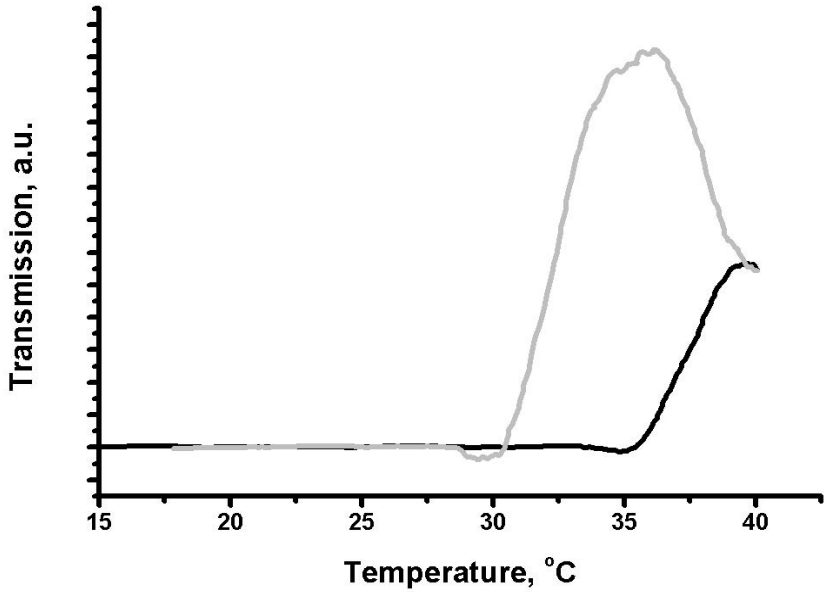

Figure 4.22: Turbidimetric analysis of LCST behaviour of HCT-PNiPAAm.

4.4. Conclusion

Carbonaceous materials with enhanced porosities and different morphologies can successfully be obtained under relatively mild hydrothermal conditions using various meso- macro-structured templates such as mesoporous silica beads and macroporous alumina membrane in combination with HTC process. The flexibility of the presented approach allows access to a wide range of functional materials with surface functionalities / chemistry tuneable via selection of post-carbonisation treatment temperature.

The spherical morphology of mesoporous silica beads Si-300 was successfully replicated yielding mesoporous carbonaceous beads. Furthermore, surface properties were controllable by varying the carbonisation temperature (e.g. high degree of oxygenated surface functionalities in as-synthesised material and increased aromatic motif in the carbonised material). Additionally, pore properties such as pore volume and BET surface area were also varied by post carbonisation showing developed microporosity for the materials treated at increased temperatures.

Likewise, tubular carbons were synthesised via hydrothermal carbonisation of 2-furaldehyde in the macropores of AAO. The synthesised tubular carbon replicas showed uniform morphology and accessible internal structure via open tube endings. Here again, control of surface properties was possible by employing post carbonisation step at different elevated temperatures. Surface characterisation indicated an increasing reduction of the oxygen content of the presented materials, while the aromatic character becomes increasingly prominent as a function of post-carbonisation temperature. Tubular nanostructures present accessible macroporosity within the hollow central space, while the carbon tube walls become increasingly microporous as post-carbonisation temperature increases. Importantly, as a proof of principle, the model thermoresponsive polymer PNiPAAm was successfully covalently attached to the surface of low temperature hydrothermal carbonaceous tubular nanostructures generating a hybrid material possessing stimuli (thermal) responsive behaviour. This feature potentially enables applications in the fields of biotechnology (e.g. enzyme immobilization) and medicine (e.g. as controllable drug micro-containers).

The example of nanocasting using bimodal silica monoliths was somewhat not straightforward, resulting in only very limited porosity. Morphology was not controllable, either. We consider that the synthesis condition (e.g. pressure, temperature, carbon precursor concentration) should be further optimised to render effective precursor impregnation and to achieve more rigid carbon network. Nevertheless, in the case of successful replication, this monolithic material together with mesoporous carbon beads would be one of the promising candidates for stationary phase in chromatography as well as, together with carbonaceous tubular nanostructures improved electrode materials in Li Ion batteries.

5. Hydrothermal Carbonisation of Carbohydrates in the presence of Block Copolymer Templates

5.1. Introduction

Carbon materials with periodic ordered pore structuring have drawn extensive attention in adsorption,[2] separation science,[3] catalysis[4] and more recently in areas of increasing technological and societal importance such as electrochemical sensors,[131] and energy storage[6]; e.g. as electrodes in Li-ion batteries, supercapacitors or as catalytic materials (e.g. as supports) for the oxygen reduction reaction in fuel cells.[7] Interest in these ordered carbons is generated from the enhanced performance originating from the nanoscale chemical environments offered by micro and mesoporous domains. Application performance can be further enhanced by the development of an organised, uniformly sized and shaped pore texture, in tandem with controlled pore wall chemistry.

As discussed in the previous chapter, production of ordered porous carbon materials has previously been achieved via hard-templating[132] of ordered inorganic solids such as zeolites[133] or mesoporous silicas (e.g. SBA-15 to CMK-3[34,134]). Such multistep syntheses involve carbon source impregnation (e.g. phenol-formaldehyde,[135] mesophase pitch,[136] sucrose[33,137,138,139]), carbonisation at elevated temperature (e.g. > 700 ^{o}C), and inorganic hard template removal (e.g. via acid etching using HF (aq)) to yield inverse replication of the hard template pore structure. Selection of solid inorganic template pore

structure in turn allows access to a variety of different ordered pore structures (e.g. *p6mm*, *Ia3d*[137,140]). In this context, Zhao *et al*. and Dai *et al*. have recently demonstrated that the use of a sacrificial inorganic template is not required, reporting on a direct route to ordered carbons via organic - organic self-assembly of a block copolymer (e.g. Pluronic® F127 or polystyrene-*b*-poly(4-vinylpyridine)) and a suitable aromatic carbon precursor (e.g. phloroglucinol[35,36] or phenol-formaldehyde[37,38,39]). Hydrogen bonding interactions play a significant role in orientating the resulting poly-aromatic network, whilst pore structuring was conventionally controlled by polymeric template (e.g. via concentration and structure), copolymer - precursor ratio, *p*H, solvent polarity and the presence of a catalyst.[141] The polymeric template was then removed either by solvent extraction or thermolysis. From a macromorphological perspective, ordered porous carbons have been prepared previously as films,[35] pellets[142] and monoliths,[143] extending material application remit still further. More recently, based on the same self-assembly / soft templating approach, the preparation of single crystal mesoporous carbons was demonstrated by Zhao *et al*., with the intention of developing these materials for future applications in nanodevices (e.g. optical devices).[144,145]

Carbons prepared by all of such strategies typically present rather chemically condensed (e.g. graphitic-like) pore walls / surfaces, which inhibits facile post chemical modification and limits surface hydrophobicity / polarity modification. In this context, the transformation of carbohydrates via the inexpensive and facile hydrothermal carbonisation (HTC) route employing mild aqueous conditions (e.g. T ~ 180 ^{o}C, P < 10 Bar) to yield functional carbonaceous materials is considered advantageous.[26,28,29,30,146] In the previous chapter, we demonstrated a combined HTC / nanocasting synthesis using sacrificial inorganic solids to yield inverse carbon replicas. However, it would be desirable to remove this process step and generate ordered porous carbonaceous materials via a direct soft templating approach, meaning that methods extensively developed for structure direction / texturing of inorganics can be transferred to preparation of ordered carbon materials. This would allow the production of high value, functional, ordered and application rich carbonaceous materials in an economical, sustainable and relatively facile manner, providing a real chemical advantage over more traditional ordered mesoporous carbons.

The HTC of D-Fructose is known to occur at a temperature as low as 130 ^{o}C; a significantly lower processing temperature compared to other hexoses (e.g. D-Glucose;

180 °C) due to a lower intramolecular dehydration energy boundary.[147] Typically block copolymer micelles or surfactant micelles used in soft templating are not stable at the high temperatures used for the HTC process.[148] Therefore, the use of D-Fructose allows access, in principle, to more stable micellar self-assembly and opens the opportunity of soft templating. Herein, we demonstrate the synthesis of ordered porous single crystalline carbonaceous materials from the hexose carbohydrate D-Fructose, via a combined aqueous HTC / soft templating approach, generating both ordered microporous and mesoporous carbonaceous materials.

5.2 Experimental

5.2.1 Chemicals

Pluronic® F127 ($EO_{106}PO_{70}EO_{106}$), F108 ($EO_{130}PO_{60}EO_{130}$) and P123 ($EO_{20}PO_{70}EO_{20}$) were purchased from Sigma-Aldrich® (Steinheim, Germany). Sodium dodecyl sulfate (SDS) was purchased from Fluka. Poly(styrene)$_{10}$-*block*-poly(ethylene oxide)$_{68}$ (PS_{10}-*b*-PEO_{68}) was purchased from Theodor Goldschmidt AG. Poly(acrylic acid)$_{40}$-*block*-poly(propylene oxide)$_{40}$ (PAA_{40}-*b*-PPO_{40}) was synthesised in the laboratory according to the procedure reported elsewhere (please see *Appendix*). D-Fructose was purchased from ABCR GmbH & Co. KG (Karsruhe, Germany). D-Glucose monohydrate, 5-hydroxymethyl-2-furaldehyde (HMF), Sulfuric acid and 1,2,4-Trimethylbenzene (TMB) was purchased from Sigma-Aldrich® (Steinheim, Germany).

5.2.2 Synthesis

Synthesis was performed at 130 °C in H_2O using a water-soluble block copolymer structural directing agent (e.g. Pluronic® F127) and the carbohydrate carbon source (e.g. D-Fructose). In a typical synthesis, 0.25 g of block copolymer or surfactant and 1.20 g of D-Fructose (Fru) (or D-Glucose monohydrate (Glu) and HMF for comparison test) were dissolved in 10 mL of water by stirring. The solution was then heat-treated in a sealed steel autoclave (Parr, Acid Digestion Vessel 4744) at 130 °C for ~ 120 h. The molar composition ratios were Fru / F127 / water = 1 : 0.0028 ; 83.4, Fru / F108 / water = 1 : 0.0115 ; 83.4, Fru / P123 / water = 1 : 0.0065 ; 83.4, Fru / PS-*b*-PEO / water = 1 : 0.0094 ; 83.4, Fru / PPO-*b*-PAA / water = 1 : 0.0072 ; 83.4 and Fru / SDS / water = 1 : 0.13 ; 83.4.

With particular respect to the F127 – Fru system, template – Fru ratios were varied stepwise up to Fru / F127 / water = 1 : 0.0224 ; 83.4. After reaction, a dark-brown solid precipitate was recovered, which was washed with water and ethanol, dried and then calcined under N_2 at 550 ^oC with the ramp time of 4 h and hold time of 2 h. When using PPO-*b*-PAA, a cross-linked gel was obtained, which was freeze-dried and calcined in the same manner. For pore size control, TMB was added to the F127 / Fru reaction mixture (mol_{F127} : mol_{TMB} = 1 : 0.92, 1.53, and 2.30). The other procedures were identical as that outlined for the F127-Fru system (Fru / F127 / water = 1 : 0.0028 ; 83.4). Soxhlet extraction of the template – carbon composite was performed by refluxing ethanol for 2 nights.

5.3 Selection of Structural Directing Agents

Material morphology after template removal varies with differing structural directing agents (Figure 5.1). The material synthesised with F127 presents ~ 5 μm sized particles possessing faceted edges (Figure 5.1.a), whilst the material synthesised using F108 presented similar macromorphological texturing, where particles were connected with each other (Figure 5.1.b). When using P123, a bulk material consisted of small aggregated particles (< ~ 1 μm) was obtained (Figure 5.1.c). The use of PPO-*b*-PAA block copolymer led to 3D-continuous structures with monolithic macromorphology composed of much smaller particles (~ 20 nm, Figure 5.1.d, inset showing TEM micrograph of the observed smaller particles). In the case of using PS-*b*-PEO, near spherical particles (~ 5 μm) with some surface roughness was observed, accompanied with some smaller particles (< ~ 1 μm, Figure 5.1.e), whilst, in the case of SDS, homogeneous spherical particles (~ 5 μm) were observed (Figure 5.1.f). The material synthesised without any structural directing agents for comparison purpose represents approximately 5 μm – sized spherical particles with coexistence of some much smaller particles (< ~1 μm, Figure 5.1.g). The presented faceted edge / layered morphology seen when using F127 and F108 can be considered indicative of some particular effect of block copolymer templating (Figure 5.1.a and b).[144,145]

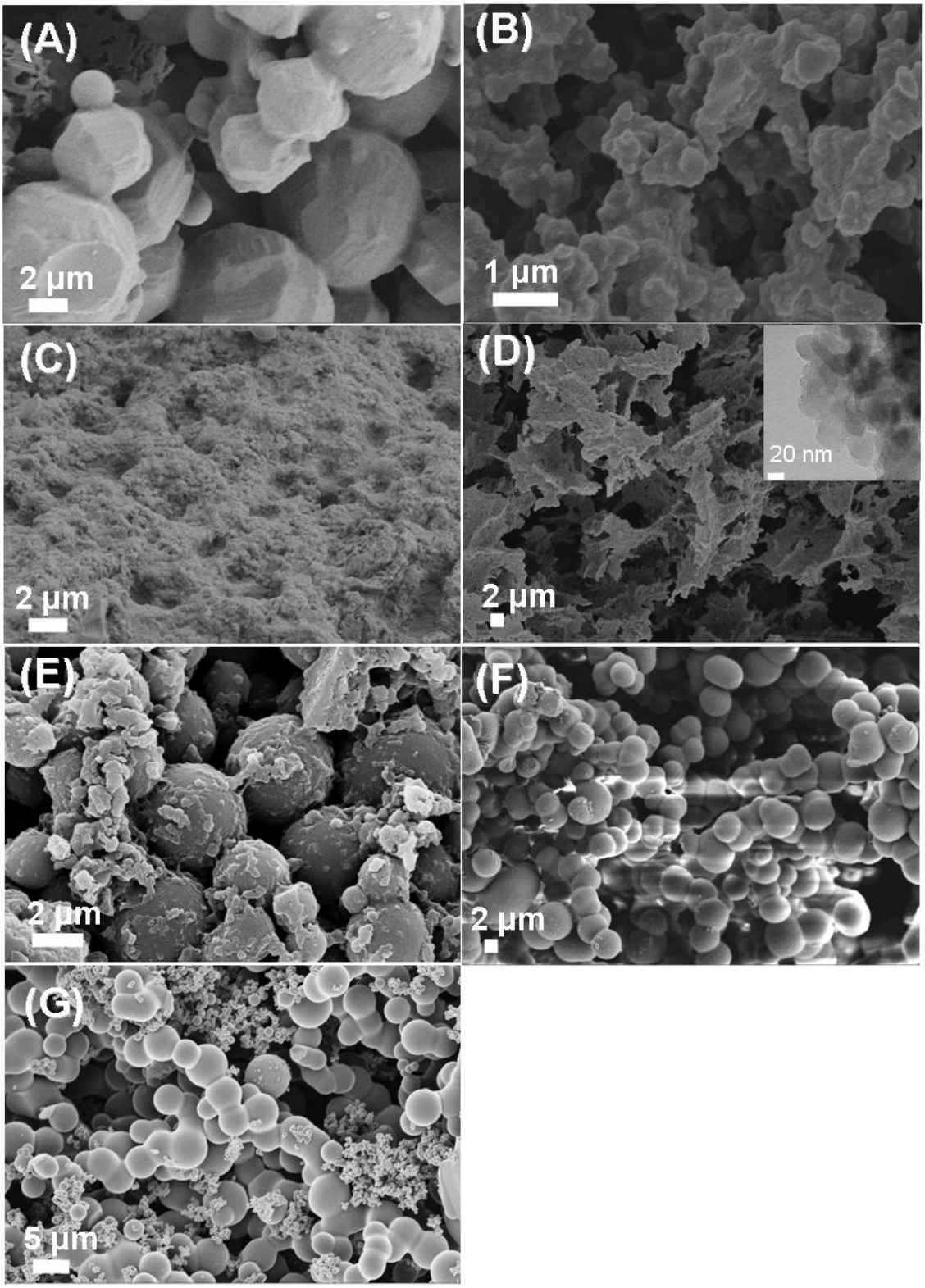

Figure 5.1: SEM micrographs of obtained carbonaceous materials synthesised with (a) F127, (b) F108, (c) P123, (d) PPO-*b*-PAA, (e) PS-*b*-PEO, (f) SDS and (g) of the material synthesised without any structural directing agents.

In order to investigate the structure at nanoscale (e.g. pore regularity / symmetry), small angle X-ray scattering analysis (SAXS) measurements were carried out for the obtained materials after calcination uner N_2 at 550 ^oC (Figure 5.2). The materials synthesised with F127 and F108 show well-resolved peaks at q = 0.54 and 0.44, respectively, indicative of existence of some structural ordering (Figure 5.2.a and b). Each peak is accompanied by a small shoulder peak located around q = 0.93 and 0.78, respectively. The materials synthesised with PS-*b*-PEO also showed one very broad shoulder peak at q = ~ 0.5 (Figure 5.2.e), whilst the use of the other structural directing agents did not lead to occurrence of any peaks (Figure 5.2.c, d, and f). For the standard material, (i.e. prepared in the absence of any block copolymer structure directing agent) no peaks were observed (Figure 5.2.g).

The observed SAXS peaks are considered indicative of the existence of some structural regularity inside the carbonaceous materials derived from block copolymer micellular templating, particularly in materials prepared in the presence of F127 and F108 block copolymers. Due to its widespread usage in many soft templating approaches and to increased opportunities for the system comparison with the other reported systems, the F127 system was selected for further investigation.

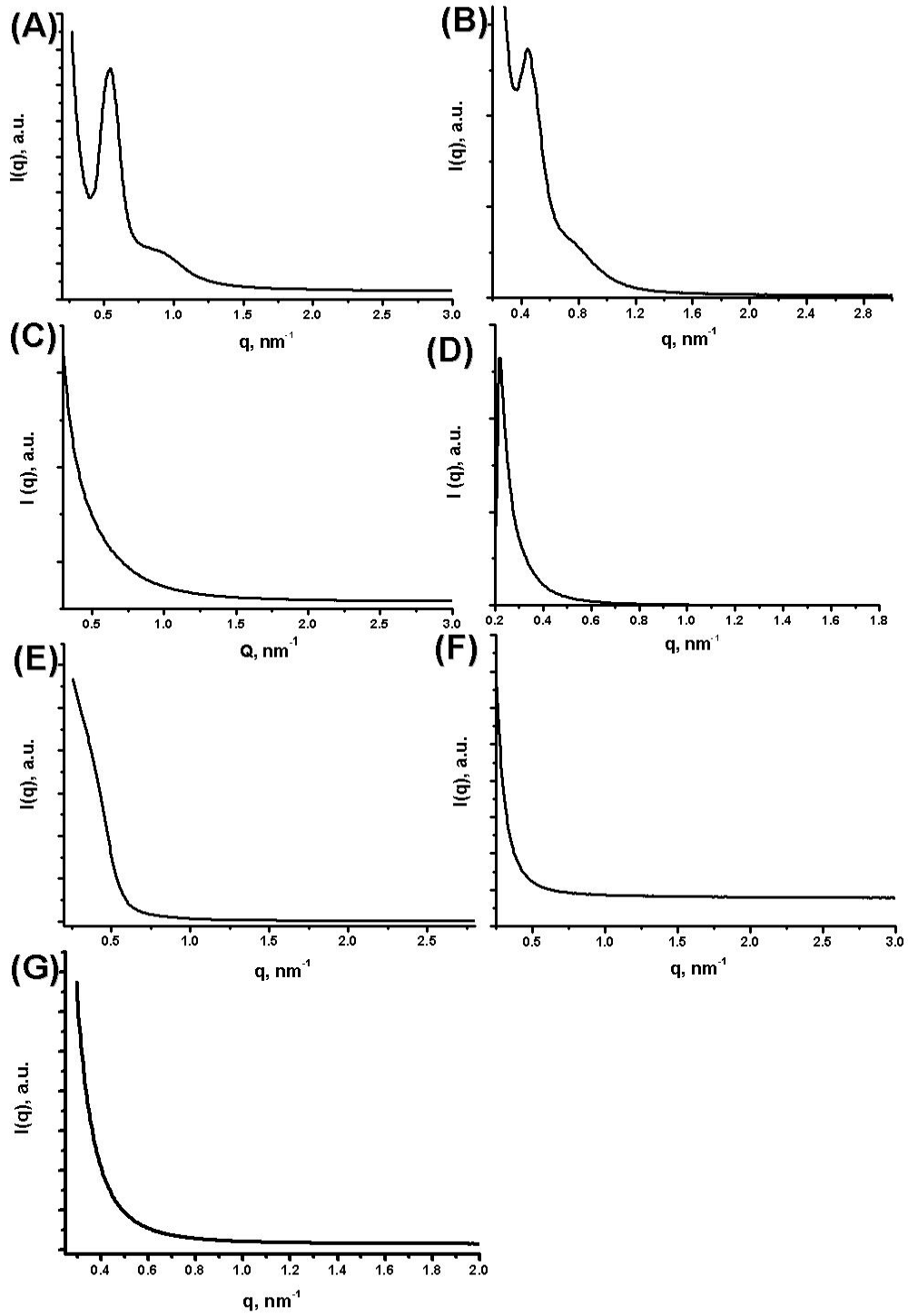

Figure 5.2: SAXS patterns of materials synthesised with (a) F127, (b) F108, (c) P123, (d) PAA-*b*-PPO, (e) PS-*b*-PEO, (f) SDS as structural directing agents and (g) of the material synthesised without any structural directing agents.

5.4 Effect of F127-Fru Composition

For the optimisation of the F127 system, the composition of F127 and Fru was varied from ($F127_{mol}$) ; (Fru_{mol}) = 0.5 ; 1.0028 to 8 ; 1.0028, where the amount of water was kept as 10 g. Figure 5.3 (a) ~ (e) show the SAXS patterns of the materials synthesised with the different F127-Fru molar ratios. The scattering patterns (a) to (d) show peaks at the q values between 0.5 and 0.6, among which the pattern (b) shows the most well-dissolved discrete peak at the q = 0.54. Scattering patterns of (a), (c) and (d) also give one or more peaks, but they are very broad, indicative of decreased structural homogeneity. In the case of the materials synthesised with the ratio of 8 : 1.0028 (Figure 5.2.e), no peak was observed meaning a near complete lack of long range structural order. Thus, the system was optimised to F127 : Fru = 1.0 ; 1.0028 for further investigation.

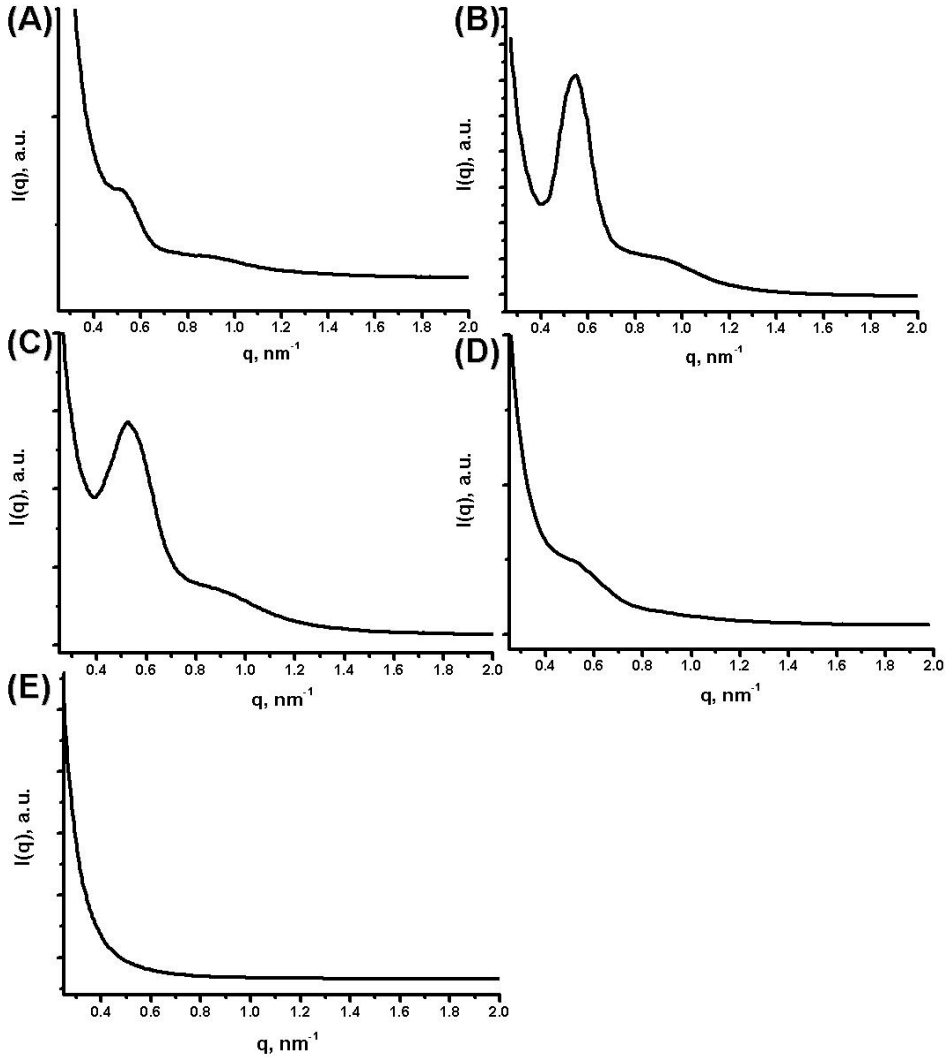

Figure 5.3: SAXS patterns of the carbonaceous materials synthesised with the F127-Fru compositions of (a) 0.5 ; 1.0028, (b) 1.0 ; 1.0028, (c) 2.0 ; 1.0028, (d) 4.0 ; 1.0028 and (e) 8.0 ; 1.0028.

For the optimised system, the isolated composite showed well ordered structure with an F127 micelle diameter of ~ 10 nm and HTC wall thickness of ~ 6 nm by TEM observation (denoted as C-MPG1-*com*) indicating the successful assembly of F127 copolymer species and Fru (Figure 5.4). Synchrotron small angle X-ray scattering analysis (SSAXS) of this composite demonstrated a well-resolved pattern with the *d*-spacing value of the first peak equivalent to 16.8 nm, corresponding to a unit cell parameter of 23.6 nm for cubic *Im3m* symmetry (Figure 5.5, inset; 2D scattering pattern).[149] Nitrogen sorption isotherms of the composite showed only negligible BET surface area and pore volume for this composite (Table 5.1).

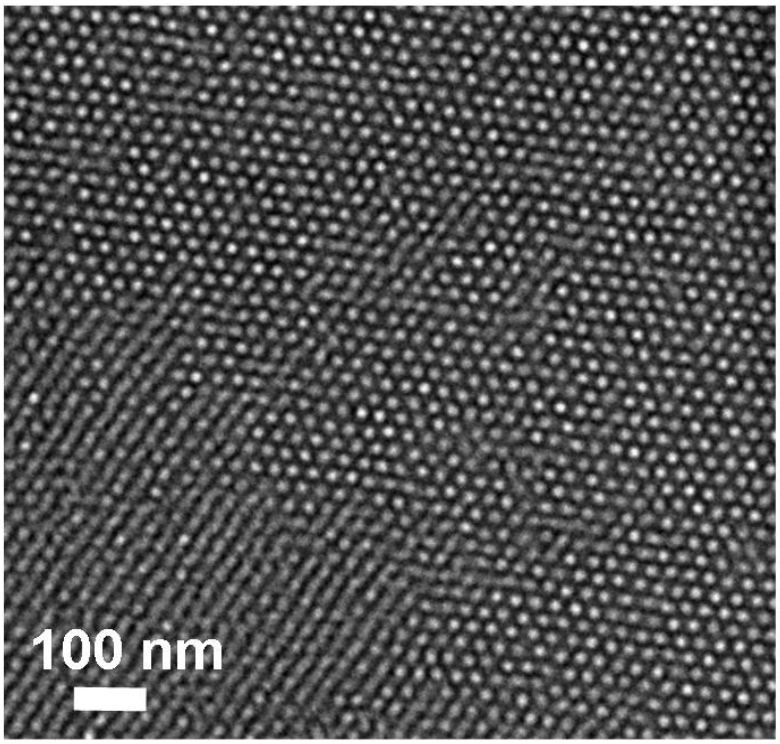

Figure 5.4: TEM micrograph of C-MPG1-*micro* before template removal.

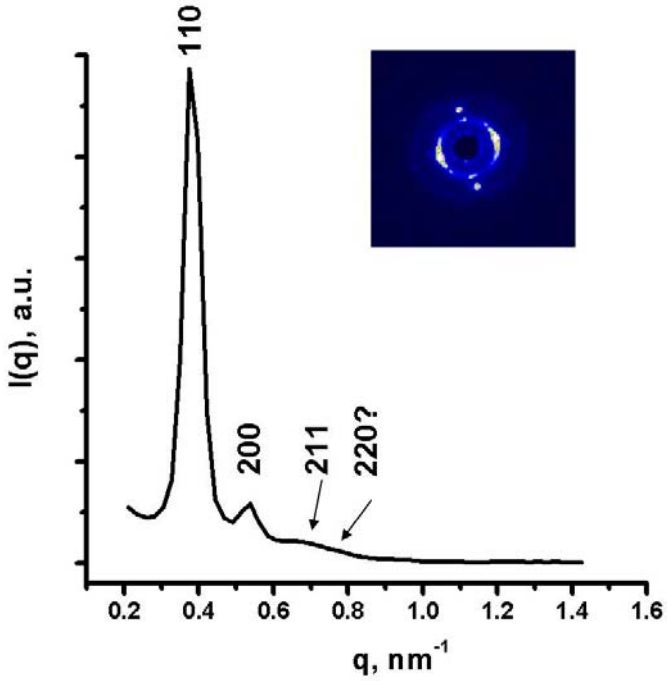

Figure 5.5: SSAXS pattern of C-MPG1-*com* (before template removal, insert; 2D scattering pattern).

Further heat treatment under N_2 (e.g. at 550 ^oC) resulted in the decomposition of the thermally labile template to yield a carbonaceous product (denoted as C-MPG1-*micro*), composed of 82.6 wt% C, 14.2 wt% O, and 3.2 wt% H, respectively (Table 5.1). SEM image analysis of C-MPG1-*micro* reveals a degree of layering of the material structure, indicative of a layer-by-layer growth mode yielding relatively uniform cuboctahedron-like particles in the 1 – 10 μm size domain (Figure 5.1.a and 5.6).

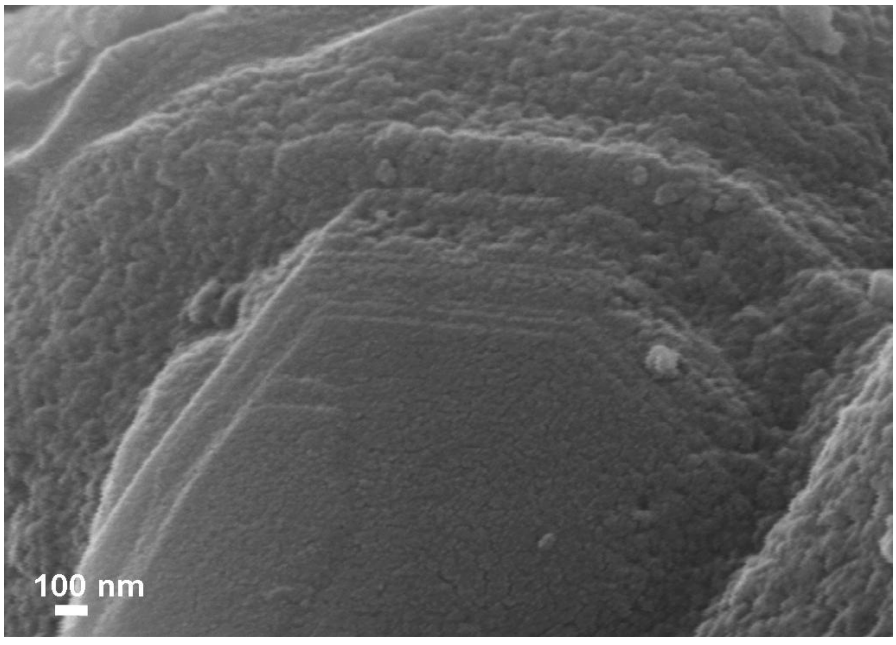

Figure 5.6: SEM micrograph of C-MPG1-*micro* showing the stacking layers.

Whilst of similar size to previously reported HTC materials, cuboctahedron-like particles with stacking layers are considered indicative of the growing direction of the hydrothermal carbon network by the templating phase as well as of the formation of single crystalline particles.[145] (High Resolution) Transmission Electron Microscopy ((HR)TEM) images of C-MPG1-*micro* show a long-range regularly ordered pore structure (Figure 5.7.a - d). SSAXS analysis of C-MPG1-*micro* indicates the formation of a near perfect cubic *Im3m* symmetry (Figure 5.8). The obtained 2D scattering pattern (Figure 5.8 insert) is indicative of a single-crystalline nature to this material and presents well-resolved peaks at *q*-spacing values of 0.51, 0.72 and 0.87 nm^{-1} respectively in combination with less intense peaks at higher *q* values. This corresponds to a *d*-spacing of 12.3 nm equating to a unit cell parameter of 17.4 nm.[149]

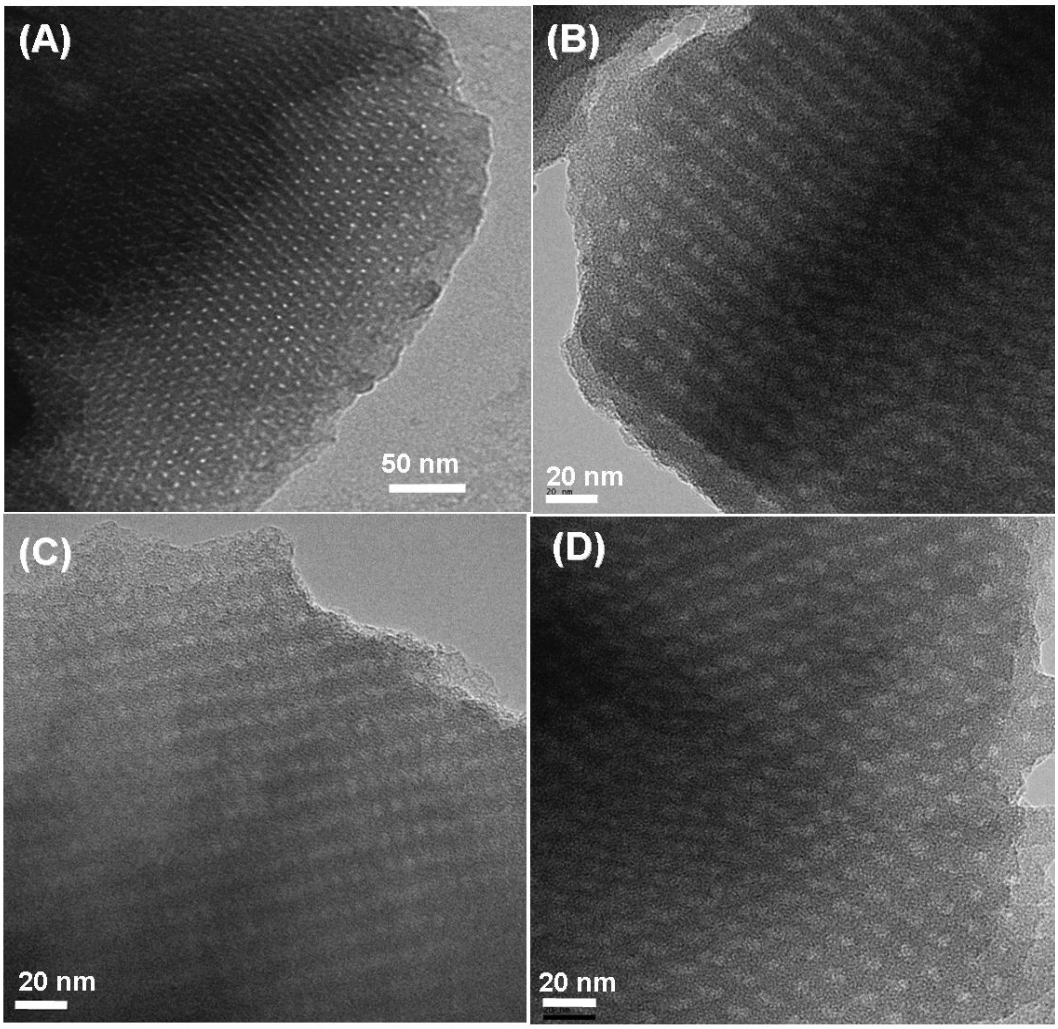

Figure 5.7 (a) TEM and (b) (c) and (d) HRTEM micrographs of C-MPG1-*micro* from different directions.

This cell parameter value is considerably smaller than the structural dimensions observed before template removal (~ 23.6 nm) believed to be the result of structural shrinkage upon thermal treatment / decomposition (e.g. carbon network condensation). Some unassigned peaks were also observed indicating the presence, in part, of a mixed phase, but nevertheless, the calculated SSAXS unit cell parameter agrees well with the presented HRTEM images. Unusually both SSAXS and HRTEM indicate the generation of a very thick pore wall feature for C-MPG1-*micro* with dimensions of between 7 - 10 nm.

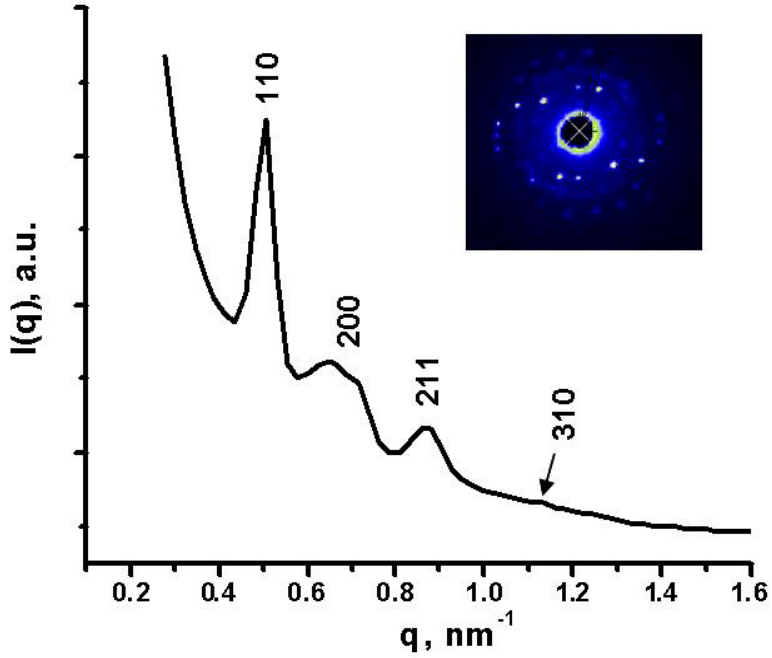

Figure 5.8: SSAXS pattern of C-MPG1-*micro* (inset; 2D scattering pattern).

Table 5.1: N_2 sorption characteristics and elemental analysis data.

Sample	[a] S_{BET}, m^2g^{-1}	[b] V_{micro}, cm^3g^{-1}	[b] V_{meso}, cm^3g^{-1}	[b] V_{total}, cm^3g^{-1}	[c] PS, nm	[d] C, %wt
C-MPG1-*com*	13	0	0.01	0.01	-	63
C-MPG 1-*micro*	257	0.11	0.03 (22 %)	0.14	0.9	83
C-MPG 1-*meso*	116	0.04	0.06 (60 %)	0.1	1.0 , 4.0	79

[a] BET surface area; [b] Microporous, mesoporous and total pore volume from QSDFT method, with the % ratio of mesopore to total pore volume in parentheses; [c] Pore size calculated from QSDFT method; [d] Elemental analysis data.

N_2 sorption analysis of C-MPG1-*micro* indicates a microporous type I isotherm of a non-reversible nature believed to be due to possible structural changes in pore wall dimensions during gas sorption processes (Figure 5.9.a).[76] Specific surface area and total pore volume were calculated as 257 $m^2 g^{-1}$ and 0.14 $m^3 g^{-1}$ respectively (Table 5.1). The pore size distribution presents a sharp peak at a diameter of 0.9 nm and a less discrete broader shoulder centred around 2 nm (Figure 5.9.b). Comparison with C-MPG1-*com* indicates that indeed pores are opened upon removal of the block copolymer template via a thermolytical process.

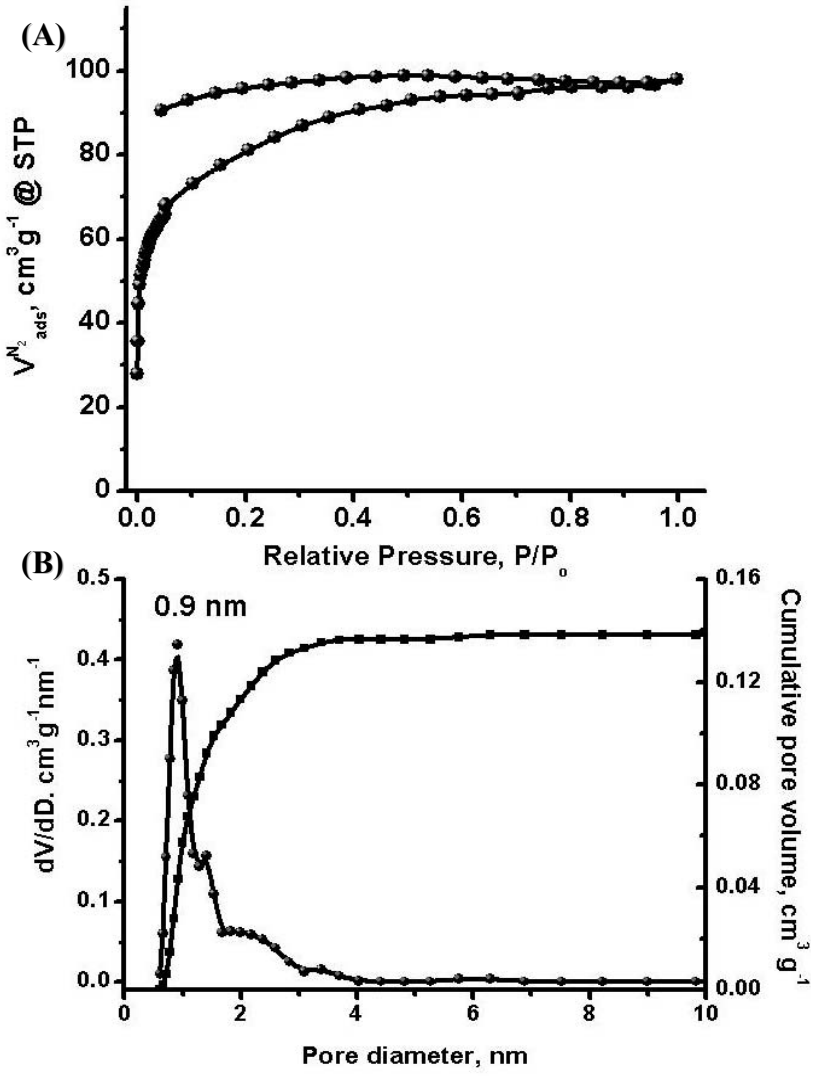

Figure 5.9: (a) N_2 sorption isotherms and (b) QSDFT pore size distribution of C-MPG1-*micro*.

5.5 Carbon Framework and Carbon Surface Functionalities

Thermogravimetric analysis (TGA) of C-MPG1-*com* (i.e. F127 / HTC composite) presented a significant symmetrical mass loss event at ~ 340 ^{o}C followed by a smaller and broader secondary charring step at ~ 590 ^{o}C (Figure 5.10.a). The first *d*TG peak is believed to correspond to the F127 decomposition and the second much broader thermal event to further condensation / aromatisation of the carbon structure.[150] After the template removal, C-MPG1-*micro* presents a broad rather asymmetric mass loss event centred at *ca.* ~ 600 ^{o}C, demonstrating firstly the thermolytic removal of the copolymer template, and secondly the formation of a functional but relatively stable ordered functional carbonaceous material (Figure 5.10.b).

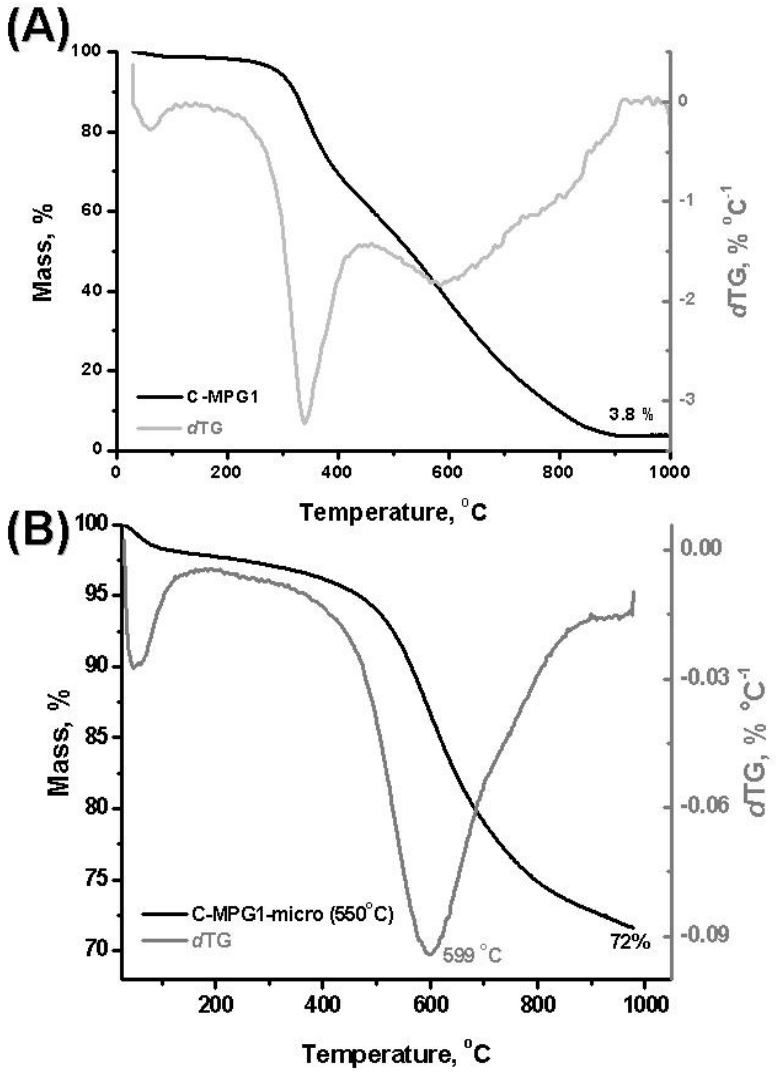

Figure 5.10: TGA (black) and dTG (grey) curves of (a) C-MPG1-*com* and (b) C-MPG1-*micro*.

Comparison of FTIR spectra of C-MPG1-*com* (before template removal) and C-MPG1-*micro* (after) also indicates the near complete removal of F127 template showing a decrease in ν(C-H) stretching mode (~ 2917 cm^{-1}) and –OH stretching mode (3700-3100 cm^{-1}) derived from F127 (Figure 5.10). Surface oxygenated groups are well preserved even after calcination at 550 ^{o}C, presenting –OH stretching mode (3700-3100 cm^{-1}), C=O stretching mode from C(O)OH / lactone groups (1800-1520 cm^{-1}) and conjugated C=C / olefinic species (C=C-O) (stretching mode between 1650-1450 cm^{-1}).

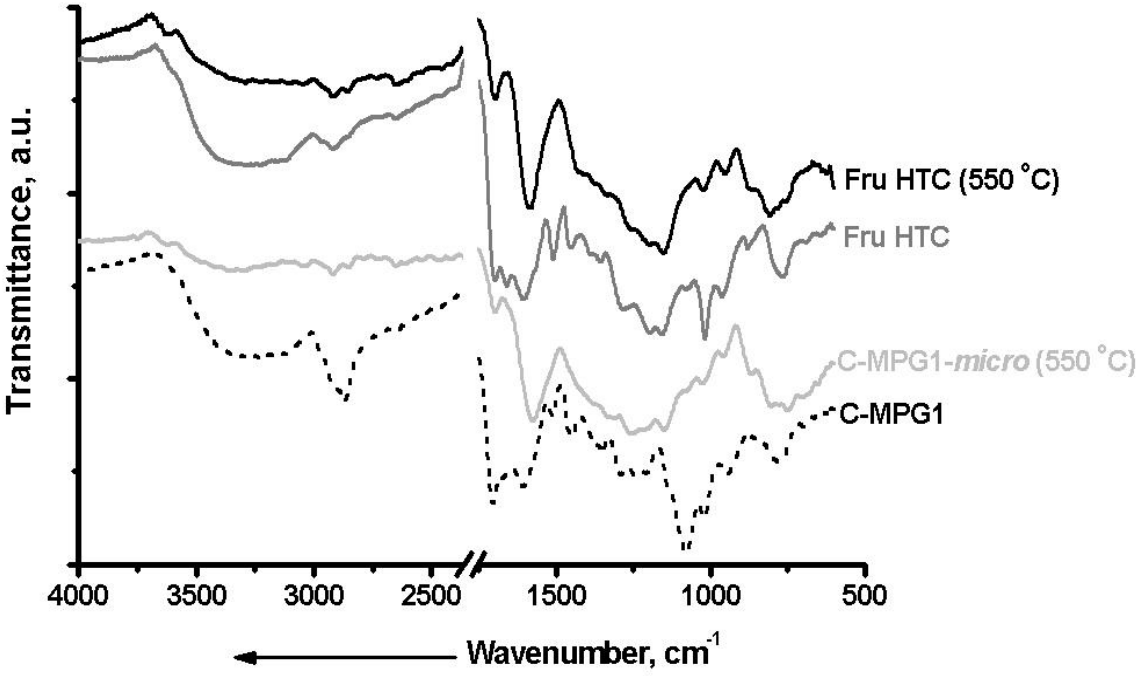

Figure 5.11: FTIR spectra of C-MPG-1-*com* and C-MPG-1-*micro* and fructose-derived reference carbonaceous samples before and after calcination under nitrogen at 550 ^{o}C from bottom to top.

A similar trend is observed for the system without F127, namely between Fru HTC and Fru HTC@550 ^{o}C. Here, Fru HTC corresponds to a hydrothermally carbonised Fru in the absence of a F127 template and Fru HTC@550 ^{o}C corresponds to Fru HTC which was further calcined at 550 ^{o}C under N_2. Importantly, Fru HTC@550 ^{o}C and C-MPG1-*micro* show almost the same features in their spectra. Thus, it can be said that surface functionalities of the final material are not significantly affected by employing this soft templating route.

^{13}C cross polarisation magic angle spinning (CPMAS) NMR spectroscopy analysis of the F127 – HTC composite (i.e. C-MPG1-*com*) presented all the characteristic features of hydrothermal carbon materials, including resonances associated with carbonyls (e.g.

aldehydes / ketones at δ = 210 ppm and carboxylic acids at δ = *ca.* 170 ppm), oxygen-substituted, protonated and non-protonated C=C bonds resonating (at δ = 150 ppm); aromatic carbon environments characteristic of furan motifs and long-range conjugated double bonds at δ = 125 - 129 ppm as well as aliphatic groups resonating in the δ = 20 – 50 ppm region (Figure 5.12).[31] Additionally, a very intense asymmetric peak at δ = 75 ppm associated with hydroxylated methylene groups (R-CH_2-O-R) of the block copolymer F127 template is also observed.

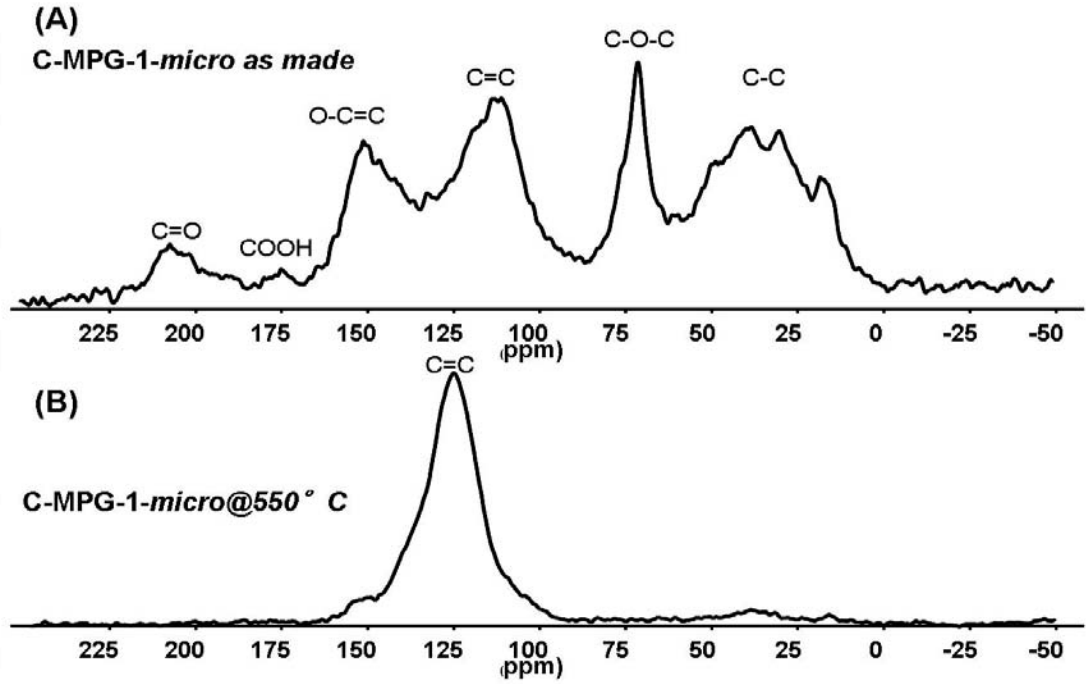

Figure 5.12: ^{13}C CP MAS NMR spectra of (a) C-MPG1-*com* and (b) C-MPG1-*micro*.

The effect of heat treatment at 550 ^{o}C on C-MPG-*com* is the condensation of the carbon structure to increasingly traditional aromatic features as indicated by a single broad resonance at δ = 125 - 127 ppm, of an asymmetric nature indicative of the presence of some residual oxygenated aromatic groups (e.g. shouldering at δ = 150 ppm) (Figure 5.12.b). The peak at δ = 75 ppm corresponding to F127 resonances disappear indicating the destruction of the template during the thermal treatment step. This bulk solid analysis agrees well with previously discussed TGA and FTIR analysis.

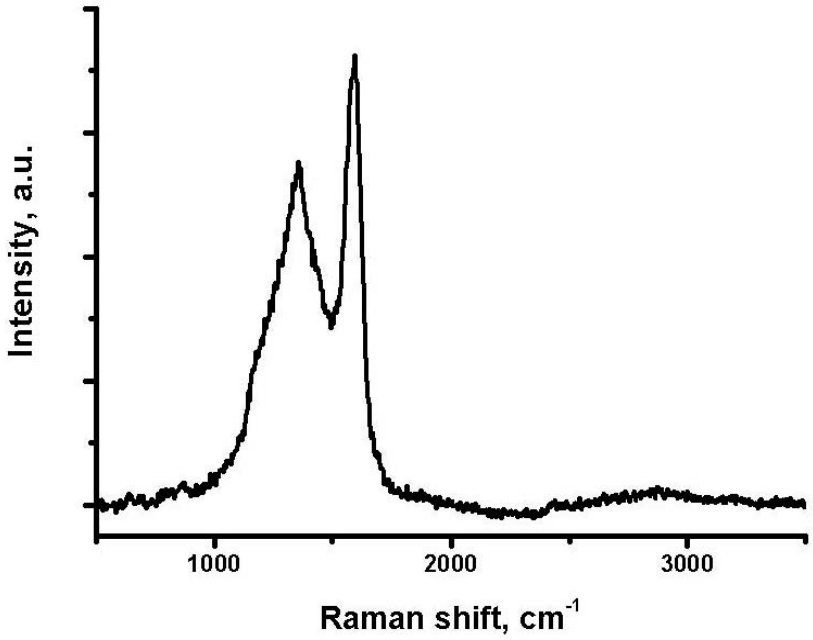

Figure 5.13: FT-Raman spectrum of C-MPG1-*micro*.

Raman spectrum of C-MPG1-*micro* showed the typical D and G bands at ~1363 and at ~1594 cm^{-1} respectively, indicative of a disordered, graphitic-like material structure (Figure 5.12).[117,122] Significant long-range atomic ordering, corresponding to extended aromatic or graphitic layered systems could not be detected (in agreement with XRD, data not shown) meaning that the obtained carbonaceous material (i.e. C-MPG1-*micro*) possesses a highly disordered carbon wall structure.

5.6 Pore Size Control

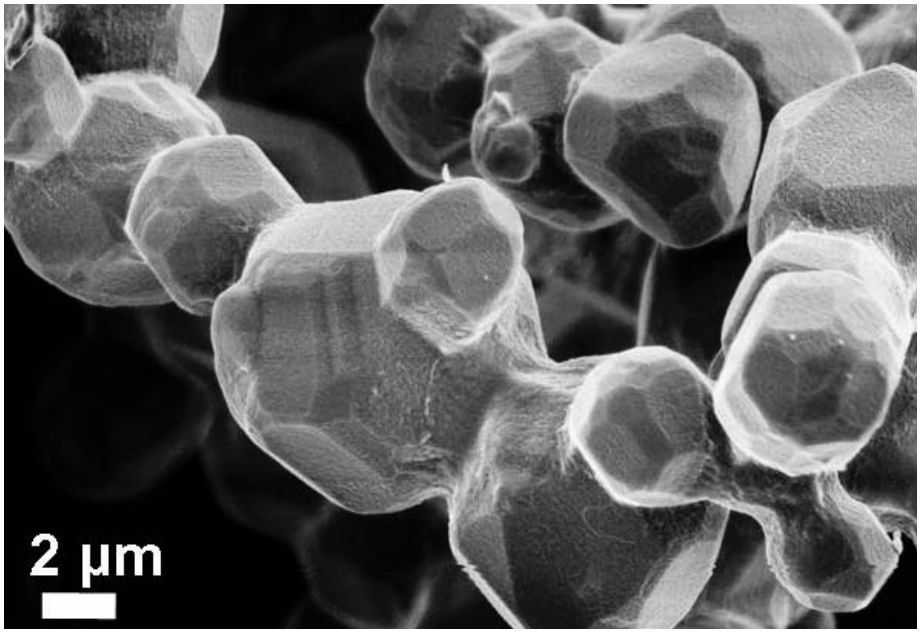

Figure 5.14: SEM micrograph of C-MPG1-*meso* material.

To shift the ordered pore phase dimensions of C-MPG1-*micro* material into the mesoporous domain, the pore swelling agent trimethylbenzene (TMB) [151,152,153,154,155] was added to the F127 / Fru reaction mixture (mol_{F127} : mol_{TMB} = 1 : 0.92; denoted as C-MPG1-*meso*) and material was prepared identically to C-MPG-1-*micro*. Thermal template removal at 550 ^{o}C generated cuboctahedron-like carbonaceous particles, again possessing a faceted edge morphology similar to C-MPG1-*micro* (Figure 5.14). Close examination of the pore structuring via (HR)TEM image analysis indicated the maintenance of the well ordered pore structuring upon addition of the pore swelling agent, with a pore diameter and wall thickness of ~ 5 nm and ~ 10 nm, respectively (Figure 5.15.a and b).

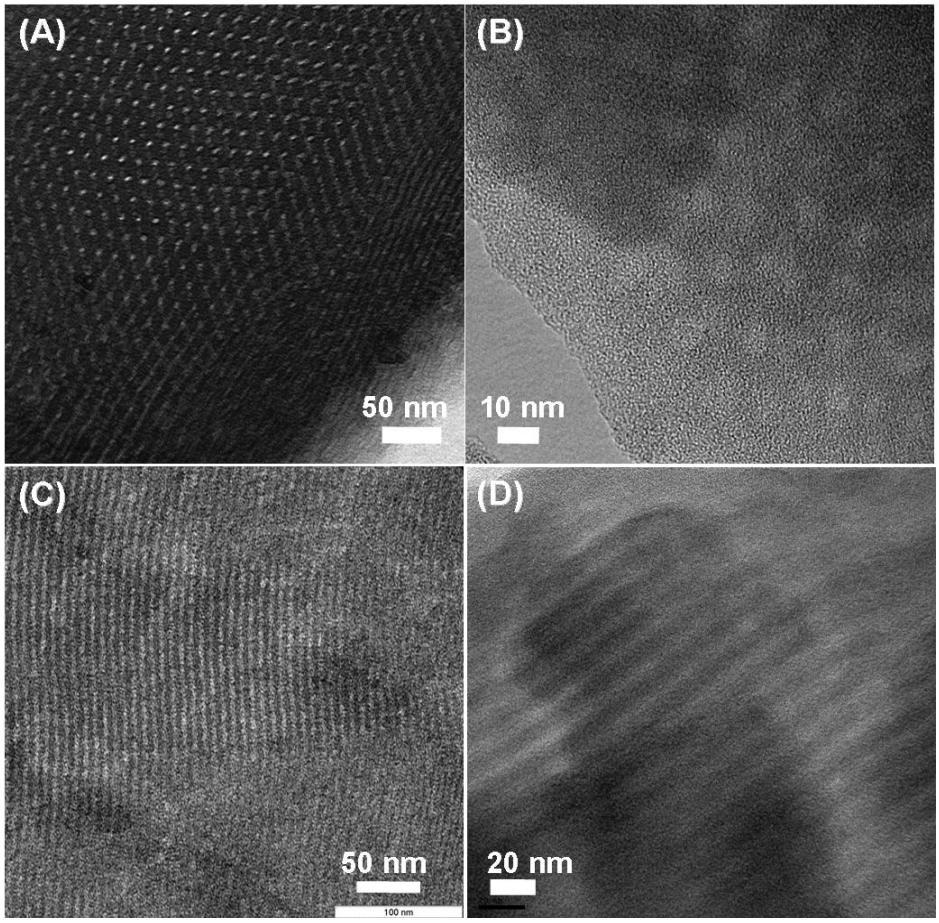

Figure 5.15: (a) and (c) TEM and (b) and (d) HRTEM micrographs of C-MPG1-*meso* material from different directions.

SSAXS analysis of C-MPG1-*meso* presented well resolved peaks at inverse nanometre values of q = 0.47, 0.65, 0.80 and 0.94 nm^{-1} (Figure 5.16). The peak at 0.47 nm^{-1} is accompanied with a shoulder feature indicating some structural heterogeneity (e.g. the presence of a mixed phase) as also demonstrated by the increased polycrystalline nature of this material (2D scattering pattern; Figure 5.16 insert). Indeed, HRTEM image analysis shows the presence of some 1D pore channels demonstrative of a degree of localised structural inhomogeneity (Figure 5.15.c and d). Nevertheless, the SSAXS pattern is indicative of *Im3m* symmetry with a unit cell of 18.9 nm showing the increased regular unit.[149]

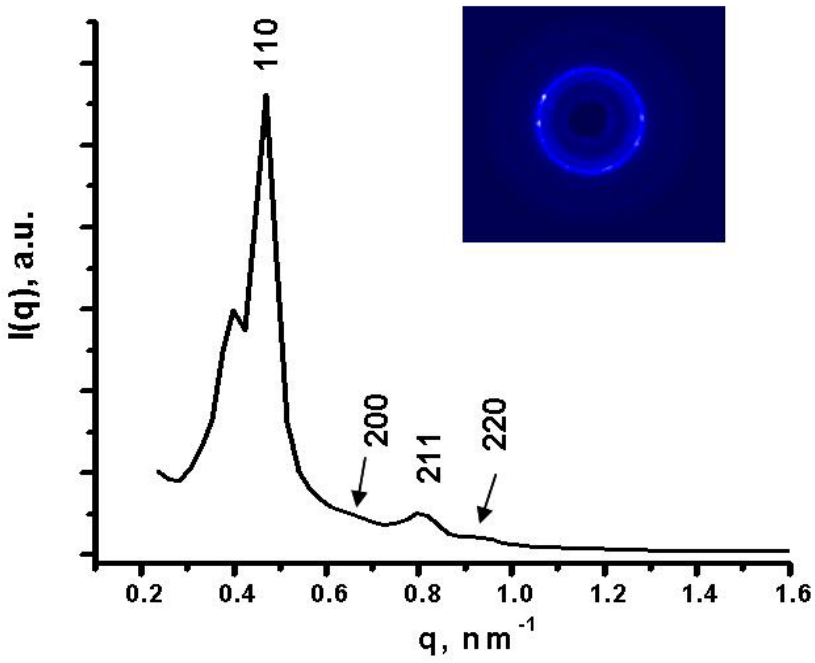

Figure 5.16: SSAXS pattern of C-MPG1-*meso* material (insert; 2D scattering pattern).

The transition from a Type I (e.g. for C-MPG1-*micro*) to a Type IV N_2 sorption profile for C-MPG1-*meso* was observed with associated capillary condensation feature at $P/P_o \sim 0.45$, indicative of a shift in pore structuring into the mesopore domain (Figure 5.17). Consequently, a reduction in surface area ($S_{BET} = 116\ m^2g^{-1}$) and total pore volume resulted ($V_{total} = 0.10\ cm^3g^{-1}$; Table 5.1). The addition of the swelling agent resulted in a bimodal pore size distribution with a new maximum at 4.0 nm in the mesopore domain and a discrete micropore peak at 1.0 nm (e.g. from template removal in mesopore walls). Correspondingly, mesopore volume was enhanced as a proportion of the total pore volume, increasing from ~ 20 % in C-MPG1-*micro*, to ~ 60 % in C-MPG1-*meso*.

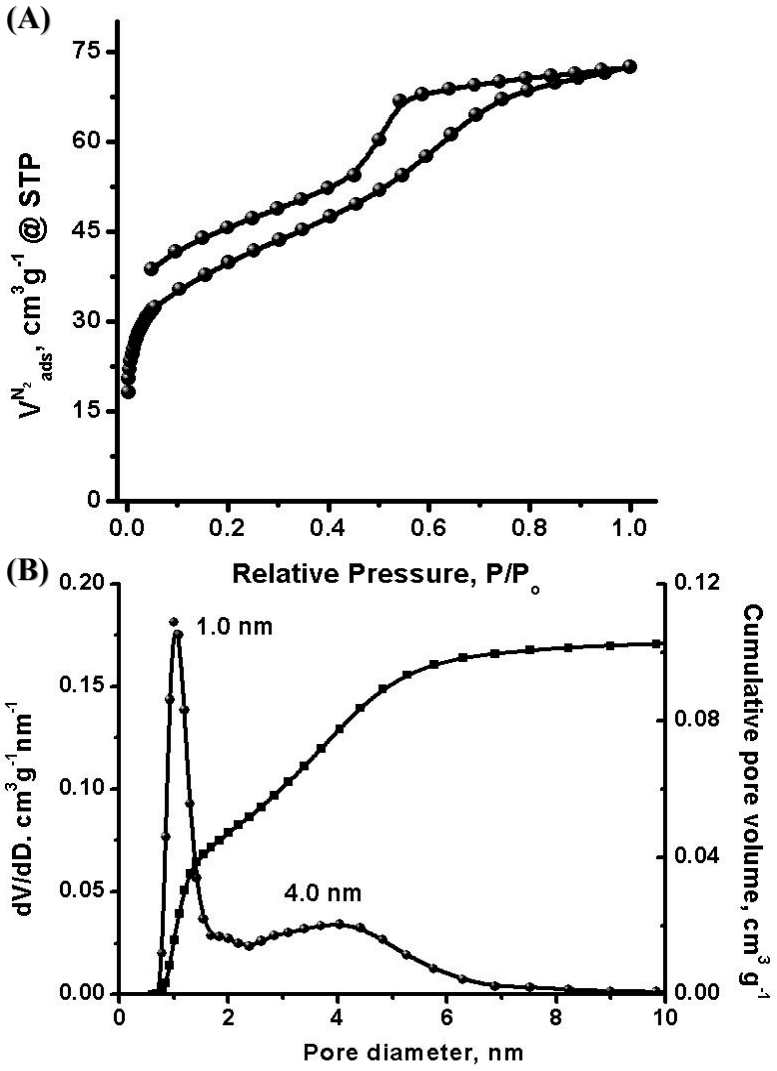

Figure 5.17: (a) N_2 sorption isotherm and (b) QSDFT pore size distribution of C-MPG1-*meso*.

In order to investigate the effect of TMB addition in more detail, the TMB molar ratio relative to the F127 polymer between mol_{F127} : mol_{TMB} = 1 : 0.92 (C-MPG1-*meso*), 1.53, and 2.30. Figure 5.18 (a) - (c) show SAXS patterns of the synthesised materials. Figure 5.18 (a) presents relatively sharp peaks among the three scattering patterns with the overlapping first two peaks located at q = 0.38 and 0.46. When TMB is added at the ratio of 1 ; 1.53, the scattering pattern presents much broader features, but some peaks can be still observed at q = 0.37, 0.45, and 0.52 (Figure 5.18.b). These peaks are located at almost the same positions as the peaks in Figure 5.18 (a), indicating that the size of structural unit remained constant.

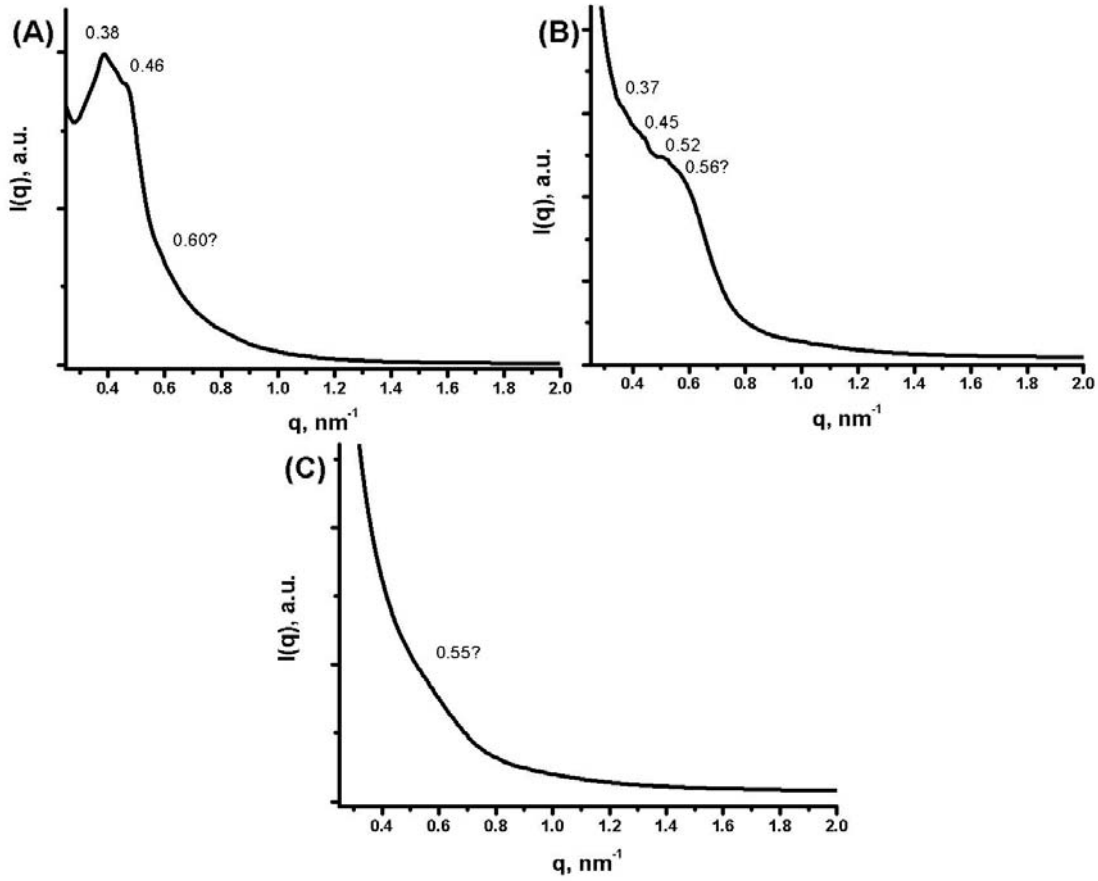

Figure 5.18: SAXS patterns of materials synthesised with the amount of TMB addition (mol_{F127} : mol_{TMB}) of (a) 1 : 0.92, (b) 1 : 1.53, and (c) 1 : 2.30.

When a higher amount of TMB is added (mol_{F127} : mol_{TMB} = 1 : 2.30), almost no peaks are observed indicating the absence of any long range structural regularity (Figure 5.17.c). TEM micrographs of the material synthesised at a F127 : TMB ratio of 1 : 1.53 presented an ordered pore structure of ~ 4 nm in size, whilst pore wall was measured to be ~ 9 nm (Figure 5.19.a and b), thus very similar to the materials synthesised at the F127 : TMB molar ratios of 1 : 0.92 (Figure 5.15.a – d). The increased structural inhomogeneity is considered to be one of the reasons for the observed broad features in the SAXS pattern (see arrows, Figure 5.19.a). Furthermore, the addition of more TMB (F127 : TMB ratio = 1 : 2.30) led to a mixed phase of ordered structure and amorphous structure (Figure 5.19.c – d). Although the ordered area can indeed be partly observed, a non-ordered pore structure with the pore size of ~ 5 nm was more dominant (Figure 5.19.d).

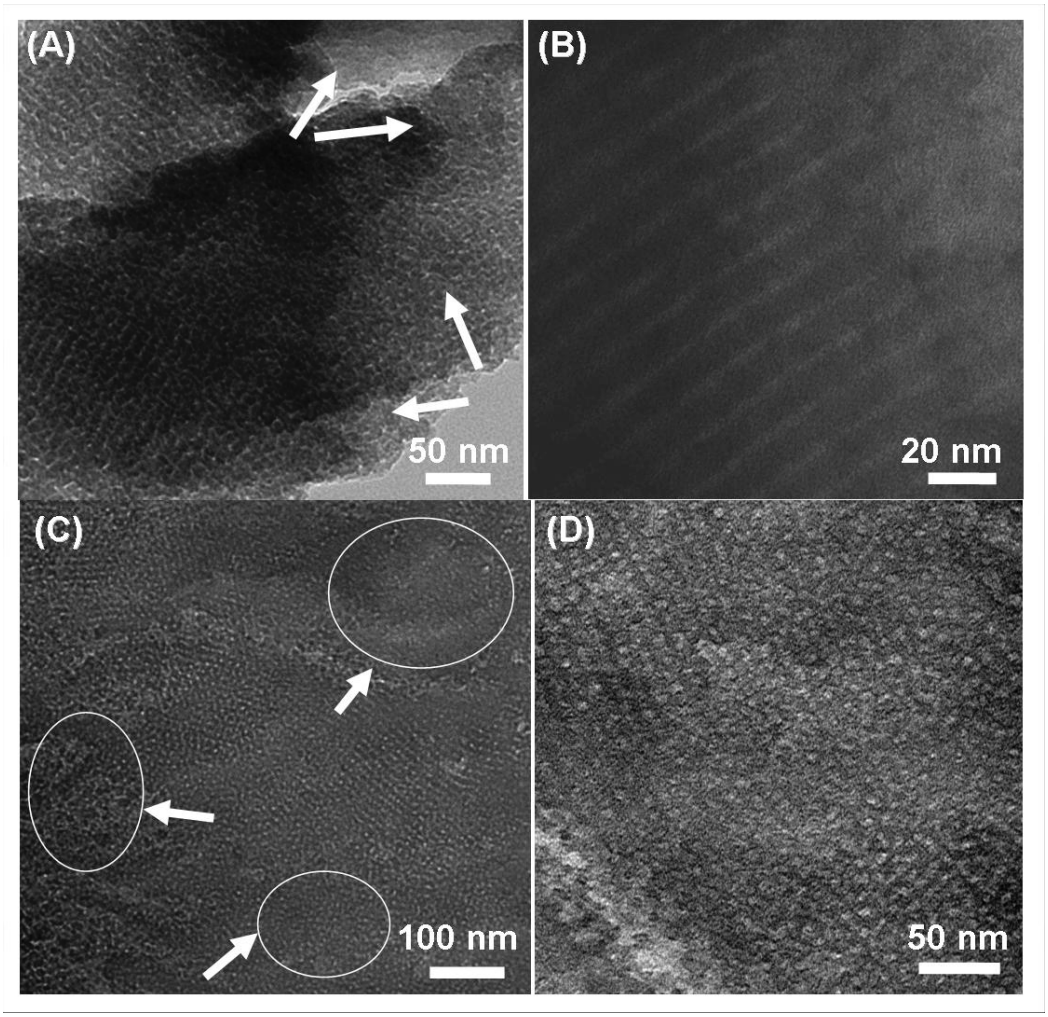

Figure 5.19: TEM micrographs of carbonaceous materials synthesised with the F127 – TMB ratios of (a) and (b) 1 : 1.53, and (c) and (d) 1 : 2.30 (micrographs for the ratio 1 : 0.93 presented in Figure 5.15).

Only negligible differences in pore properties as measured by N_2 sorption between the two materials at F127 : TMB molar ratios of 0.92 and 1.53, were observed (e.g. S_{BET} = 116 $m^2 g^{-1}$, V_{total} = 0.10 $cm^3 g^{-1}$, V_{micro} = 0.04 $cm^3 g^{-1}$ for the former and S_{BET} = 115 $m^2 g^{-1}$, V_{total} = 0.09 $cm^3 g^{-1}$ and V_{micro} = 0.05 $cm^3 g^{-1}$ for the latter, Figure 5.20.a and b). When the relative concentration of TMB was increased still further, the N_2 sorption isotherm of the resulting material presented a profile typical of a non-porous material (S_{BET} = 44 $m^2 g^{-1}$ and V_{total} = 0.05 and V_{micro} = 0 $cm^3 g^{-1}$) showing almost negligible N_2 uptake throughout the whole relative pressure region (Figure 5.20.c).

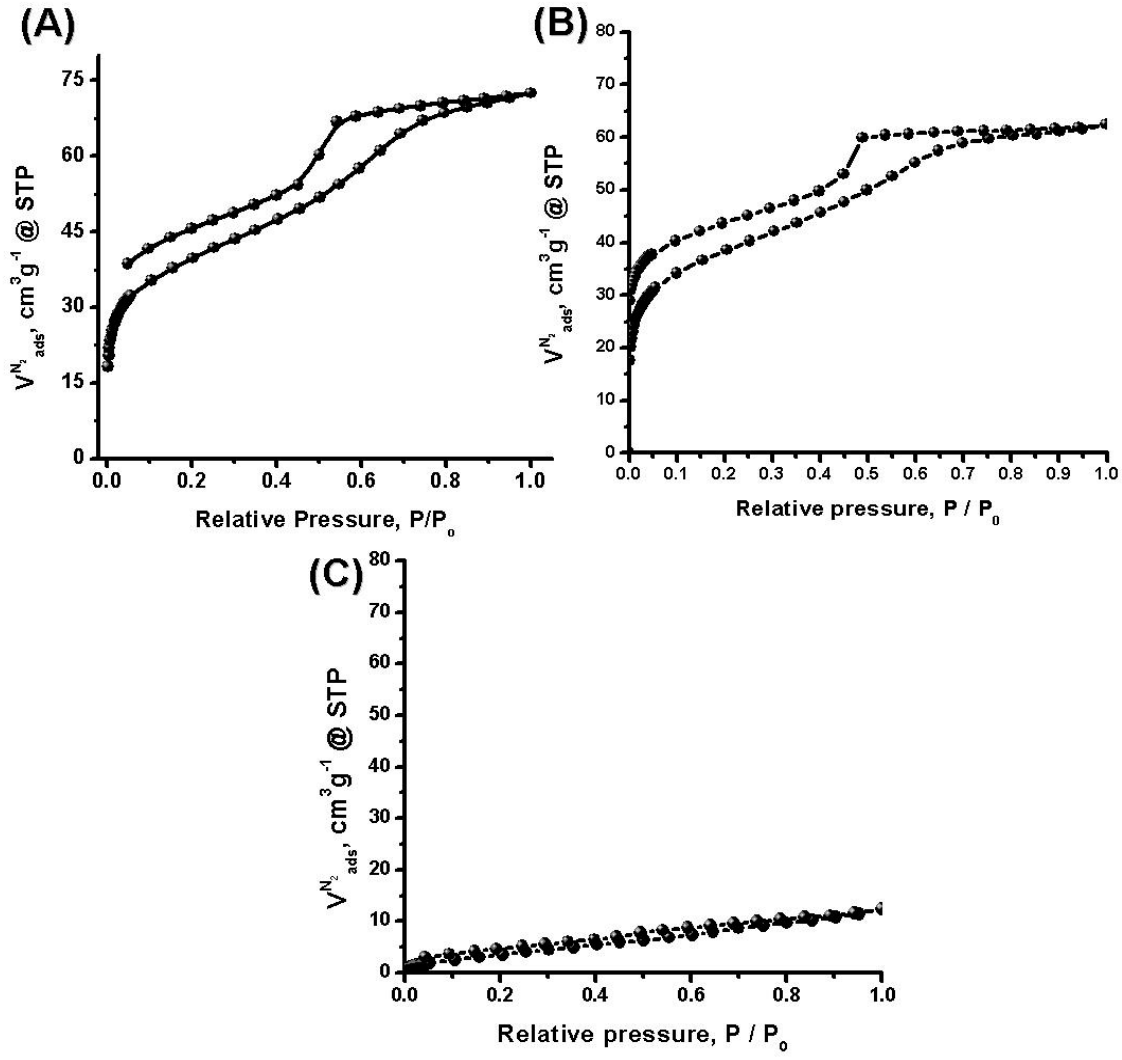

Figure 5.20: N_2 sorption isotherms of materials synthesised with increasing TMB amount (mol_{F127} : mol_{TMB}) of (a) 1 : 0.92, (b) 1 : 1.53, and (c) 1 : 2.30.

As a general rule at low concentrations, the addition of TMB leads to an increase in pore size presumably through swelling of the micellar templating domain. However, when the amount of added TMB becomes higher than the certain amount (i.e. mol_{F127} : mol_{TMB} = 1 : 1.53), a mixed phase occurs, where the stable formation of micelle - Fru composites is disfavoured.[156] Under such synthetic conditions, templating of the micellular phase cannot be achieved yielding non-porous materials.

5.7 Further Optimisation of Synthesis Conditions

One possible drawback of this soft-templating process is the long synthesis time (*ca.* 72 - 120 h). Therefore chemical means to enhance the rate of reaction and material yield were investigated, namely by varying carbon sources, by increasing synthesis temperature or by adding an acid catalyst. Moreover, template removal via solvent extraction was also investigated with the aim of preventing structural shrinkage (by ~30 %) observed to occur upon thermal template removal (e.g. @550 ^{o}C in inert atmosphere); potentially another disadvantage of the presented synthesis system, as this limits access to highly functional low temperature materials.

5.7.1 Effect of Carbon Source

Complementary to the use of Fru, Glu and HMF were respectively used as a carbon source to investigate their effect on pore structuring, whilst the weight amount of added sugar and weight composition of the synthesis mixture were kept constant. Although, unfortunately, determination of pore symmetry was not possible due to the increased broad features of the patterns, it could be observed that the SAXS pattern of the Glu system shows very similar features as compared to the Fru system with the first peak observed at q = ~ 0.50 nm^{-1} (Figure 5.21.a). In contrast, the SAXS peak of the HMF system is slightly shifted to the lower q values (~ 0.48 nm^{-1}) compared to the Fru system (Figure 5.21.b), with both investigated systems generating materials with ordered pore structures and thick pore walls (Figure 5.22.a and b).

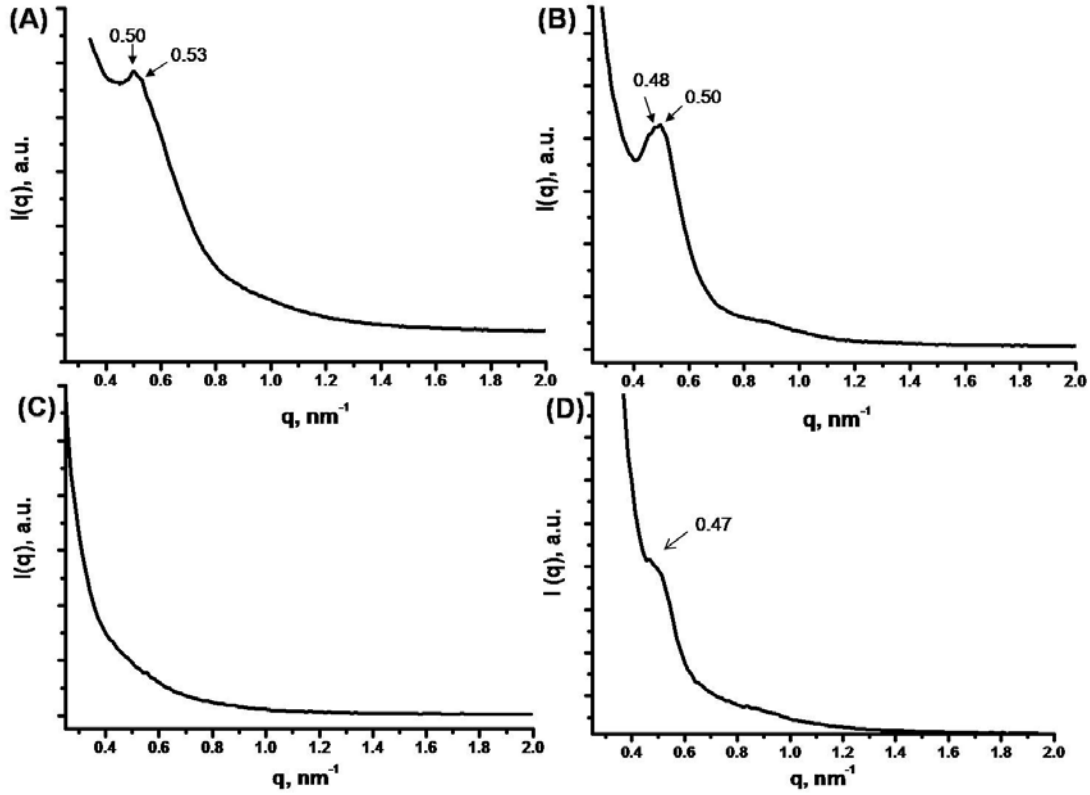

Figure 5.21: SAXS patterns of carbonaceous material synthesised with (a) Glu and (b) HMF as carbon sources at 130 ^{o}C, (c) Fru at 150 ^{o}C and (d) Fru with the addition of H_2SO_4 at 130 ^{o}C.

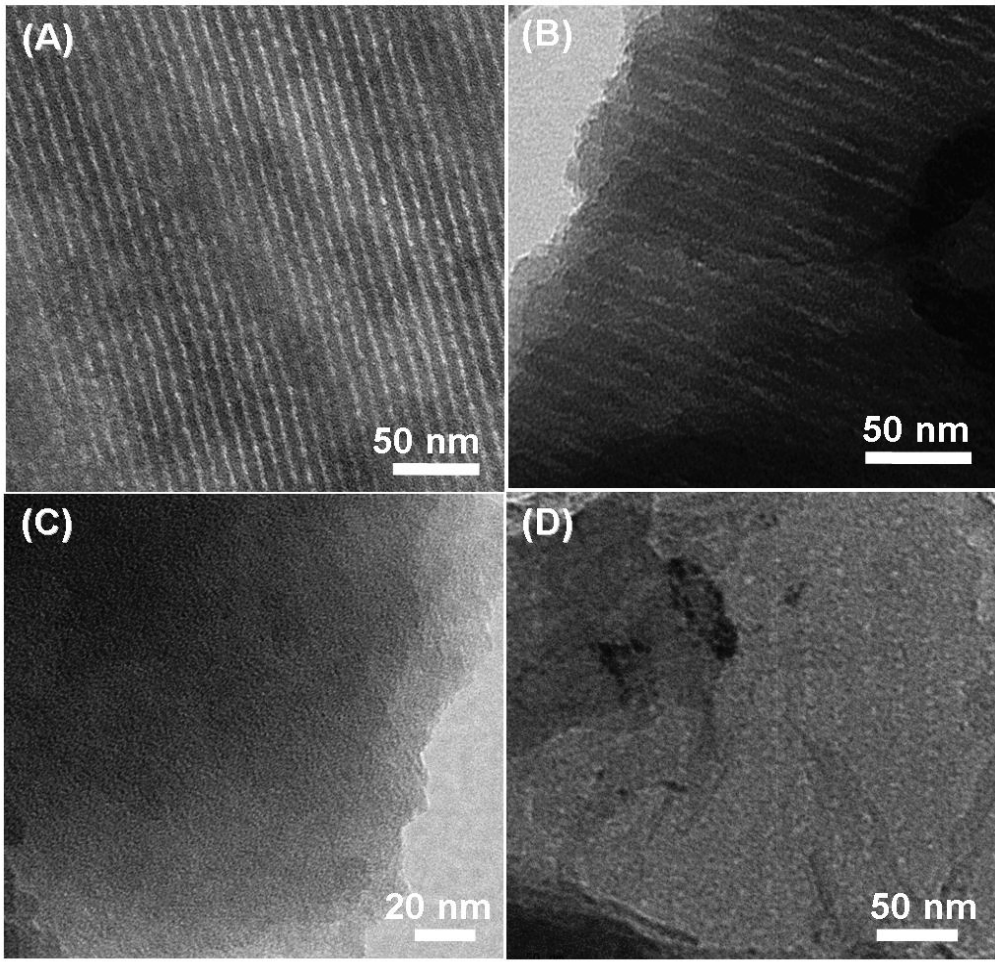

Figure 5.22: TEM micrographs of carbonaceous material synthesised with (a) Glu and (b) HMF as carbon sources at 130 ^{o}C, (c) Fru at 150 ^{o}C and (d) Fru with the addition of H_2SO_4 at 130 ^{o}C.

5.7.2 Synthesis temperature

With an attempt to decrease the reaction time, the material synthesis was performed at 150 ^{o}C. In this case, the block copolymer - carbon composite precipitates were formed after 24 h, which is much shorter than the synthesis at 130 ^{o}C. The respective SAXS pattern of the material synthesised at 150 ^{o}C (after template removal at 550 ^{o}C), indicates no distinct peak indicating the absence of structural order (Figure 5.21. c). TEM micrographs also indicate no long range pore ordering (Figure 5.22.c). The lack of ordered pores was further confirmed from N_2 sorption analysis showing only negligible nitrogen uptake for the whole relative pressure region (see *Appendix* for pore property of this material). It can be considered that the formed micelles are not stable any more at the temperature higher than ~ 150 ^{o}C or that carbonisation already occurs and completes before the stable formation of the micelle – Fru composite.

5.7.3 Addition of acid catalyst

Acids such as H_2SO_4 are well known to be relatively efficient catalysts for the dehydration of saccharides.[58] When acid was added as a catalyst to the starting synthetic mixture (e.g. H_2SO_4), the reaction rate was much faster generating a precipitate after 24 h. Although being relatively broad, the SSAXS pattern shows the first shoulder peak at q = ~ 0.47 nm^{-1} (Figure 5.21.d). This value equates to a d-spacing of 13.4 nm, approximately 1 nm bigger than that of the material synthesised without acid addition (i.e. ~ 12.3 nm). N_2 isotherms of the material shows type I feature with the S_{BET} = 234 $m^2 g^{-1}$ and total and micro pore volume of 0.11 $cm^3 g^{-1}$ and 0.09 $cm^3 g^{-1}$ (Figure 5.23), which are comparable values to that of the material synthesised without acid addition. Importantly, pore size also remained constant (~ 1.1 nm) demonstrating that an increase in d-spacing is the result of increased pore wall thickness, as demonstrated by wall measurements performed on TEM micrograph of the corresponding sample indicating a wall thickness of ~ 20 nm (Figure 5.22.d). Analysis of SEM micrographs also indicates structural inhomogeneity such as formation of film-like structure (Figure 5.24). It is considered that the addition of an acid catalyst leads to the faster carbonisation since it helps the dehydration of the carbohydrate and as a consequence carbon materials with thick walls are obtained.

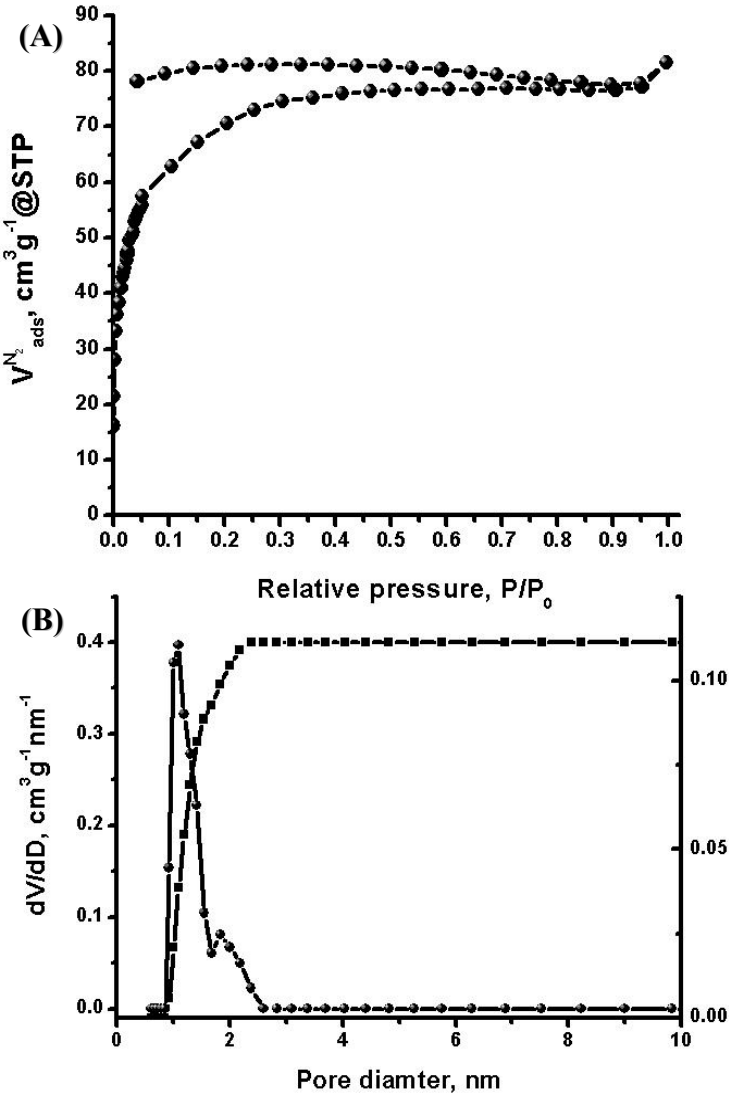

Figure 5.23: (a) Nitrogen sorption isotherms and (b) QSDFT pore size distribution of the material synthesised with the addition of H_2SO_4.

Additional carbonisation outside of the formed block copolymer micelles (e.g. at air-water interface) may lead also to the observed structural inhomogeneity. Addition of acid species can be, therefore, considered a promising method to catalyse the reaction. However, conditions of the reactions still need to be improved to avoid the observed structural inhomogeneity.

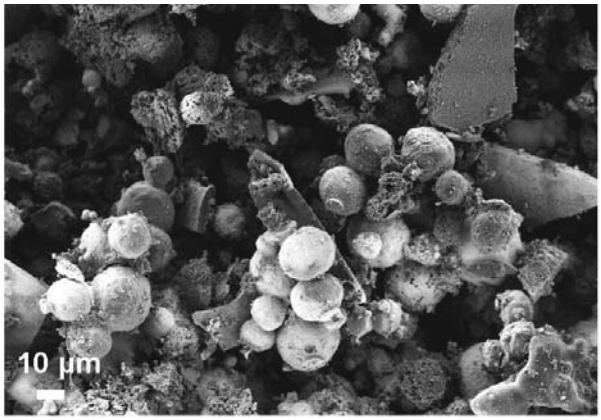

Figure 5.24: SEM micrograph of the material synthesised with the addition of H_2SO_4.

5.7.4 Avoiding pore shrinkage

The structural shrinkage occurring upon template removal through thermolysis was observed to lead to a decrease in pore size and volume. In order to prevent such structural shrinkage and to potentially minimise any contribution to the observed pore dimension shrinkage from the thermal decomposition from the polymer template, an alternative template removal method would be necessary. Our attempt here was to conduct a solvent extraction procedure (i.e. Soxhlet extraction). The F127 – HTC composite material was subjected to the Soxhlet extraction using ethanol for 48 h in an attempt to remove the block copolymer template. However, the material after the Soxhlet extraction did not show any noticeable increase in S_{BET} or nitrogen uptake ability (see *Appendix* for pore property of this material, C-MPG1-Soxhlet). The F127 block copolymer could not be removed as observed from TGA, showing a typical decomposition peak at ~ 400 ^{o}C after the Soxhlet extraction (Figure 5.25). Compared to the total mass loss of the original C-MPG1-*com* material (e.g. ~ 96%), that of the material after Soxhlet process was smaller (e.g. ~ 78%) indicative of removal of HTC decomposition product such as levulinic acid from C-MPG1-*com* by Soxhlet process.[29] SAXS pattern after the Soxhlet process shows the same scattering pattern as the material before the process with the first peak positioning at q= ~ 0.39 (Figure 5.26), indicative of the preservation of the structural regularity of ~ 24 nm. This was also confirmed by the TEM observation showing unchanged pore size and pore wall thickness (Figure 5.27), respectively.

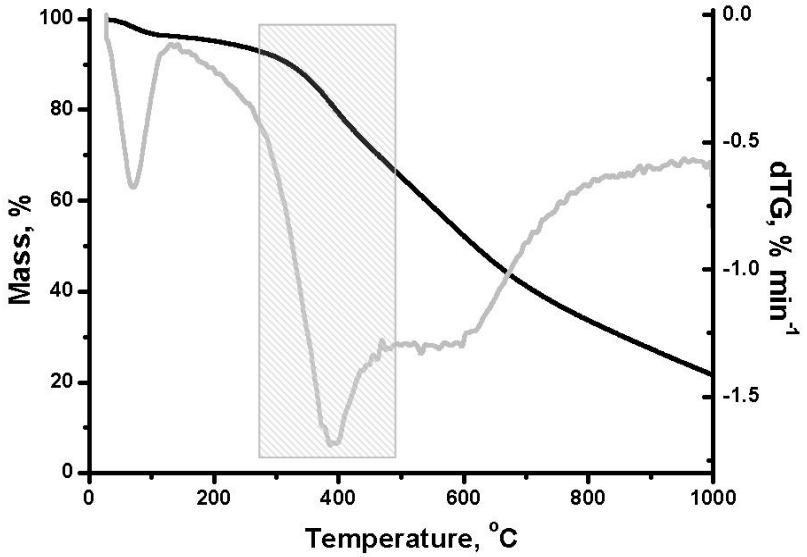

Figure 5.25: TGA (black line) and *d*TG (grey line) curves of C-MPG1-*com* after Soxhlet extraction.

Therefore, the difficulty in the solvent extraction of the F127 template is either due to very limited access of the solvent to the block copolymer species or to the existence of some relatively strong interaction between block copolymer species and the formed carbon. Regarding the former limitation, taking a close look at the TEM micrograph of the composite material (Figure 5.27), one can indeed observe that the pore entrances are blocked by carbon layers, which could then limit an access to the pores. Thus, template removal is currently possible only by thermolysis.

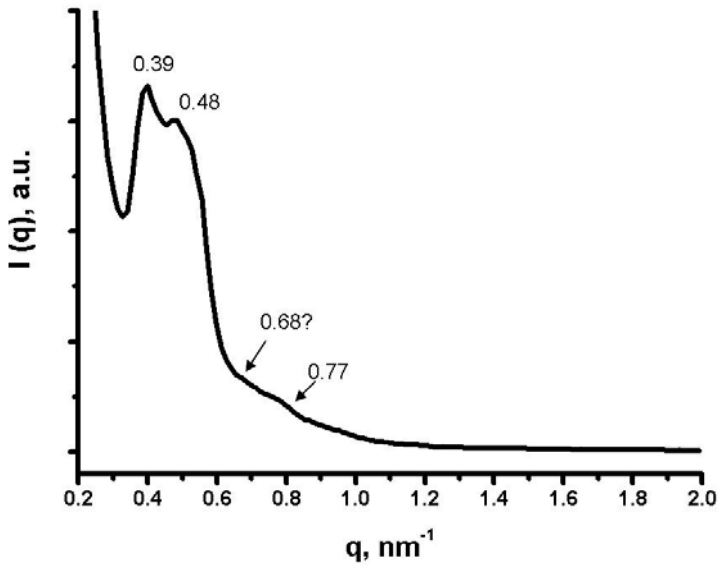

Figure 5.26: SAXS pattern of C-MPG1-*com* after Soxhlet extraction.

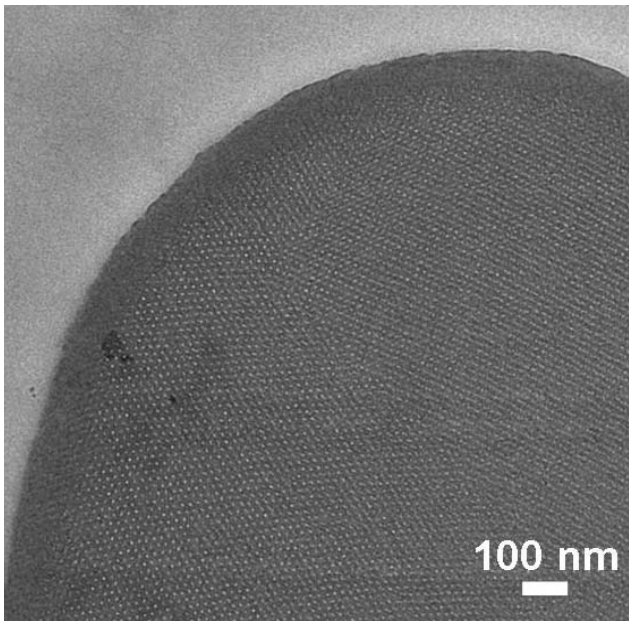

Figure 5.27: TEM micrograph of C-MPG1-*com* after Soxhlet extraction (the image of microtomed material).

5.8 Proposed Mechanism

5.8.1 F127 block copolymer in an aqueous solution

The critical micellisation temperature (CMT) of the F127 block copolymer (2.5 wt%) in H_2O is known to be 27.5 ^oC.[157,158,159] Dynamic light scattering (DLS) measurements revealed that the hydrodynamic diameter of an F127 block copolymer micelle was ~ 26 nm at 27.5 ^oC, continuously decreasing to ~ 10 nm upon heating to 80 ^oC (Figure 5.28, closed circle). Although several different results can be found in the literatures regarding micelle behaviour of the Pluronic-type triblock copolymers as a function of temperature[157,160,161], the observed decrease has been attributed to the combined effect of enhanced dehydration of PEO moiety,[148,160] an increase in aggregation number[157] and a change in solution viscosity.[160,162,163,164] A decrease in solution viscosity could also be induced by disaggregation of formed micelles or to an enhanced degree of dynamic motion of the formed micelles, which, as a result, were detected as micelles with smaller hydrodynamic diameter.

The F127 block copolymer species was revealed to be chemically stable (i.e. not carbonisable) under the presented hydrothermal process conditions. After hydrothermal

processing of an F127 aqueous solution, no precipitates was recovered and the solution was colourless. Comparison between the ATR-FTIR spectra of an F127 block copolymer aqueous solution before and after hydrothermal process did not reveal any significant change in the polymer chemistry indicating the ether functional group (~ 1637 cm^{-1}) and the alkyl chain (3700 - 2800 cm^{-1}) of the polymer were preserved (see Figure 5.29 for the spectrum of the solution after hydrothermal process).[165,166] Therefore, the F127 template is considered to serve only as a structural "template" in the synthesis and not contribute to the overall carbon yield from this hydrothermal process.

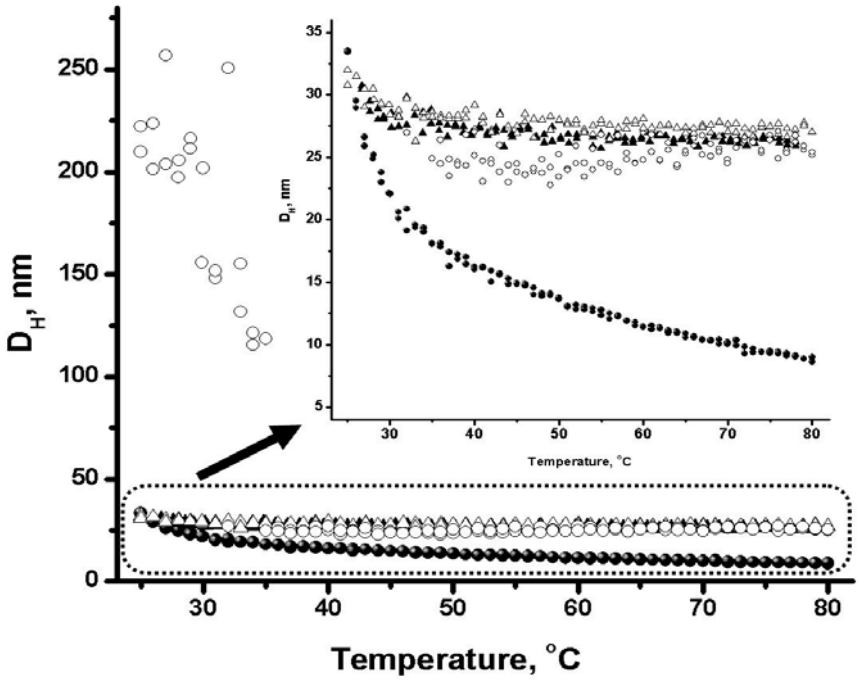

Figure 5.28: Hydrodynamic diameter of the micelles as a function of temperature; (●) pure F127 aqueous solution, (▲) F127 in the presence of fructose, (Δ) F127 in the presence of glucose, and (○) F127 in the presence of HMF.

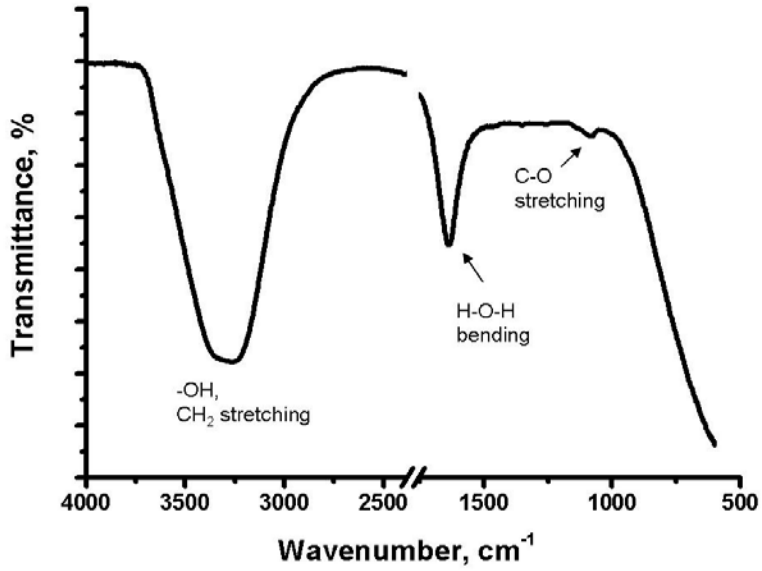

Figure 5.29: ATR-FTIR spectrum of the F127 solution after hydrothermal process.

5.8.2 Formation of micelles in an aqueous carbohydrate solution

In the presence of the carbohydrate species (e.g. Fru, 12 wt% aqueous solution) the dynamic behaviour of the formed micelles was observed to be different from that observed in the absence of carbohydrate species. The hydrodynamic diameter of the micelle in Fru aqueous solution showed only limited decrease between 27.5 ^{o}C and 80 ^{o}C, from 28 nm to 26 nm as measured by DLS. The decrease in diameter of the F127 - Fru solution (Δ -7 %, Scheme 5.1.b) was significantly smaller than that for the pure F127 solution (Δ -62 %, Scheme 5.1.a) and is considered almost negligible. It can be therefore considered that the co-existing sugar species (Fru) hinders the dynamic behaviour of micelles in an aqueous solution upon increasing system temperature. This indicates that some interactions such as hydrogen bonding already exist between the block copolymer micelles and the carbon source (e.g. stabilisation of the formed micelle)[167,168] before the carbonisation reaction begins or that the shrinkage of the micelles is thermodynamically hindered.

Interestingly, F127 in an aqueous Glu solution presented a very similar behaviour during the DLS experiment, undergoing only a marginal decrease in hydrodynamic diameter from 30 nm (@27.5 ^{o}C) to 28 nm (@ 80 ^{o}C) (Figure 5.28, open triangle). In the case of F127 in an aqueous HMF solution, the measured hydrodynamic diameter at 27.5 ^{o}C was significantly larger (> 50 nm) indicative of some significant interaction between

F127 micelles and HMF, possibly resulting in the formation of aggregates. The hydrodynamic diameter, however, was measured as ~ 24 nm once temperature reaches 40 ^{o}C and was observed to increase gradually to 28 nm at 80 ^{o}C (Figure 5.28, open circle). This resulting different tendency could be considered indicative of some different thermodynamic behaviour such as formation of reverse micelles, where the PPO moiety is located on the outer surface showing a more stretched structure at higher temperature (e.g. 80 ^{o}C) interacting with HMF (Scheme 5.1.c-i), or of the increase in aggregation number due to the increased hydrophobicity of the solution as a consequence of HMF addition (Scheme 5.1.c-ii).

5.8.3 Formation of ordered block copolymer – hydrothermal carbon composite

Upon recovering synthetic solution at various stages before the formation of the F127 – carbon composite was complete, the solution was observed to become increasingly carbon-rich (e.g. polyfuran-like) finally to form F127 - carbon composite. The starting solution (Figure 5.30.a) firstly turns light brown after 24 h (Figure 5.30.b) indicative of the formation of HMF. As the reaction proceeds, it turns dark brown and more turbid indicative of polymerisation of the formed HMF towards a polyfuran-like structure (Figure 5.30.c). After 120 h, a solid precipitate is finally observed (Figure 5.30.d).

The formation of solid precipitate is presumably accompanied by some transition from the individual micellular assembly to some higher degree of organisation (e.g. lyotropic phase, 2D hexagonal or 3D cubic), which could be observed in the final materials. Although it is currently not possible to exactly determine at which step this ordered phase (e.g. 3D cubic phase) is formed, from the aforementioned mechanism studies, one can propose one possible formation pathway (Scheme 5.2). As the HTC process proceeds via dehydration / poly-condensation reactions to generate a polyfuran-like network,[29] the organised block copolymer micellular phase is essentially "templated" in the initial steps. F127 micelles are formed in the presence of Fru sugar (Scheme 5.2.a), where Fru is presumably absorbed via hydrogen bonding interactions into the hydrophilic PEO moiety of the F127 and the carbohydrate species slowly transforms into HMF (Scheme 5.2.b). At this stage, the F127 micelles are considered to be normal phase (e.g. hydrophobic core – hydrophilic shell). Here, the possibility of the occurrence

of interaction between PEO moiety and the carbon precursor can be supported also by the fact that only block copolymers with long PEO chains (e.g. F127 ($EO_{106}PO_{70}EO_{106}$), F108 ($EO_{130}PO_{60}EO_{130}$)) led to the formation of the ordered phase (see subchapter 5.3) The formed HMF then starts to form polyfuran – like network and becomes increasingly carbon – rich (Scheme 5.2.c). The resulting polyfuran–like network is comparatively hydrophobic and therefore the possibility of "templating" of a reversed phase through a hydrophobic interaction still cannot be ruled out. As the carbonisation process proceeds, the F127 is considered to change from dispersed individual micelles to 2D or 3D lyotropic phase with higher structural order (e.g. 2D hexagonal or 3D cubic). Finally, the formed F127 – carbon precipitates out of the solution (Scheme 5.2.d). Upon removal of the template by thermal treatment at 550 °C, the resulting pores are smaller than those before template removal due to structural shrinkage (e.g. carbon network condensation) or possible partial carbonisation of the block copolymers.

The growth of carbonaceous crystals is presumably determined by the rate of hexose dehydration (e.g. the generation of HMF) and subsequent polymerisation reactions. Strong interactions between HMF and the PEO segments of the F127 template or between polyfuran-like network and the PPO segments favour this growth of templated near perfect single crystalline carbonaceous structures. A suitably slow HMF feed rate (as determined by dehydration kinetics) leads to a slow growth rate and the formation of these relatively large nanocrystalline structures. Mechanistically, the added TMB is believed to interact with hydrophobic PPO moieties, thus swelling the spatial volume of the hydrophobic region, which in turn results in the observed pore expansion into the mesopore range as observed in more classical inorganic templating examples.

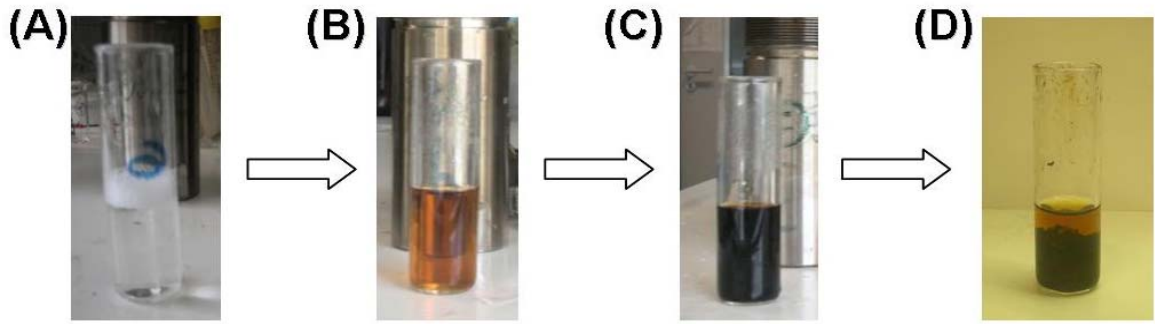

Figure 5.30: Optical micrographs of synthesis mixture; (a) as-prepared F127 – Fru aqueous solution, (b) solution after 24 h, (c) solution after 48 h and (d) yielded precipitates after 120 h.

Importantly, regardless of the carbon source (e.g. Fru, Glu, HMF), the ordered phase was formed. While this represents the versatility of the method, the use of Glu results in a low carbon yield at 130 ^{o}C. The elemental analysis study of the obtained products enabled the calculation of the carbon yields from the different carbon precursors (See *Appendix* for detail). HMF showed the highest yield (70 %) followed by Fru (52 %), while the yield from Glu as a carbon source was much lower (8 %).

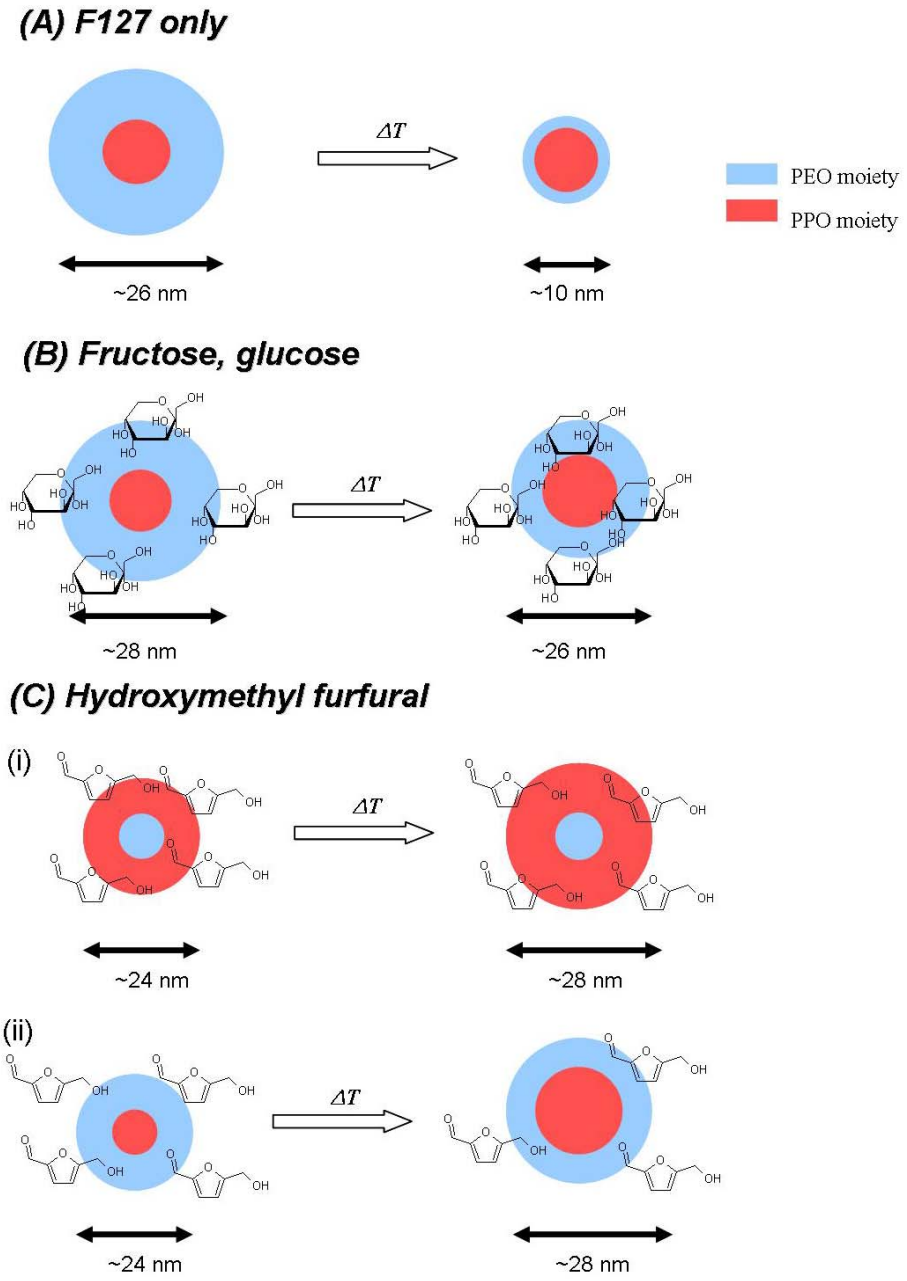

Scheme 5.1: Schematic representation of the proposed behaviour of the template micelle and a carbon source.

Employing a higher reaction temperature (e.g. @ > 150 °C) or acid catalyst indeed increased the carbon yield by enhancing the reaction ratio (subchapter 5.7.3). However, under such conditions, micelles are not stable and the carbonisation speed is so high that the homogeneous nucleation is hindered. Therefore, the selection of Fru as a carbon source plays an essential role in maintaining the relatively high yield, whilst the low synthesis temperature (e.g. 130 °C) allows the formation of the stable template – carbon composite inducing as a result the slow and homogeneous nucleation. Compared to HMF, the use of Fru is more advantageous being by comparison an inexpensive, sustainable carbon source and easier to handle and requires less process steps.

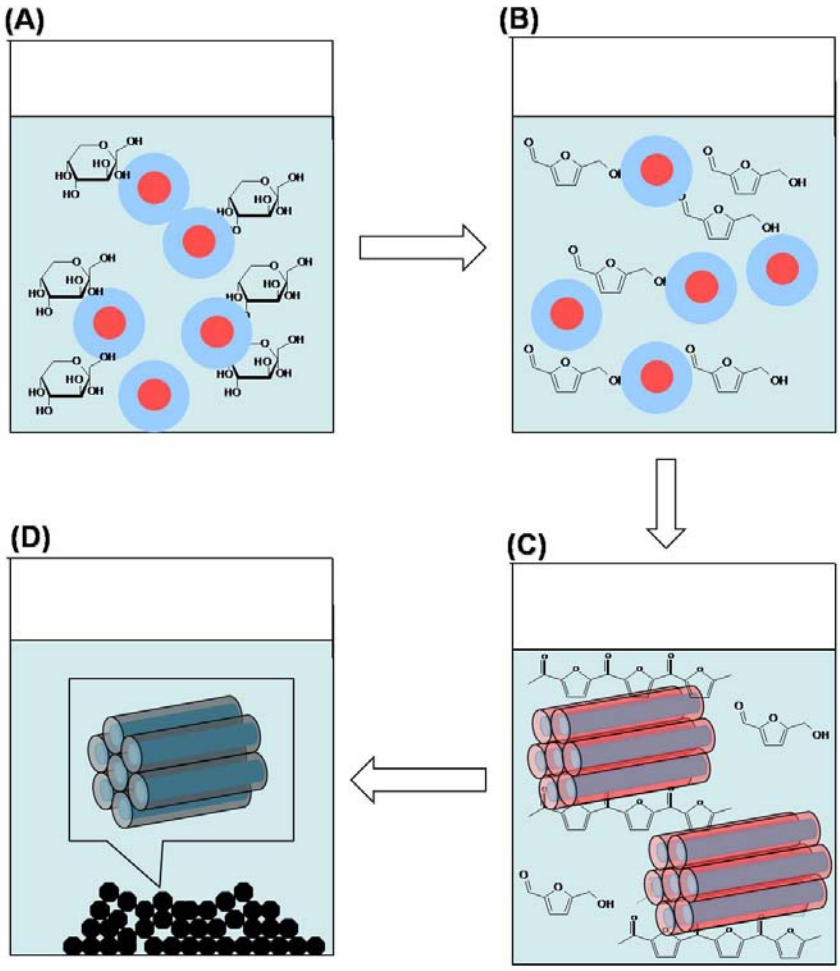

Scheme 5.2: Schematic representation of the formation process of the template – carbon composite.

5.9 Conclusion

A hydrothermal approach for the synthesis of both ordered microporous and mesoporous functional carbonaceous materials was presented. The synthesis was firstly optimised in terms of structural directing agents, composition, carbon precursors, and synthesis temperature. The structure of the obtained materials were characterised by electron microscopy, small angle X-ray scattering and nitrogen sorption porosimetry. The carbon surface and bulk chemistry were analysed by FTIR, ^{13}C solid NMR and FT-Raman spectroscopy. In the optimised system (i.e. F127 block copolymer – Fru system @130 ^{o}C), the material showed cuboctahedron single crystalline-like morphology (particle diameter *ca.* ~ 5 μm) with well ordered pore structuring of a near perfect *Im3m* cubic texture. Nitrogen sorption analysis revealed a type I isotherm (S_{BET} = 257 m^2g^{-1}, V_{micro} / V_{total} = 79 %), whilst QSDFT pore size distribution indicated a discrete peak at a pore diameter of 0.9 nm. The use of simple pore swelling additive (i.e. TMB) directed pore size into the mesopore size domain, with the predominantly pore size diameter shifting to ~ 4 nm (i.e. Type IV isotherm, S_{BET} = 116 m^2g^{-1}, V_{meso} / V_{total} = 60 %). In both cases, materials possessed thick carbon pore walls (7 ~ 10 nm), whilst useful surface functionalities remained (as were characterised by FTIR) after template removal, a product of the comparatively low temperature synthesis and potentially being useful in post-functionalisation strategies.

Based on several comparison studies, a possible formation mechanism of the ordered carbon materials was proposed; as HTC proceeds via the dehydration/ polycondensation reactions, to generate a polyfuran-like network, the organised block copolymer micellular phase is essentially “templated”, whereby in the initial steps Fru is absorbed presumably via hydrogen bonding interactions into the hydrophilic poly(ethylene oxide) moiety of the F127. The resulting polyfuran-like network is comparatively hydrophobic and therefore the possibility of “templating” of a reversed phase through a hydrophobic interaction still cannot be ruled out. Upon removal of the template at 550°C, the resulting pores are smaller than that of before template removal due to structural shrinkage (e.g. carbon network condensation) or possible partial carbonisation of the block copolymers. The pore swelling agent TMB is believed to interact with hydrophobic poly(propylene oxide) moiety, thus swelling the spatial volume of the hydrophobic region, resulting in the observed pore expansion of pore diameter into the mesopore range.

Moreover, it was also revealed that the use of other hexoses or hexose derivatives (e.g. Glu or HMF) also led to ordered materials, whilst the corresponding carbons differ significantly in terms of yields with HMF giving the highest yield of 70 %. The use of an acid catalyst and higher synthesis temperature resulted in a decrease reaction time, but at the expense of the structural order of the final materials.

Ordered porous carbonaceous materials were prepared from renewable inexpensive carbohydrate feedstocks (e.g. D-Fructose, D-Glucose), whilst carbonisation can be performed at relatively low temperatures (~ 130 ^{o}C) to yield materials rich in functional groups with versatile chemistry. Furthermore, compared to the previous hard-templating methods, this soft-templating approach allows direct access to nanoporous materials with ordered pore structures. The preparation of inorganic sacrificial templates and their removal are thus unnecessary.

6. Conclusion and Outlook

In this thesis, the combined use of carbohydrate hydrothermal carbonisation (HTC) and templating strategies was demonstrated to be a useful route to the production of nanostructured carbonaceous materials. Mesoporous carbon spheres were produced via the inverse nanostructure replication of mesoporous silica beads template using a carbohydrate-derived carbon precursor; i.e. 2-furaldehyde (Chapter 4). The presented process consisted of impregnation of the inorganic template with the water-soluble carbon precursor followed by a HTC step (performed at 180 ^{o}C) and subsequent removal of the template via acid etching. The obtained carbonaceous replica possessed the inverse porous structure of the original template, but importantly and contrary to more conventional hard templating routes, presented a functionally rich (oxygenated) surface functionalities (e.g. hydroxy- and carbonyl-containing groups).

The flexibility of this approach allowed control of surface functionality via selection of post-carbonisation temperature (e.g. @350 ^{o}C, 550 ^{o}C, 750 ^{o}C), whilst bulk and surface analysis (e.g. via ^{13}C solid state NMR and FTIR spectroscopy) indicated the transition from more hydrophilic features to increasingly developed aromatic / pseudo-graphitic features with increasing post-carbonisation temperature. However, it should be noted that the complete impregnation of carbon precursors into the inorganic matrixes investigated and the formation of a suitably rigid carbon network still remains a challenge (e.g. as seen in the case of templating of a bimodal silica monolith). Here, additional techniques such as vacuum impregnation or surface modification of the parent inorganic template would play a significant role in improving the degree and quality of

the replication / impregnation. The obtained mesoporous carbonaceous spheres together with bimodal carbonaceous monolith upon achievement of successful templating are promising candidate materials as stationary phases in liquid chromatography, particularly given the ease with which these hydrothermal materials may be successfully chemically modified. The facile and flexible control in surface and bulk chemistry would allow the production of stationary phases with tuneable aromatic properties.

The chemical inertness and high stability over the entire *p*H range (i.e. of high carbonisation temperature materials) would offer a great advantage over the conventional stationary phases (e.g. silica, graphitic carbons). As such the separation of not only non-polar analytes but also polar analytes (e.g. neutral sugars, sugar alcohols) is envisioned using the highly flexible materials.

As an extension of this approach, tubular carbonaceous nanostructures were obtained by templating macroporous alumina membrane. The obtained replicas showed uniform morphology and accessible internal structure via open tube-end apertures (D > *ca.* 125 nm). Again direction of surface functionalities was possible via selection of thermal post-carbonisation temperature as demonstrated particularly by XPS analysis. Again, a reduction in oxygen-containing functionality with increasing carbonisation temperature was observed with associated increase in material aromatic (more classical carbon) character. Gas sorption analysis revealed that the pore properties of these materials could also be simultaneously controlled, showing increasingly microporous features, presumably at the tube wall, as post carbonisation temperature increased. As a proof of principle of the utility of these functional surfaces, the model thermoresponsive polymer poly-N-isopropylacrylamide was successfully covalently attached to the surface of low temperature hydrothermal carbonaceous tubular nanostructures generating a hybrid material possessing stimuli (thermal) responsive behaviour. This feature potentially enables applications in the fields of biotechnology (e.g. enzyme immobilization) and medicine (e.g. as controllable drug microcontainers). This ability to produce nanostructured carbonaceous materials via relatively facile routes, in combination with the simple approach to control bulk and surface chemistry potentially allows for the generation of tailor-made materials from these hard templating approaches. When the carbon network is graphitised, carbonaceous tubular nanostructures would become a very interesting candidate for electrochemical applications such as as anode materials in Li ion batteries or supercapacitors. Here, the developed microporosity and the facile handling

due to tube like morphology would offer the added advantage. For electrochemical applications and, additionally, for possible catalytic applications, incorporation / doping of other chemical species (e.g. N, Li, Pd) would become a very interesting topic.

In chapter 5, the combined HTC / templating approach was extended further and the use of block copolymer templates to direct carbon nanostructural ordering was demonstrated. Here D-Fructose was found to be a useful carbon precursor as it allowed direct access to carbonaceous materials with controlled nanostructures via the formation of block copolymer – carbon ordered phase, as a result of its low hydrothermal degradation temperature (i.e. 130 ^{o}C), allowing access to micellular phases, which under normal HTC conditions (e.g. at 180 ^{o}C) are not available for templating. After the selection of structural directing agents and the optimisation of synthesis compositions, the PEO-PPO-PEO triblock copolymer F127 ($EO_{106}PO_{70}EO_{106}$) – D-Fructose system was extensively studied. Template removal by thermolysis produced carbonaceous materials with an ordered pore structure of *Im3m* cubic symmetry and near perfect (cuboctahedron) single crystalline morphology of ~ 5 μm diameter. The material showed predominantly microporous features as measured by nitrogen sorption (i.e. Type I N_2 sorption isotherm; S_{BET} = 257 $m^2 g^{-1}$; V_{micro} / V_{total} = 79 %) with the corresponding pore size distribution presenting a sharp peak at a diameter of 0.9 nm and a less discrete broader shoulder centred around 2 nm. Whilst both SSAXS and HRTEM indicated the generation of a very thick pore wall feature (e.g. 7 - 10 nm), the wall surface possessed potentially useful functionalities (e.g. phenolic hydroxyls, olefinic / lactone-type C=O and C=C groups). This ordered (micro)pore phase dimensions could be shifted into the mesoporous domain via the simple addition of a pore swelling agent, trimethylbenzene (TMB). Whilst having the same particle morphology as the microporous equivalent, the material possessed the same ordered pore structuring and importantly an increased mesopore character (S_{BET} = 116 $m^2 g^{-1}$; V_{meso} / V_{total} = 70 %) with a bimodal pore size distribution presenting maxima at 4.0 nm (in the mesopore domain) and at 1.0 nm (discrete micropore domains).

This HTC / soft templating study indicated that as HTC proceeds via the dehydration / poly condensation reactions, the organised block copolymer micellular phase is essentially "templated" through certain interactions such as hydrogen bonding between PEO moiety and D-Fructose or hydrophobic – hydrophobic interactions between PPO moiety and the growing polyfuran-like structure (e.g. a reverse micelle replication). Upon removal of the template at 550 °C, the structure encounters shrinkage (e.g. carbon

network condensation) or possible partial carbonisation of the block copolymer leading to microporous features with the thick carbon wall. The added TMB was believed to interact with the hydrophobic PPO moiety, thus swelling the spatial volume of the hydrophobic region, which in turn resulted in the observed pore expansion into the mesopore range.

Further studies on the formation mechanism and the corresponding synthesis optimisation are desirable for this highly interesting soft templating system. For example, in-situ SAXS/SANS studies or ^{13}C-NMR study of the reaction solution could give key information to understand the formation mechanism and ultimately manipulation of the ordered phases. Such information would then open access to materials with enhanced porous features (e.g. increased pore size and pore volume), necessary for successful real world application of these materials. As such these materials are highly versatile potentially finding application in fields such as electrochemistry (e.g. batteries and supercapacitors) or drug delivery systems (e.g. encapsulation of drug molecules). Regularly ordered pore structuring confers particular properties such as controlled linear electronic conduction pathways and fast charge-discharge properties or could facilitate fast encapsulation and release of drug molecules. In future, the materials would find their possible application fields further in optic or electronic devices.

The presented work in this thesis represents important progress in the research field of porous carbonaceous materials providing an access to nanostructured carbonaceous materials with rich surface chemistry via a low-temperature, aqueous-based procedure, using inexpensive, renewable carbon feedstocks (e.g. carbohydrates and their derivatives). Particularly, it presents the first example to demonstrate soft templating under HTC providing direct access to the ordered porous carbonaceous materials. Also, the presented work represents an important contribution to the overall HTC research field, offering developed pore properties to conventionally non-porous HTC - based carbonaceous materials. Additionally, the possibility of controlling material surface functionalities via post-carbonisation temperature selection (as demonstrated for the first time for hydrothermally produced carbons) adds another dimension to these interesting material synthesis approaches. Although further developments related with structural homogeneity and precisely defined porosities are desirable, the presented approaches are intended to open up new pathways to high-value nanostructured carbonaceous materials with versatile applicability.

Appendix

A-1) Synthesis of PO_{40}-*b*-AA_{40} block copolymer

1) α-Butoxy-*ω*-bromo poly(propylene oxide)

10.6 g of commercial poly(propylene oxide) monobutyl ether (Mn ~ 2500) was dried by azeotropic distillation and dissolved under Ar in dry toluene. 1.3 equivalent (eq.) of 2-bromoisobutyryl bromide (0.68 mL) and 1.3 eq. of triethylamine (0.77 mL) were added and mixture was stirred at room temperature for 5 days. The solution was filtered and charcoal was added to the filtrate, stirred for 24 h and filtered. The solvent was removed under reduced pressure to dry and the polymer was re-dissolved in cold water at *p*H=9. The solution was extracted six times with chloroform. The collected organic layer was dried over $MgSO_4$ and filtered followed by the evaporation of the solvent.

2) Poly(propylene oxide)-*b*-poly(*tert*-butyl acrylate)

2 g of the previously synthesised α-Butoxy-ω-bromo poly(propylene oxide) was dissolved in 5 mL of acetone and was bubbled through Ar for 1 h. 1 eq. of N,N,N',N',N-pentamethyl diethylenetriamine (PMDETA, 167 µL) and 1 eq. of CuBr (0.115 g) were added to the solution. 4 mL of freshly distilled *tert*-butyl acrylate was

added and the mixture was heated at 50 °C overnight. The polymer was precipitated in hot water, filtered, re-dissolved in THF and eluted through a silica column followed by the solvent removal under vacuum.

3) Poly(propylene oxide)-*b*-poly(acrylic acid)

4.82 g of the previously synthesised poly(propylene oxide)-*b*-poly(*tert*-butyl acrylate) were dissolved in 5 wt% in dichloromethane. 5 eq. to *tert*-butyl acrylate units of CF_3COOH were added (9.42 mL) and the mixture was stirred at room temperature for 20 h. Purification was achieved by dialysis against chloroform for 4 days with 4 solvent changes. The polymer was recovered by removal of the solvent under reduced pressure.

A-2) Calculation of carbon yield

Carbon yield was calculated using the values in Table App-1 and the following formula.

Table App-1: Weight amount and carbon content of the carbonaceous materials obtained from different carbon precursors.

Carbon source (M_w[a])	Amount of carbon product,[b] g	C content, wt%[c]
Fru (180)	0.38	66
Glu (198)	0.05	64
HMF (126)	0.74	65

a: Molecular weight of each carbon source. b: Weight amount of carbon product obtained after HTC. c: Carbon content measured by elemental

$$\textbf{Carbon yield (\%)} = \frac{W \times C\%}{1.2 \times \frac{M_{WC}}{Mw}} \quad \textbf{(eq. App.1)}$$

Where W is amount of carbon product, C% carbon content measured by elemental analysis, M_{WC} molecular weight of total carbon in each sugar species, and M_w molecular weight of each sugar species.

A-3) List of pore properties of the synthesised carbonaceous materials via soft templating

Table App-2: Pore properties of the synthesised carbonaceous materials *via* soft-templating analysed by N_2 sorption.

Entry	Sample name or discription	[a]S_{BET}, m^2g^{-1}	[b]V_{micro} cm^3g^{-1}	[c]V_{meso} cm^3g^{-1}	[d]V_{total} cm^3g^{-1}	[e]PS, nm
1	C-MPG1-*com*	13	0	0.01	0.01	-
2	C-MPG1-*micro*	257	0.11	0.03	0.14	0.9
3	C-MPG1-*meso* (F127:TMB = 1 : 0.92)	116	0.04	0.06	0.1	1.0, 4.0
4	C-MPG1-Soxhlet	3.4	0	0.01	0.01	-
5	[f]F127:TMB = 1 : 1.53	115	0.05	0.04	0.09	1.0, 3.2
6	[g]F127:TMB = 1 : 2.30	44	0	0.05	0.05	-
7	[h]150 °C	25	0	0.02	0.02	-
8	[i]H_2SO_4	234	0.09	0.02	0.11	1.1

[a] BET surface area, [b] micro- [c] meso- and [d] total pore volume and [e] pore size calculated from QSDFT.
Material synthesised at a F127 : TMB ratio of [f] 1 : 1.53 and [g] 1 : 2.30.
Material synthesised [h] at 150 oC and [i] with the addition of H2SO4.

A-4) Instrumental

[1] Scanning Electron Microscopy (SEM)

SEM was performed using a Gemini Leo-1550 instrument. Before imaging, material was loaded onto carbon tapes and sputtered coated with Au.

[2] (High Resolution) Transmission Electron Microscopy ((HR)TEM)

TEM was performed using an Omega 912 instrument (Carl Zeiss, Oberkochen, Germany). HR-TEM images were acquired using a Topcon EM-002B 120 kV. Samples were prepared by grinding, dispersion in ethanol, and evaporative deposition onto Cu grids (Mesh 400). Particularly, for the observation of thin slices of the materials (e.g. for the observation of micro- and mesopore structures), materials were embedded in an acrylic resin (LR White® resin) by drying the resin at 60 ^{o}C for ~ 3 days. The obtained specimen was trimmed, cut with a diamond cutter and was dispersed on the water surface. Cut specimen was recovered onto cupper grids and dried.

[3] Elemental Microanalysis (EA)

Elemental composition was determined using a Vario El elemental analyzer.

[4] Thermogravimetric Analysis (TGA)

TGA was performed using a NETZSCH TG 209 at a heating rate of 10 K min^{-1} under O_2 and N_2.

[5] Gas Sorption Anlyasis

N_2 and CO_2 sorption analyses were performed using QUADRASORB SI at 77K and an AUTOSORB-1 at 273K (Quantachrome Instrument), respectively. Prior to measurements samples were degassed at 180 ^{o}C for 20 h, except for material obtained directly from hydrothermal carbonisation, which was degassed at 100 ^{o}C. Surface area was determined using the BET method, while textural properties (e.g. pore volume) were calculated using non-linear density functional theory (NLDFT) or quenched solid density functional theory (QSDFT) from adsorption data.

[6] Fourier Transform Infrared Spectroscopy (FTIR)

FTIR was performed with a Varian 600 FTIR Spectrometer with the number of scan times of 256.

[7] Fourier Transform Raman Spectroscopy (FT-Raman)

FT-Raman spectra were acquired using a WiTec Confocal Raman Microscope R-300, frequency doubled green 532 nm Nd/YAG laser with optical resolution diffraction limited to 200 nm laterally and 500 nm vertically and with spectral resolution down to 0.02 wave numbers.

[8] X-ray photoelectron spectroscopy (XPS)

XPS was performed using a Thermo Scientific K-Alpha ESCA instrument equipped with Al Kα monochromatised radiation at a 1486.6 eV X-ray source. Photoelectrons were collected at a take off angle of 90^{o} relative to the sample surface. The measurement was done in a constant analysed energy mode (CAE) with a 100 eV pass energy for survey spectra and a 20 eV pass energy for high resolution spectra. Charge referencing was carried out by setting the lower binding energy of C1s peaks at 285.0 eV. The atomic percentage was determined from the XPS peak area using the Shirley background subtraction technique and the Scofield sensitivity factors.

[9] Synchrotron Small Angle X-ray Scattering (SSAXS)

SSAXS measurements were performed at the μ-Spot beamline of the Synchrotron facility Bessy II (Helmholzzentrum für Materialien und Energie) equipped with a Mar Mosaic 225 detector (MarUSA, Evanston, USA). Radiation energy was 15 keV and a pinhole diameter was 10 μm.

[10] Small Angle X-ray Scattering (SAXS)

SAXS measurements were performed using a CuKα rotating anode device (Nonius) with 3-pinhole collimation, equipped with a MarCCD detector.

[11] Solid-state ^{13}C Cross-Polarisation Magic Angle Spinning (CPMAS) nuclear magnetic resonance (NMR)

Solid-state ^{13}C CPMAS NMR was performed on a Bruker Avance 300 MHz (7T) spectrometer using the 4 mm zirconia rotors as sample holders spinning at MAS rate

νMAS= 14 kHz. The chemical shift reference was tetreamethylsilane (TMS; d = 0 ppm). Proton-to-carbon CP MAS was used to enhance carbon sensitivity: recycle delay for all CP experiments was 3s and TPPM decoupling is applied during signal acquisition. Cross-polarisation transfers were performed under adiabatic tangential ramps to enhance the signal with respect to other known methods and the CP time tCP = 1 ms was found to be a good compromise in order to have a good overview of all carbon species. The number of transients was 2400.

[12] Dynamic Light Scattering (DLS)

DLS experiment was performed using ALV-7004 Multiple tau digital correlator equipped with CGS-3 Compact Goniometer system, 22 mW He-Ne laser (wavelength λ = 632.8 nm) and pair of avalanche photodiodes operated in a pseudo-cross-correlation mode. The measurement was conducted at an angle of 90 ^{o}, with the heating program of 1 ^{o}C of a heating step and 600 s of waiting time.

[13] Gel Permeation Chromatography (GPC)

GPC measurements were performed to determine molecular weights and molecular weight distributions at 25 ^{o}C in THF (flow rate 1 ml/min), using four 5 μ-SDV columns (one guard column and three columns at 4 X 103, 3 X 105, 2 X 106 Angstroms). The detection was carried out with a RI (DN-1000, WGE Dr. Bures) and a UV/VIS detector (UV 2000; 260 nm). For calibration, linear polystyrene standards (PSS, Germany) were used.

[14] Turbidimetric Analysis

Turbidimetric analysis was performed using a turbidimetric photometer (TP1, Tepper Analytik). A 0.3 wt % aqueous solution of PNiPAAm-modified tublar carbons were sonicated for 30 min prior to analysis. Light transmission experiments were performed in the temperature range of 10-50 ^{o}C at a rate of 1 ^{o}C min^{-1}.

A-5) List of main abbreviations and symbols

Abbreviations

AAO	Anodic alumina membrane
AIBN	2,2-azobisisobutyronitrile
APS	(3-Aminopropyl) triethoxysilane
BET	Brunauer-Emmett-Teller
BJH	Barret-Joyner-Halenda
CMT	Critical micellisation temperature
CP MAS	Cross polarization magic-angle-spinning
(NL / QS) DFT	(Non-local / Quenched-state) Density functional theory
DLS	Dynamic light scattering
EA	Elemental analysis
Fru	D-Fructose
FTIR	Fourier transform infrared spectroscopy
GAI	Generalised adsorption isotherm
Glu	D-Glucose
GPC	Gel permeation chromatography
HMF	5-hydroxymethyl-furfural
HTC	Hydrothermal carbonisation
LCST	Lower critical solution temperature
NMR	Nuclear magnetic resonance
PEO	Poly(ethylene oxide)
PNiPAAM	Poly(N-isopropylacrylamide)
PPO	Poly(propylene oxide)
RAFT	Reversible addition fragmentation chain transfer
SAXS	Small angle X-ray scattering
SDS	Sodium dodecyl sulfate
SEM	Scanning electron microscopy
(HR)TEM	(High resolution) Transmission electron microscopy
TGA	Thermogravimetric Analysis
TMB	Trimethylbenzene
XPS	X-ray photoelectron spectroscopy

Symbols

d	Distance
λ	Wavelength
n	Refractive index
θ	Bragg angle (subchapter 3.2) / Contact angle (subchapter 3.3)
$\vec{q}$	Scattering vector
$I(\vec{q})$	Scattering intensity
$P(\vec{q})$	Form factor
$S(\vec{q})$	Structure factor
ρ	Electron density
V	Volume
a	Lattice parameter
h,k	Miller index
p/p_0	Relative pressure
n_m	Monolayer capacity
$a_{(BET)}, a_{(t)}, S_{BET}$	Specific surface area
σ	average area occupied by one molecule (subchapter 3.3.1) / surface tension (subchapter 3.3.2)
C	BET constant
L	Avogadro constant
t	Standard multilayer thickness
V_{ads}^{STP}	Volume of gas adsorbed at standard temperature and pressure
r	Radius
R	Gas constant
T	Temperature
ν	Wavenumber
m	Mass
h	Planck constant
V_{total}	Total pore volume
V_{meso}	Mesopore volume
V_{micro}	Micropore volume
σ	Chemical shift

A-6) Acknowledgement

I would like to thank Professor Dr. Markus Antonietti for giving me the opportunity to pursue Ph.D. degree at the Max-Planck-Institute of Colloids and Interfaces. His idea, word fascinated me every time at the discussions and even some laboratory work we did together. The horizon of my scientific world has been definitely widened by his supervision.

I would like to sincerely acknowledge Dr. Maria-Magdalena Titirici for offering me the Ph.D. position in her group and for her supervision for the entire two years and nine months. Without her leadership, guidance and support, I would not have been able to finish writing my Ph.D. thesis. I very much appreciate her for her neverending trust in my scientific work.

Dr. Robin Jeremy White is sincerely acknowledged for tremendous amount of discussions and suggestions and comments on daily work, papers and my thesis and for the correction of the thesis. During the entire Ph.D. period he helped me develop both basic and advanced scientific skills and knowledge. I very much appreciate being always open to any questions, also being strict (!) but very supportive.

Special thanks go to the technicians; Frau Regina Roethe (vor allem!! Du warst ja immer um mich besorgt…), Frau Silvia Pirok (EA), Frau Irina Shekova (TGA), Frau Ingrid Zenke (SAXS), Frau Heiko Jung (EM), and Frau Rona Pitschke (EM). I would especially appreciate Frau Pitschke for her enduring and dedicated TEM work and for being enthusiastic about observing my carbon samples.

I would also like to thank Dr. Yoshizawa for HRTEM observation, Dr. Serra for XPS measurement, Dr. Wagermeier, Dr. Aichmayer Dr. Li and Ms. Schenk for the support at SSAXS measurements, Dr. Klaus Tauer and Dr. Peter Cernoch for DLS measurements and many discussions, Dr. Jens Weber for his support in sorption analyses and SAXS analyses and discussions, and Ms. Clara Valverde for block copolymer synthesis and DLS measurements.

DAAD is thanked for the financial support. AIST is sincerely acknowledged for the very kind understanding of my research plan in Germany and continuous support. I would also like to thank Prof. Dr. Smarsly for accepting to be a “Gutachter” for the DAAD scholarship application.

I would also like to thank Ms. Tatjana Wonneberg (Japanisch-Deutsches Zentrum Berlin) and Prof. Dr. Arne Thomas (TU-Berlin) for providing me with the first contact to the MPI, which gave me the idea of pursuing Ph.D. study at the MPI.

I can never forget to thank all my colleagues, who worked together and shared very precious time here in Golm; Irene, Daniel, Alex. We always supported with each other and I will never forget all the events we went through and overcome together during our Ph.D.

Rezan, Farnoosh, Li, Niki, Jelena, Jerome, Fernando, George, Camillo, Tim, Steffi, Marina, Maria-Luz, Sang-min, Linghui, Jens P., Johannes S., Nicola, Christine, Christina, Florian, David, Alfonso, Zoe, Emi, Ina, Bettina, Antje, Jekaterina, Sujeong, Wen, Yuan, Yong, Ruben, Martin H., Thorsten, Ronald (UP), Xailai (UP), Dr. Xinchen Wang, and Dr. Takashi N., thank you for your support and being awesome colleagues. I would also like to thank new comers, Nico, Hiro, Filip, Steffan, Nina, Constanze for bringing fresh atmosphere to the workplace. Outside of workplace, I would like to thank Karin, Hans and Iris for all your help with my life in Germany.

Finally, I would like to thank my parents and my sister for their understanding and support both in bad times and good times. I appreciate that you are always proud of me. I am proud of you, too. 「親思う心に勝る親心」。

Ein besonderes Dankeschön and appreciation go to Johannes Früh, who is always with me going through both good times and bad times with me. Bald bist du daran!

Thank you, danke schön and ありがとう。

A-7) References

[1] Kondo, S.; Ishikawa, T.; Abe, I., *Science of Adsorption*. Maruzen: Tokyo, **2001**.

[2] Eltekova, N. A.; Berek, D; Novak, I; Belliardo, F. *Carbon* **2000**, *38*, 373.

[3] Steel, K.M; Koros, W.J. *Carbon* **2003**, *41*, 253.

[4] Demir-Cakan, R; Makowski, P; Antonietti, M; Goettmann, F; Titirici, M-M. *Chem. Commun.* **2008**, 999.

[5] Serp, P.; Figueiredo, J. L. *Carbon Materials for Catalysis.* A John Wiley & Sons, Inc.: the United States of America, **2009**.

[6] Demir-Cakan, R.; Titirici, M-M.; Antonietti M.; Cui G.; Maier, J.; Hu, Y-S. *Chem. Commun.* **2008**, 3759.

[7] Paraknowitsch, J-P.; Antonietti, M.; Thomas, A. *Chem. Mater.* **2009**, *21*, 1170.

[8] Knox, J-H.; Kaur, B.; Millward, G.R. *J. Chromatogr.* **1986**, 352, 3.

[9] Hanai, T; *J Chromatogr. A* **2003**, *989*, 183.

[10] Budarin, V.; Clark, J-H.; Hardy, J.J.E.; Luque, R.; Milkowski, K.; Tavener, S.J.; Wilson, A.J. *Chem Commun*. **2006**, *45*, 3782.

[11] Pandolfo, A. G.; Hollenkamp, A. F. *J. Power Sources* **2006,** *157*, 11.

[12] Pekala, R. W.; *J. Mater. Sci.* **1989,** *24*, 3221.

[13]http://www.panasonic.com/industrial/batteries-oem/oem/primary-coin-cylindrical/index.aspx

[14] http://www.engr.wisc.edu/news/archive/2009/Sep17.html

[15] De la Zerda, A.; Gambhir, S.S. *Nat. Nanotechnol.* **2007**, *2*, 745.

[16] Kroto, H.W.; Heath, J.R.; Brien, S.C.; Curl, R.F.; Smalley, R.E. *Nature*, **1985**, *318*, 162.

[17] Iijima, S. *Nature* **1991,** *354*, 56.

[18] Endo, M. *Phys. Chem. Solids*, **1993**, *54*, 1841.

[19] Geim, A.K.; Novoselov, K.S. *Nat. Mater.* **2007**, *6*, 183.

[20] M. Ströck; GNU Free Documentation Licence **2006**.

[21] Guo, T.; Nikolaev, P.; Rinzler, A.G.; Tomanek, D.; Colbert, D.T.; Smalley, R.E. *J. Phys. Chem.* **1995**, *99*, 10694.

[22] Thess, A.; Lee. R.; Nikolaev, P.; Dai, H.J.; Petit, P.; Robert, J.; Xu C-H.; Lee, Y.H.; Kim, S.G.; Rinzler, A.G.; Colbert, D.T.; Scuseria, G.E.; Tomanek, D.; Fischer, J.E.; Smalley, R.E. *Science*, **1996**, *273*, 483.

[23] Eftekhari, A.; Jafarkhani, P.; Moztarzadeh, F. *Carbon*, **2006**, *44*, 1343.

[24] Marsh, H. *Introduction to Carbon Science*, **1989**, Butterworth-Heinemann, UK.

[25] Bergius, F. *Naturwissenschaften* **1928,** *16*, 1.

[26] Cui, X.; Antonietti, M.; Yu, S-H. *Small* **2006**, *2*, 756.

[27] Wang, Q.; Li, H.; Chen, L.; Huang, X. *Carbon* **2001**, *39*, 2211.

[28] Sun, X.; Li, Y. *Angew. Chem. Int. Ed.* **2004**, *43*, 597.

[29] Baccile, N.; Antonietti, M.; Titirici, M-M. *Green Chem.* **2008**, *10*, 1204.

[30] Titirici, M-M.; Antonietti, M. *Chem Soc Rev*, **2010**, *39*, 103.

[31] Baccile, N.; Laurent, G.; Babonneau, F.; Fayon, F.; Titirici, M-M.; Antonietti, M. *J. Phys. Chem. C* **2009**, *113*, 9644.

[32] Schueth, F. *Angew. Chem. Int. Ed.* **2003,** *42*, 3604.

[33] Ryoo, R.; Joo, S-H.; Jun, S. *J. Phys. Chem. B* **1999,** *103*, 7743.

[34] Ryoo, R.; Joo, S-H.; Kruk, M.; Jaroniec, M. *Adv. Mater.* **2001**, *13*, 677.

[35] Liang, C.; Hong, K.; Guiochon, G.A.; Mays, J.W.; Dai, S. *Angew. Chem. Int. Ed.* **2004,** *43*, 5785.

[36] Liang, C.; Dai, S. *J. Am. Chem. Soc.* **2006,** *128*, 5316.

[37] Zhang, F.; Meng, Y.; Gu, D.; Yan, Y.; Yu, C.; Tu, B.; Zhao, D. *J. Am. Chem. Soc.* **2005,** *127*, 13508.

[38] Huang, Y.; Cai, H.Q.; Yu, T.; Zhang, F.Q.; Zhang, F.; Meng, Y.; Gu, D.; Wan, Y.; Sun, X.L.; Tu, B.; Zhao, D. *Angew. Chem. Int. Ed.* **2007,** *46*, 1089.

[39] Meng, Y.; Gu, D.; Zhang, F.; Shi, Y.; Yang, H.; Li, Z.; Yu, C.; Tu, B.; Zhao, D. *Angew. Chem. Int. Ed.* **2005,** *44*, 7053.

[40] Meng, Y.; Gu, D.; Zhang, F.; Shi, Y.; Cheng, L.; Feng, D.; Wu, Z.; Chen, Z; Wan, Y.; Stein, A.; Zhao, D. *Chem. Mater.* **2006,** *18*, 4447.

[41] McEnaney, B.; Burchell, T. D. *Carbon Materials for Advanced Technologies*, Pergamon: **1999**.

[42] Inagaki, M.; Radovic, L. R. *Carbon* **2002,** *40*, 2279.

[43] Peterson, A.A.; Vogel, F.; Rachance, R.P.; Froeling, M.; Antal, M.J.; Jr., Tester, J.W. *Energy. Environ. Sci.* **2008**, *1*, 32.

[44] Berl, E.; Schmidt, A.; Koch, H., *Angew. Chemie* **1932,** *45*, 517.

[45] Schuhmacher, J. P.; Huntjens, F. J.; Vankrevelen, D. W., *Fuel* **1960,** *39*, 223.

[46] Yu, S.H.; Cui, X.J.; Li, L.L.; Li, K.; Yu, B.; Antonietti, M.; Colfen, H. *Adv. Mater.* **2004,** *16*, 1636.

[47] Luo, L.B.; Yu, S.H.; Qian, H.S.; Gong, J.Y., *Chem. Commun.* **2006,** *7*, 793.

[48] Demir-Cakan, R.; Baccile, N.; Antonietti, M.; Titirici, M-M. *Chem. Mater.* **2009,** *21*, 484.

[49] Demir-Cakan, R.; Makowski, P.; Antonietti, M.; Goettmann, F.; Titirici, M-M. *Catal. Today* **2010***, 150*, 115.

[50] Aida, T.M.; Tajima, K.; Watanabe, M.; Saito, Y.; Kuroda, K.; Nonaka, T.; Hattori, H.; Smith Jr. R.L.; Arai, K. *J. Supercrit. Fluids* **2007**, *42*, 110

[51] Baiccile, N.; Laurent, G.; Babonneau, F.; Titirici, M-M.; Antonietti, M. *Carbon* **2008**, *46*, 1393.

[52] Lozano-Castello, D.; Cazorla-Amoros, D.; Linares-Solano, A.; Shiraishi, S.; Kurihara, H.; Oya, A. *Carbon* **2003,** *41*, 1765.

[53] Pekala, R. W. *J. Mater. Sci.* **1989,** *24*, 3221.

[54] Pekala, R. W.; Alviso, C. T.; Kong, F. M.; Hulsey, S. S. *J. Non-Cryst. Solids* **1992,** *145*, 90.

[55] Moreno-Castilla, C.; Maldonado-Hodar, F. J. *Carbon* **2005,** *43*, 455.

[56] White, R.J.; Budarin, V.; Luque, R.; Clark, J.H.; Macqarrie, D.J. *Chem. Soc. Rev.* **2009**, *38*, 3401.

[57] Budarin, V.; Clark, J.H.; Hardy, J.J. E.; Luque, R.; Milkowski, K.; Tavener, S.J.; Wilson, A.J. *Angew. Chem. Int. Ed.* **2006,** *45*, 3782.

[58] White, R.J.; Budarin, V.L.; Clark, J.H. *ChemSusChem.* **2008**,1,408.

[59] White, R.J.; Antonio, C.; Budarin, V.L.; Bergstroem, E.; Thomas-Tates J.; Clark, J.H. *Adv. Funct. Mater.* **2010**, 20, 1834.

[60] White, R.J.; Budarin, V.L.; Clark, J.H. *Chem. Eur. J*. **2010**, 16, 1326.

[61] Schueth, F.; Sing, K.S.W.; Weitkamp, J. *Handbook of porous solids vol. 1,* Wiley-VCH: Weinheim, Germany, **2002**.

[62] Kresge, C. T.; Leonowicz, M. E.; Roth, W. J.; Vartuli, J. C.; Beck, J. S. *Nature* **1992,** *359*, 710.

[63] Beck, J. S.; Vartuli, J. C.; Roth, W. J.; Leonowicz, M. E.; Kresge, C.T.; Schmitt, K.D.; Chu, C.T.W.; Olson, D.H.; Sheppard, E.W.; McCullen, S.B.; Higgins, J. B.; Schlenker, J. L. *J. Am. Chem. Soc.* **1992,** *114*, 10834.

[64] Zhao, D. Y.; Huo, Q. S.; Feng, J. L.; Chmelka, B. F.; Stucky, G. D. *J.Am. Chem. Soc.* **1998,** *120*, 6024.

[65] Monnier, A.; Schuth, F.; Huo, Q.; Kumar, D.; Margolese, D.; Maxwell, R. S.; Stucky, G. D.; Krishnamurty, M.; Petroff, P.; Firouzi, A.; Janicke, M.; Chmelka, B. F. *Science* **1993,** *261*, 1299.

[66] Huo, Q. S.; Margolese, D. I.; Ciesla, U.; Demuth, D. G.; Feng, P. Y.; Gier, T. E.; Sieger, P.; Firouzi, A.; Chmelka, B. F.; Schuth, F.; Stucky, G. D. *Chem. Mater.* **1994,** *6*, 1176.

[67] Antonelli, D. M.; Ying, J. Y. *Angew. Chemie Int. Ed.* **1995,** *34*, 2014.

[68] Yang, H. F.; Zhao, D. Y. *J. Mater. Chem.* **2005,** *15*, 1217.

[69] Jun, S.; Joo, S. H.; Ryoo, R.; Kruk, M.; Jaroniec, M.; Liu, Z.; Ohsuna, T.; Terasaki, O. *J. Am. Chem. Soc.* **2000,** *122*, 10712.

[70] Eberhart, J. P., *Structural and Chemical Analysis of Materials*. John Wiley & Sons Ltd: England, **1991**.

[71] Strasser, P., *Small Angle X ray Scattering - Principles and Application - Lecture series, "Modern Methods in Heterogeneous Catalysis Research"*, Fritz Haber Institut, Berlin, **2009**.

[72] Ciccariello, S.; Goodisman, J.; Brumberger, H. *J. Appl. Cryst.* **1988**, *21*, 117.

[73] Ne, F.; Zemb, T. *J. Appl. Crystallogr.* **2003,** *36*, 1013.

[74] Rouquerol, J.; Rouquerol, F.; Sing, K. S. W., *Adsorption by Powders and Porous Solids, Principles, Methodology, and Applications*. Academic Press: **1998**.

[75] *Quadrasorb SI Operation Manual*, Quantachrome Instruments: USA, **2006**.

[76] Sing, K. S. W.; Eberett, D.H.; Haul, R.A.W.; Moscou, L.; Pierotti, R.A.; Rouquerol, J.; Siemieniewska, T. *Pure Appl. Chem.* **1985**, *57*, 603.

[77] Brunauer, S.; Emmett, P.H.; Teller, E. *J. Am. Chem. Soc.* **1938**, *60*, 309.

[78] C.Lippens, J.H. de Boer, *J. Catal.* **1965**, *4*,319.

[79] Barrett, E.P.; Joyner, L.G.; Halenda,P.H. *J. Am. Chem. Soc*. **1951**, *73*, 373.

[80] Dubinin, M.M. *Chem. Rev.* **1960**, *60*,235.

[81] Stoeckli, H.F. *J. Colloid Interface. Sci.* **1977**, *59*, 184.

[82] Horvath, G.; Kawazoe, K. *J. Chem. Eng.* **1983**,*16*,470.

[83] Saito. A; Foley, H.C. *AIChE J.* **1991**, *37*, 429.

[84] Neimark, A. V.; Lin, Y. Z.; Ravikovitch, P. I.; Thommes, M. *Carbon* **2009,** *47*, 1617.

[85] *Application of QSDFT*; Quantachrome Instruments: USA.

[86] Lambert, J.B.; Shurvell, H.F.; Lightner, D.A.; Cooks, R.G. *Introduction to Organic Spectroscopy*, Macmillan Publishing Company, New York, USA, **1987**.

[87] Nakanishi, K.; Soga, N. *J. Non-Crst. Solids* **1992**, *139*, 14.

[88] Roohi, F.; Antonietti, M.; Titirici, M. M. *J. Chromatogr. A* **2008**, *1203*, 160.

[89] Roohi, F.; Fatoglu, Y.; Titirici, M. M. *Anal. Methods* **2009**, *1*, 52.

[90] Roohi, F.; Titirici, M. M. *New J. Chem*. **2008**, *32*, 1409.

[91] Liang, C.; Dai, S.; Guichon, G. *Anal. Chem.* **2003**, *75*, 4904.

[92] Taguchi, A.; Smatt, J-H.; Linden, M. *Adv. Mater.* **2003**, *15*, 1209.

[93] Lu, A.H.; Smatt, J-H.; Backlund, S.; Linden, M. *Microporous Mesoporous Mater*. **2004**, *72*, 59.

[94] Z. Li, M. Jaroniec, *Anal. Chem.* **2004**, *76*, 5479.

[95] Kyotani, T.; Tsai, L. F.; Tomita, A. *Chem. Mater.* **1995,** *7*, 1427.

[96] Parthasarathy, R. V.; Phani, K. L. N.; Martin, C. L. R. *Adv. Mater.* **1995,** *7*, 896.

[97] Kyotani, T.; Tsai, L. F.; Tomita, A. *Chem. Mater.* **1996**, *8*, 2109.

[98] Rodriguez, A. T.; Chen, M.; Chen, Z.; Brinker, C. J.; Fan, H. Y. *J. Am. Chem. Soc.* **2006,** *128*, 9276.

[99] Wen, Z. H.; Wang, Q.; Li, J. H. *Adv. Funct. Mater.* **2008,** *18*, 959.

[100] Liang, H-W.; Liu, S.; Yu, S-H. *Adv. Mater.* **2010**, *22*, 3925.

[101] Dekker, C. *Physics Today* **1999,** *52*, 22.

[102] Forro, L.; Schonenberger, C. *Carbon Nanotubes* **2001,** *80*, 329.

[103] Tomanek, D.; Jorio, A.; Dresselhaus, M. S.; Dresselhaus, G. *Carbon Nanotubes* **2008,** *111*, 1.

[104] Kong, J.; Franklin, N. R.; Zhou, C. W.; Chapline, M. G.; Peng, S.; Cho, K. J.; Dai, H. J. *Science* **2000,** *287*, 622.

[105] Besteman, K.; Lee, J. O.; Wiertz, F. G. M.; Heering, H. A.; Dekker, C. *Nano Lett.* **2003,** *3*, 727.

[106] Lidorikis, E.; Ferrari, A. C. *ACS Nano* **2009,** *3*, 1238.

[107] Zhenhai, W.; Qiang, W.; Jinghong, L. *Adv. Funct. Mater.* **2008**, 959.

[108] Pan, X. L.; Fan, Z. L.; Chen, W.; Ding, Y. J.; Luo, H. Y.; Bao, X. H. *Nature Materials* **2007,** *6*, 507.

[109] Tibbetts, G. G.; Meisner, G. P.; Olk, C. H. *Carbon* **2001,** *39*, 2291.

[110] Zandonella, C. *Nature* **2001,** *410*, 734.

[111] Martin, C. R. *Adv. Mater.* **1991,** *3*, 457.

[112] Martin, C. R. *Science* **1994,** *266*, 1961.

[113] Steinhart, M.; Wendorff, J. H.; Greiner, A.; Wehrspohn, R. B.; Nielsch, K.; Schilling, J.; Choi, J.; Gosele, U. *Science* **2002,** *296*, 1997.

[114] Steinhart, M.; Wendorff, J. H.; Wehrspohn, R. B. *Chem. Phys. Chem.* **2003,** *4*, 1171.

[115] Chen, Q. L.; Xue, K. H.; Shen, W.; Tao, F. F.; Yin, S. Y.; Xu, W. *Electrochimica Acta* **2004**, *49*, 4157.

[116] Titirici, M-M.; Thomas, A.; Antonietti, M.; *Adv. Funct. Mater*.,**2007**, *17*, 1010.

[117] Kubo, S.; Tan, I.; White, R.J.; Antonietti, M.; Titirici, M-M. *Chem. Mater*. **2010**, *22*, 6590.

[118] Brun, N.; Prabaharan, S.R.S.; Morcrette, M.; Sanchez, C.; Pecastaings, G.; Derre, A.; Soum, A.; Deleuze, H.; Birot, M.; Backov, R. *Adv. Funct. Mater*. **2009**, *19*, 3136.

[119] Mitsukami, Y.; Donovan, M. S.; Lowe, A. B.; McCormick, C. L. *Macromolecules* **2001,** *34*, 2248.

[120] Lua, A. C.; Yang, T. *J. Colloid Interface Sci*. **2004**, *274*, 594.

[121] GomezSerrano, V.; PastorVillegas, J.; PerezFlorindo, A.; DuranValle, C. *J. Anal. Appl. Pyrol*. **1996**, *36*, 71.

[122] Lespade, P.; Aljishi, R.; Dresselhaus, M. S. *Carbon* **1982,** *20*, 427.

[123] De las Heras Alarcón, C.; Pennadam, S.; Alexander, C. *Chem. Soc. Rev.* **2005**, 276.

[124] Puoci, F.; Iemma, F.; Picci, N. *Current Drug Delivery* **2008,** *5*, 85.

[125] Heskins, M.; Guillet, J. E. *J. Macromol. Sci A* **1968,** *8*, 1441.

[126] Kanazawa, H. *J. Sep. Sci.* **2007,** *30*, 1646.

[127] Xu, G. Y.; Wu, W. T.; Wang, Y. S.; Pang, W. M.; Wang, P. H.; Zhu, G. R.; Lu, F. *Nanotechnology* **2006,** *17*, 2458.

[128] Hong, C. Y.; You, Y. Z.; Pan, C. Y. *Chem. Mater.* **2005,** *17*, 2247.

[129] Strano, M. S.; Dyke, C. A.; Usrey, M. L.; Barone, P. W.; Allen, M. J.; Shan, H. W.; Kittrell, C.; Hauge, R. H.; Tour, J. M.; Smalley, R. E. *Science* **2003,** *301*, 1519.

[130] Bahr, J. L.; Yang, J. P.; Kosynkin, D. V.; Bronikowski, M. J.; Smalley, R. E.; Tour, J. M. *J. Am. Chem. Soc.* **2001,** *123*, 6536.

[131] Zhao, Q.; Gan, Z.H.; Zhuang, Q.K. *Electroanalysis* **2002**, *14*, 1609.

[132] Lu, A.H.; Schueth, F. *Adv. Mater.* **2006**, *18*, 1793.

[133] Kyotani, T.; Nagai, T.; Inoue, S.; Tomita, A.; *Chem. Mater.* **1997**, *9*, 609.

[134] Zhao, D.; Feng, J.L.; Huo, Q.S.; Melosh, N.; Fredrickson, G.H.; Chmelka, B.F.; Stucky G.D., *Science* **1998**, *279*, 548..

[135] Lee, J.; Yoon, S.; Hyeon, T.; Oh, S.M.; Kim, K.B. *Chem. Commun.* **1999**, 2177.

[136] Li, Z.J.; Jaroniec, M. *J. Am. Chem. Soc.* **2001**, *123*, 9208.

[137] Kleitz, F.; Hei, C.S.; Ryoo, R. *Chem. Commun.* **2003**, 2136.

[138] Yang, H.; Shi, Q.; Liu, X.; Xie, S.; Jiang, D.; Zhang, F.; Yu, C.; Tu, B.; Zhao, D.; *Chem. Commun.* **2002**, 2842.

[139] Yu, C.; Fan, J.; Tian, B.; Zhao, D.; Stucky, G.D. *Adv. Mater.* **2002**, *14*, 1742.

[140] Y. Sakamoto, T. W. Kim, R. Ryoo, O. Terasaki, *Angew. Chem. Int. Ed.* **2004**, *43*, 5231.

[141] Lu, A.H.; Schueth, F. *Chem. Mater.* **2008**, *20*, 5314.

[142] Zhang, F.; Meng, Y.; Gu, D.; Yan, Y.; Chen, Z.; Tu, B.; Zhao, D. *Chem. Mater.* **2006**, *18*, 5279.

[143] Huang, Y.; Cai, H.Q.; Feng, D.; Gu, D.; Deng, Y.; Tu, B.; Wang, H.; Webley, P.A.; Zhao, D. *Chem. Commun.* **2008**, 2641.

[144] Zhang, F.; Gu, D.; Yu, T.; Zhang, F.; Xie, S.; Zhang, L.; Deng, Y.; Wan, Y.; Tu, B.; Zhao, D. *J. Am. Chem. Soc.* **2007**, *129*, 7746.

[145] Gu. D.; Bongard, H.; Meng, Y.; Miyasaka, K.; Terasaki, O.; Zhang, F.; Deng, Y.; Wu, Z.; Feng, D.; Fang, Y.; Tu, B.; Schueth, F.; Zhao, D. *Chem. Mater.* **2010**, *22*,4828.

[146] Titirici, M-M.; Thomas, A.; Antonietti, M. *J. Mater. Chem.* **2007**, *17*, 3412.

[147] Yao, C.; Shin, Y.; Wang, L-Q.; Windisch, C.F.; Samuels, W.D.; Arey, B.W.; Wang, C.; Risen, W.M.; Exarhos, G.J. *J. Phys. Chem. C* **2007**, *111*, 15141.

[148] Hergeth. W.-D.; Bloss, P.; Doering, E.; Witkowski, K.; Wartewig, S. *Acta Polym.* **1989**, *40*, 260.

[149] Matos, J. R.; Mercuri, L.P.; Kruk, M.; Jaroniec, M. *Langmuir* **2002**, *18*, 884.

[150] Xue, C.F.; Tu, B.; Zhao, D. *Nano Res.* **2009**, *2*, 242.

[151] Huo, Q.S.; Margolese, D.I.; Stucky, G.D. *Chem. Mater.* **1996**, *8*, 1147.

[152] Liu, J.; Yang, Q.; Zhao, X.S.; Zhang, L. *Microporous Mesoporous Mater.* **2007**, *106*, 62.

[153] Sun, J.; Zhang, H.; Ma, D.; Chen, Y.; Bao, X.; Klein-Hoffmann, A.; Pfaender, N.; Su, D.S. *Chem. Commun.* **2005**, 5343.

[154] Sun, J.; Zhang, H.; Tian, R.; Ma, R.; Bao, A.; Su, D.S.; Zoub, H. *Chem. Commun.* **2006**, 1322.

[155] Blin, J.L. ;Su, B.L. *Langmuir* **2002**, *18*, 5303.

[156] Blin, J.L.; Otjacques, C.; Herrier, G.; Su, B.L. *Langmuir*, **2000**, *16*, 4229

[157] Wanka, G.; Hoffman, H.; Ulbricht, W.; *Macromolecules*, **1994**, *27*, 4145.

[158] Zhang, Y.; Lam, Y.M.; Tan, W.S. *J. Colloid. Inter. Sci.* **2005**, *74*, 285.

[159] Ahn, J.H.; Kim, D.J.; Kimi, S.C.; Sang, M.J.; Lee, D.S. *Polym. Bull.* **2000**, *43*, 497.

[160] Attwood, D.; Collet, J.H.; Tait, C.J. *Int. J. Pharm*. **1985**, *26*, 25.

[161] Rassing, J.; Attwood, D. *Int. J. Pharm*. **1982**, *13*, 47.

[162] Lenaerts, V. ; Triqueneaux, C. ; Quarton, M.; Rieg-Falson, F.; Couvreur, P. *Int. J. Pharm*. **1987**, *39*, 121.

[163] Prasad, K.N.; Luong, T.T. ; Florence, A.T. ; Paris, J. ; Vaution, C. ; Seiller, M. ; Puisieux, F.; *J. Colloid Interface Sci.* **1997**, *69*, 225.

[164] Kurumada, K.; Robinson, B.H. *Progr. Colloid Polym Sci*. **2004**, *123*, 12.

[165] Schimidt, P.; Dybal, J.; Sturcova, A. *Vib. Spectrosc*. **2009**, *50*, 218.

[166] Bailey, J.R.; McGuire, M.M.; *Langmuir* **2007**, *23*, 10995.

[167] Acharya, K.R.; Bhattacharyya, S.C.; Moulik, S.P. *J. Photochem. Photobiol. A* **1999**, *122*, 47.

[168] Sharma, K.S.; Joshi, J.V.; Aswal, V.K.; Goyal, P.S.; Rakshit, A.K. *Pramana – J. Phys.* **2004**, *63*, 297.